

**INSTABILITY, ION HEATING, AND FLOW DRIVE IN HIGH- $\beta$  HALL PLASMAS**

by

Jason M. Milhone

A dissertation submitted in partial fulfillment of  
the requirements for the degree of

Doctor of Philosophy

(Physics)

at the

UNIVERSITY OF WISCONSIN–MADISON

2020

Date of final oral examination: July 13, 2020

The dissertation is approved by the following members of the Final Oral Committee:

Cary Forest, Professor, Physics

Jan Egedal, Professor, Physics

Ellen Zweibel, Professor, Astronomy and Physics

Stephanie Diem, Assistant Professor, Engineering Physics

Mark Nornberg, Associate Scientist, Engineering Physics

ProQuest Number:28031054

All rights reserved

INFORMATION TO ALL USERS

The quality of this reproduction is dependent on the quality of the copy submitted.

In the unlikely event that the author did not send a complete manuscript and there are missing pages, these will be noted. Also, if material had to be removed, a note will indicate the deletion.



ProQuest 28031054

Published by ProQuest LLC (2020). Copyright of the Dissertation is held by the Author.

All Rights Reserved.

This work is protected against unauthorized copying under Title 17, United States Code  
Microform Edition © ProQuest LLC.

ProQuest LLC  
789 East Eisenhower Parkway  
P.O. Box 1346  
Ann Arbor, MI 48106 - 1346

© Copyright by Jason M. Milhone 2020

All Rights Reserved

To Lauren,

Far better an approximate answer to the right question, which is often vague, than an exact answer to the wrong question, which can always be made precise.

—John Tukey

## INSTABILITY, ION HEATING, AND FLOW DRIVE IN HIGH- $\beta$ HALL PLASMAS

Jason M. Milhone

Under the supervision of Professor Cary Forest

At the University of Wisconsin-Madison

In pursuit of flow-driven plasma instabilities in the laboratory, a novel technique for stirring plasmas with global cross-field currents, volumetric flow drive, has been shown to drive high-Alfvén mach number ( $M_A = V/V_A$ ) flows in weakly magnetized, high- $\beta$  plasmas in the Hall regime. A uniform weak magnetic field is applied to the plasma volume. Electrodes inserted into the plasma drive radial current across the magnetic field to exert a torque on the plasma volume. Ion flows exceeding 1 km/s are measured with  $M_A \sim 0.2$  in argon plasmas.

A high-throughput, high-resolution Fabry-Pérot spectrometer was upgraded to measure ion temperature and flow profiles with 100 ms time resolution in low-temperature plasmas. The optics utilize a rail mount system with a collimator for the collection optics to increase portability and decouple the light collection from the plasma and the diagnostic optical alignment. A Bayesian analysis for the absolute wavelength calibration was developed to enable first measurements of ion flow with the spectrometer. With multiple chords through the plasma, profiles of ion temperature and flow are inferred from forward modeling and fitting the plasma emission resulting in measurements with resolution better than 0.1 eV and 50 m/s.

Hall physics drastically alter the expected equilibrium for volumetric flow drive on the Big Red Ball and the Plasma Couette Experiment. With magnetized electrons, unmagnetized ions, and an ion inertial scale greater than the system size ( $\sim 1$  m), the magnetic flux is frozen into the electron fluid which drifts at speeds much faster than the ions. Electron currents amplify the magnetic field (x20) when current drive is radially outward and expel the flux when reversed. Under the right conditions on PCX, a new electromagnetic instability is observed with the electron drifts as a source of free energy. The ions gain energy and momentum from the instability through Landau damping resulting in  $M_s \sim 0.2$  flows with an 2-3x increase in temperature compared to stable

plasmas. Driving flows in high- $\beta$ , Hall plasmas with cross-field currents offers an exciting new avenue of physics necessary to understand for flow-driven plasma instabilities in the laboratory.

## ACKNOWLEDGMENTS

It has been a long and winding journey to get to the end of my Ph.D. work. I started my journey learning the ropes of RF physics and attempting to build a high-voltage power supply. It was tough to pivot years into my work to rebuild and redesign the Fabry-Perot spectrometer, but in the end was worth the effort. I am grateful for the challenges that I faced, but I would be lying if I said I tackled them alone.

I would like to start by thanking Cary Forest for advising me. I will be the first to admit that sometimes I was initially taken aback by the sheer number of ideas you would propose for solving a problem, but in the end, you were almost always correct. You pushed me to be a better physicist and to ask the right questions, and I thank you for it.

It would have been literally impossible for me to have accomplished any of this work without the help of John Wallace and Mike Clark. Both of you were always available to help and ready to design and build a piece of hardware I needed to accomplish any project I was currently working on at the time. I especially want to thank Mike for the countless hours he spent with me testing high voltage power supplies. You showed incredible patience with the very difficult task we were set upon at the time.

I also would like to show my appreciation to Mark Nornberg. You spent many hours in my office discussing the finer details of spectroscopy and plasma physics. As a result, the Fabry-Perot spectrometer has turned out to be an amazing diagnostic and has given me a great love of Bayesian data analysis.

I owe a debt of gratitude to the graduate students that have worked on the various WiPPL projects. I have spent many hours in the office bouncing ideas back and forth with them to get a better understanding of experimental plasma physics. Ken, Joe, Ethan, and Doug, you have been

great friends during my time here at Wisconsin, and I look forward to a lifelong friendship with all of you.

It would be wrong if I didn't show my gratitude to my wife, Lauren. You have always stood by me as I struggled to finish my Ph.D. I am forever thankful to you for pushing me and challenging me to be a better person. You have been patient with me the entire time, and I look forward to the next step in our lives. I love you.

# TABLE OF CONTENTS

	Page
<b>Abstract</b> . . . . .	iii
<b>List of tables</b> . . . . .	x
<b>List of figures</b> . . . . .	xi
<b>1 Introduction and Motivation</b> . . . . .	1
1.1 Successful plasma spinning on the Plasma Couette Experiment . . . . .	6
1.2 High Rm flows on the Big Red Ball . . . . .	8
1.3 Thesis Outline . . . . .	9
<b>2 Experimental Device</b> . . . . .	11
2.1 The Big Red Ball . . . . .	12
2.1.1 Vacuum Vessel . . . . .	12
2.1.2 Cusp Confinement . . . . .	13
2.2 The Plasma Couette Experiment . . . . .	14
2.3 Plasma Production . . . . .	15
2.3.1 Emissive Cathodes . . . . .	15
2.3.2 Electron Cyclotron Heating . . . . .	16
2.3.3 Plasma Washer Guns . . . . .	16
2.3.4 Compact Toroid Injector . . . . .	17
2.4 Diagnostics . . . . .	17
2.4.1 Single Tip Swept Langmuir Probe . . . . .	17
2.4.2 Triple Probe . . . . .	18
2.4.3 Mach Probe . . . . .	18
2.4.4 3-Axis Hall Probe Array . . . . .	19
2.4.5 mm-wave interferometer . . . . .	21
2.4.6 Optical Emission Spectroscopy . . . . .	22
2.4.7 Fabry-Pérot Spectrometer . . . . .	24
2.5 Experimental Workflow and Data Acquisition . . . . .	24

	Page
2.5.1 Control Software . . . . .	24
2.5.2 Data Acquisition . . . . .	24
2.5.3 Data Visualization . . . . .	25
<b>3 A spectrometer for high-precision ion temperature and velocity measurements in low-temperature plasmas . . . . .</b>	<b>27</b>
3.1 Fabry-Pérot Basic Theory . . . . .	28
3.2 Design Considerations for high-resolution spectroscopy . . . . .	30
3.3 Image Processing . . . . .	34
3.4 Bayesian Method for Analysis . . . . .	35
3.5 Plasma Analysis . . . . .	42
3.6 Initial Results . . . . .	43
3.7 Camera Upgrade . . . . .	45
3.8 Étalon Temperature Stabilization . . . . .	47
3.9 Summary . . . . .	51
<b>4 Volumetric Flow Drive . . . . .</b>	<b>52</b>
4.1 Overview of Volumetric Flow Drive . . . . .	52
4.2 Volumetric Flow Drive on the BRB . . . . .	54
4.3 Results on PCX . . . . .	60
4.4 VFD Ion Temperature and Flow Profiles . . . . .	64
4.5 Summary . . . . .	71
<b>5 Electromagnetic Gradient Drift Instability . . . . .</b>	<b>73</b>
5.1 Fluctuation onset on PCX . . . . .	74
5.2 Mode structure . . . . .	75
5.3 Ion heating and flow . . . . .	80
5.4 The Electromagnetic Gradient Drift Instability . . . . .	86
5.5 Comparison of theory and experiment . . . . .	88
5.6 Summary . . . . .	90
<b>6 Conclusion . . . . .</b>	<b>92</b>
6.1 Summary of Results . . . . .	92
6.2 Future Work . . . . .	95
<b>References . . . . .</b>	<b>96</b>

	Page
<b>Appendix A: Bayesian Probability for Fabry-Pérot Spectroscopy . . . . .</b>	109
<b>Appendix B: High Beta Gradient Drift Instability Derivation . . . . .</b>	112
<b>Appendix C: Electron Cyclotron Heating System . . . . .</b>	115

## LIST OF TABLES

Table	Page
2.1 Plasma parameters for different plasma sources . . . . .	15
3.1 Camera comparison table . . . . .	46

## LIST OF FIGURES

Figure	Page
1.1 Sunspot Butterfly Diagram . . . . .	2
1.2 PCX Velocity and Viscosity . . . . .	7
2.1 Big Red Ball . . . . .	11
2.2 Big Red Ball CAD Drawing . . . . .	12
2.3 Big Red Ball Confinement Scheme . . . . .	13
2.4 The Plasma Couette Experiment . . . . .	14
2.5 Triple Probe Schematic . . . . .	19
2.6 3-axis Hall Probe Array . . . . .	20
2.7 mm-Wave Interferometer . . . . .	21
2.8 MDSplus Tree Structure . . . . .	25
2.9 PiScope . . . . .	26
3.1 Étalon Diagram . . . . .	30
3.2 Fabry-Pérot Concentric Rings . . . . .	32
3.3 Fabry-Pérot Diagram . . . . .	33
3.4 Fabry-Pérot Annular Sum . . . . .	35
3.5 Bayesian Procedure . . . . .	35
3.6 Fabry-Pérot Thorium Lamp Peaks . . . . .	38

Figure	Page
3.7 Fabry-Pérot Synthetic Posterior Wavelength . . . . .	40
3.8 Fabry-Pérot Synthetic Marginal Posterior for $\mathcal{F}$ . . . . .	41
3.9 Marginal Joint Posterior for $f_2$ and $d$ . . . . .	44
3.10 Fabry-Pérot Marginal Posterior for $T_i$ and $V$ . . . . .	45
3.11 $T_i$ Time Trace . . . . .	47
3.12 Étalon PID Tuning . . . . .	48
3.13 Étalon PID Temperature Control . . . . .	49
3.14 Zero velocity Calibration Drift . . . . .	49
3.15 Étalon Calibration Mirror Stage . . . . .	50
4.1 Frequencies and Length Scales vs Magnetic Field . . . . .	53
4.2 BRB VFD Setup . . . . .	54
4.3 Probe Locations for BRB Volumetric Flow Drive . . . . .	55
4.4 Typical VFD Time Traces on the BRB . . . . .	56
4.5 2D Magnetic Field Measurements for VFD on BRB . . . . .	57
4.6 BRB Volumetric Flow Drive Radial Profiles . . . . .	58
4.7 PCX Volumetric Flow Drive Schematic . . . . .	60
4.8 Volumetric Flow Drive Time Trace . . . . .	61
4.9 VFD Equilibrium Radial Profiles . . . . .	63
4.10 Fabry-Pérot flow confirmation . . . . .	65
4.11 Fabry-Pérot Plasma Forward Model . . . . .	66
4.12 VFD Fabry-Pérot Chord Fits . . . . .	67
4.13 VFD $T_i$ and $V$ Marginals . . . . .	68

Figure	Page
4.14 VFD $T_i$ and $V$ Profiles . . . . .	69
4.15 VFD $T_i$ and $V_{pk}$ time trace . . . . .	70
5.1 Time trace fluctuations . . . . .	74
5.2 Plasma Stability vs Magnetic Field and Injected Current . . . . .	75
5.3 Fluctuation Radial Profiles . . . . .	76
5.4 Fluctuation power spectral density . . . . .	77
5.5 Unstable Mode Video Still . . . . .	78
5.6 Cross-correlations and Toroidal shift time traces . . . . .	79
5.7 2D Mode Reconstruction . . . . .	80
5.8 Unstable Plasma $T_i$ and $V_\phi$ profiles . . . . .	81
5.9 Unstable Plasma $T_i$ and $V$ Marginal Posteriors . . . . .	81
5.10 Fabry-Pérot Unstable Fits . . . . .	82
5.11 FP spectrum from EMGDI . . . . .	83
5.12 $T_i$ vs Mean $B_z$ . . . . .	84
5.13 Mode frequency and Velocity vs Mean Magnetic Field . . . . .	85
5.14 Gradient Drift Instability Frequency . . . . .	88
5.15 Frequency vs peak ion velocity, $V_{i0}$ . . . . .	89
5.16 Growth rate vs $\beta$ . . . . .	90
Appendix	
Figure	
C.1 Magnetron Power Supply . . . . .	116
C.2 Mod Reg Schematic . . . . .	117

Figure	Page
C.3 Mod Reg Feed Forward . . . . .	118
C.4 Mod Reg Resistor Test . . . . .	119
C.5 Saturable Reactor Diagram . . . . .	120
C.6 Filament Heating with Saturable Reactor . . . . .	121
C.7 Magnetron Power Supply Schematic . . . . .	122
C.8 Magnetron Mod Reg Testing . . . . .	123
C.9 Magnetron Power Time Trace . . . . .	124
C.10 Argon $n_e$ and $T_e$ vs RF Power . . . . .	126
C.11 Argon $n_e$ and $T_e$ radial profiles . . . . .	126
C.12 Helium $n_e$ and $T_e$ radial profiles . . . . .	127

# Chapter 1

## Introduction and Motivation

Plasmas are the most abundant form of matter in the universe and many are threaded by magnetic fields. Astrophysical plasmas found in the heliosphere, accretion disks, and jets have flows or pressure that dominate over a weak magnetic field and can be characterized by high-Alfvén mach numbers ( $M_a = V/V_A \gg 1$ ) and high-beta ( $\beta = 2\mu_0 P/B^2 \gg 1$ ). In these plasmas, the magnetic field plays a subdominant role in the source of free energy in the system but is still crucial to the overall dynamics. Two important flow driven instabilities for magnetic field generation and accretion are the dynamo and the magnetorotational instability (MRI).

In weakly collisional systems threaded by weak magnetic fields, the Hall effect can be an important contributor to the dynamics. For magnetic field generation, there is always a transition to a weak magnetic field where the electrons become magnetized while the field is too weak to magnetize the ions. In the Hall regime, the electron dynamics decouple from the ion dynamics at scales below the ion inertial scale ( $d_i = c/\omega_{pi}$ ) leading to new behavior between the plasma and the magnetic field. Typically, plasmas have high conductivity and the magnetic field is considered frozen into the plasma fluid. However, in the Hall regime, the magnetic field can become frozen into the electron fluid. This can have profound implications on how the magnetic field interacts with the plasma as a whole. In the dynamo instability, the electrons are able to stretch, twist, and fold the magnetic field on much finer spatial scales drastically altering the growth rate and saturation mechanism [1, 2]. For accretion where the MRI is believed to be important, the Hall effect alters the growth rate with a dependence on the rotation vector being parallel or anti-parallel

to the vertical magnetic field [3, 4]. Up until now, the Hall effect has been largely ignored in describing the equilibrium of laboratory plasmas looking to excite flow driven plasma instabilities. The goal of this thesis is to understand the equilibrium, flow, and stability of high-beta plasmas in the Hall regime in pursuit of creating conditions that could naturally lead to the excitation of these instabilities in the lab.

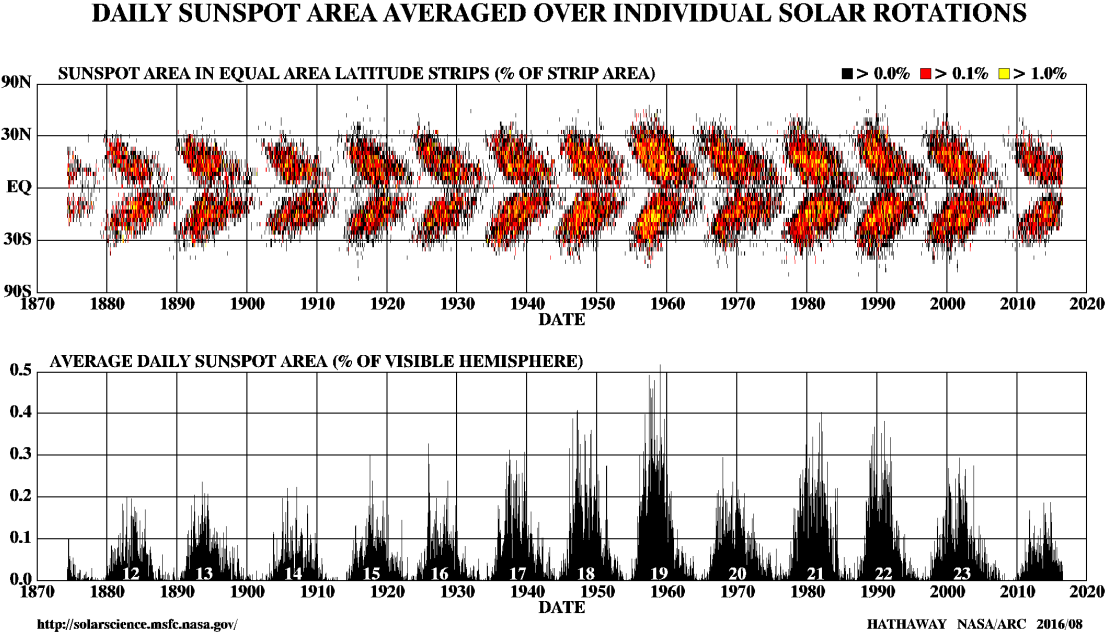


Figure 1.1: The sunspot butterfly diagram. During solar minimum sun spots appear near the mid-latitudes. As solar maximum is approached, sun spots appear closer to the equator and the total number increases. Not shown is the full 22 period with magnetic polarity reversal. Figure credit to NASA/Marshall Space Flight Center

The dynamo effect is believed to be the mechanism for the generation and maintenance of magnetic fields in the universe. If the Earth’s magnetic field was not maintained, it would decay via resistive dissipation in  $\sim 10^4$  years which is much less than the age of the Earth (4 billion years). In addition, paleomagnetic studies show clear evidence that the Earth’s magnetic field has repeatedly reversed direction at irregular intervals over the last 4 million years with an average period with an average of  $2 \times 10^5$  years. In contrast, the sun has a much lower resistivity resulting in

a much longer resistive decay time compared to the Earth but undergoes reversals at a much faster rate. The resistive decay time for the sun's magnetic field is on the order of the age of the solar system. The sun exhibits a 22 year cycle of solar activity where the sun's magnetic field polarity reverses sign and the number and location of sun spots observed varies. The classical butterfly diagram presented in Fig. 1.1 demonstrates the half-solar cycle where sun spots appear at the mid-latitudes during solar minimum. The number of sun spots increases and their location moves toward the equator as solar maximum is reached. These complicated dynamics of the magnetic field in the Earth and Sun point to an underlying inductive process such as the dynamo generating and sustaining magnetic fields.

Astrophysical bodies such as stars, galaxies, planets are all formed by the accretion of matter, but conservation of angular momentum requires a mechanism for matter falling inward to transfer angular momentum outward. Like the resistive decay of the magnetic field of stars, the time scale of viscous diffusion in accretion disks does not meet observations and expectations. Shakura and Sunyaev suggested an enhanced turbulent viscosity to account for fast momentum transport [5]; however, particles in a gravitational field exhibit Keplerian motion ( $\Omega \propto r^{-3/2}$ ) and are stable according to the Raleigh criterion ( $\partial(r\Omega^2)/\partial r < 0$ ). Velikhov and Chandrasekhar both independently realized that a weak magnetic field can drastically alter the stability of differentially rotating conducting fluids and ionized gases [6, 7]. In the 1990s, the magnetorotational instability is named and proposed as the possible cause of turbulence in accretion disks [8]. In addition, the Hall effect is known to affect the growth rates of the MRI favoring the flow to be spinning anti-parallel to the vertical magnetic field [3, 4].

In both the dynamo and the MRI, there are two dimensionless numbers, the fluid and magnetic Reynolds numbers, that are crucial to understanding their behavior and stability. The fluid Reynolds number ( $R_e$ ), the ratio of the inertial forces to the viscous forces, describes if a flow is laminar ( $R_e \ll 1$ ) or turbulent ( $R_e \gg 1$ ). The magnetic Reynolds number ( $R_m$ ), the ratio of magnetic advection to magnetic diffusion, determines if the magnetic field is frozen into the fluid flow ( $R_m \gg 1$ ) or if the magnetic field diffuses quickly ( $R_m \ll 1$ ). The fluid and magnetic Reynolds

numbers are given by

$$R_e = \frac{LV}{\nu} \quad (1.1)$$

$$R_m = \frac{LV}{\eta} \quad (1.2)$$

where  $L$  is the characteristic length scale,  $V$  is a characteristic velocity such as the peak velocity,  $\nu$  is the kinematic viscosity, and  $\eta$  is the magnetic diffusivity.

Liquid metals were first used to study flow driven instabilities, but with a fixed resistivity and viscosity, liquid metals operate in a turbulent regime at relatively low velocities at low Prandtl number ( $P_m = R_m/R_e \sim 10^{-6}$ ) pushing the critical magnetic Reynolds number beyond the achievable limits. Plasmas are an attractive option because the resistivity and viscosity can be varied independently. Using Braginskii's transport theory [9], the fluid and magnetic Reynolds numbers are given by

$$R_e = 7.8 \frac{n_{18} \sqrt{\mu} Z^4 V_{\text{km/s}} L_m}{T_{i,eV}^{5/2}} \quad (1.3)$$

$$R_m = 1.6 \frac{T_{e,eV}^{3/2} V_{\text{km/s}} L_m}{Z} \quad (1.4)$$

where  $n_{18}$  is the plasma density in units of  $10^{18} \text{ m}^{-3}$ ,  $\mu$  is the ion mass in amu,  $Z$  is the ion charge state,  $V$  is the characteristic velocity in km/s,  $L$  is the system size in m,  $T_e$  is the electron temperature in eV, and  $T_i$  is the ion temperature in eV. In a plasma, these parameters can be varied almost independently yielding a range of accessible magnetic Prandtl numbers. For example, the electrons can be heated via electron cyclotron resonant heating, and the density can be kept at moderate levels ( $\sim 5 \times 10^{17} \text{ m}^{-3}$ ) using hot emissive cathodes where the ions are only heated slightly ( $T_i \sim 0.5 \text{ eV}$ ) from collisions with electrons.

The pursuit of flow driven plasma instabilities in laboratory plasmas necessitates a well-confined, hot, unmagnetized, flowing plasma. Previous experiments at the Wisconsin Plasma Physics Laboratory (WiPPL) have achieved great results with driving fast flows in weakly magnetized plasmas. Measurement of the fluid Reynolds number, critical to developing flow shear, requires accurate measurements of the flow velocity and the ion temperature which is difficult to measure in low

temperature plasmas. Typically, Mach probes combined with a swept Langmuir probe have been used to measure flow velocity profiles but are not very precise. A Fabry-Pérot spectrometer was built and successfully used to measure time-averaged ion temperatures, but not flow. As a result, an upgrade to both the spectrometer and the calibration procedure was undertaken during this thesis work to increase the spectrometer's capability to measure temperature and flow profiles for multiple times points during a plasma discharge.

When the first plasma experiments for the dynamo and the MRI at the University of Wisconsin-Madison were developed, the relevant plasma parameters were determined using resistive magnetohydrodynamics (MHD). However, plasmas are complicated, and there are other important effects outside of MHD. The viscosity can be anisotropic resulting in drastically different rates of momentum transport parallel and perpendicular to the magnetic field. For the ions, the magnetized perpendicular viscosity (relative to the magnetic field) is drastically lower when compared to the unmagnetized viscosity for the same density and temperature. Additionally, in diffuse plasmas where the collisionality is low, the ion inertial scale can become large compared to the system size and gradient length scales leading to a decoupling between the ions and the electrons. In this Hall regime, the magnetic field can now be frozen into the electron fluid instead of the ion fluid. The electron motion can result in Hall currents that are strong enough to modify the background magnetic field significantly. These effects can drastically alter the equilibrium and interaction of the plasma with the magnetic field.

Experiments with weakly magnetized, well-confined, high- $\beta$  plasmas in the Hall regime relevant to flow-driven instabilities are almost non-existent outside of WiPPL. Helicons are generally operated at low- $\beta$ , but can be operated at high- $\beta$ . Results from the WOMBAT experiment showed  $\beta > 1$  plasmas with very little diamagnetism [10] and is possibly explained by the neutral pressure profile [11]. On the COBRA device at Cornell, high density plasma jets from plasma bubbles exhibited increased density or hollowing out depending on the injected current showcasing the effects of the Hall physics [12], but the evolution of the magnetic field was not measured. Experiments on a linear plasma device with a geometry very similar to the Plasma Couette Experiment operated at  $\beta > 1$  with weakly magnetized ions observed large amounts of diamagnetism but

lacked particle confinement [13]. The Hall effect is known to be important in space propulsion such as Hall thrusters, but are typically low- $\beta$  [14]. When the plasma is partially magnetized like in Hall thrusters, the electrons are able to drift at speeds much faster the sound speed leading to electrostatic instabilities such as the Simon-Ho [15, 16] and the gradient drift instability [17]. With high- $\beta$ , there is the possibility for the fast drifting electrons to interact with the magnetic field to excite electromagnetic instabilities where the ions might interact with the wave modifying the distribution function. The work in this thesis aims to display and explain the equilibrium, stability, and plasma flow that can be studied in high-performance, well-confined, partially magnetized, high- $\beta$  plasmas in the Hall regime at WiPPL.

## 1.1 Successful plasma spinning on the Plasma Couette Experiment

The Plasma Couette Experiment (PCX) is an experiment at the Wisconsin Plasma Physics Laboratory (WiPPL) built for studying flowing plasmas and the excitation of the MRI. The experiment is described in more detail in Chapter 2. A novel technique for stirring unmagnetized plasmas was developed and successfully implemented on PCX. Hot, emissive cathodes are inserted into the magnetized edge of the plasma and biased to cold anodes drawing cross-field current. A local torque is applied to the plasma resulting in plasma flow at the edge. Momentum is carried inward via plasma viscosity leading to the whole plasma flowing.

With edge-stirred plasmas, the flow profile is governed by the diffusion of momentum via ion viscosity and charge-exchange collisions with neutrals. The viscosity is a diffusive process where ions collide with other ions exchanging momentum. Charge exchange collisions are a momentum sink; a fast ion collides with a slow neutral exchanging a bound electron resulting in a fast unconfined neutral colliding with the vacuum wall before it can be re-ionized. A model for the flow profile was developed by Cami Collins using toroidal momentum force balance in the bulk of the plasma with assumed velocity at the plasma edge [19, 18]. The toroidal velocity profile is described by

$$v_\phi = AI_1(r/L_\nu) + BK_1(r/L_\nu) \quad (1.5)$$

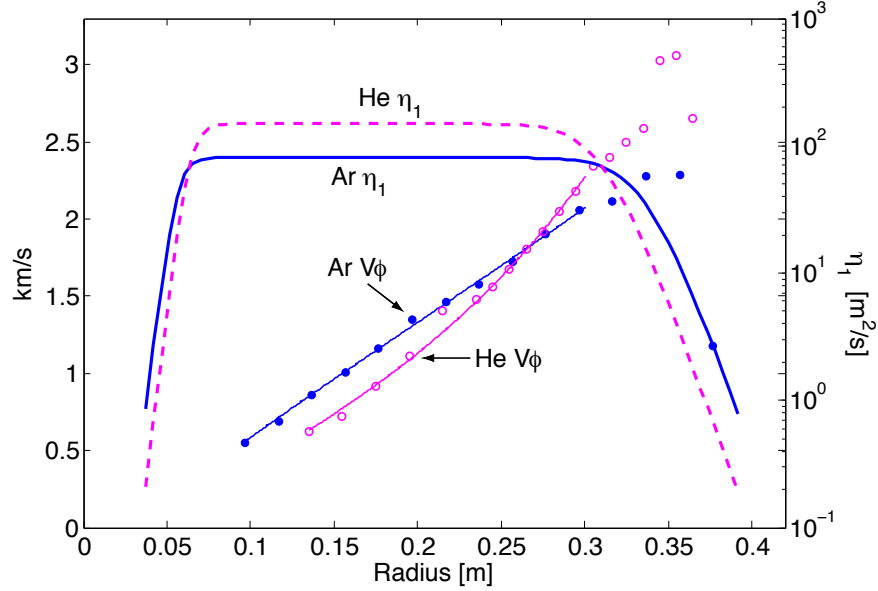


Figure 1.2: Profiles of velocity and viscosity for argon and helium plasmas on PCX. Viscosity is calculated using Braginskii formulation with ion temperature from velocity profile fit. Figure credit to Cami Collins [18].

where  $L_\nu = \sqrt{\tau_{i0}\nu}$  is the momentum diffusion length,  $\tau_{i0}$  is the ion-neutral collision time, and  $I_1$  and  $K_1$  are the modified Bessel functions of the first and second kind. The coefficients  $A$  and  $B$  are determined by the velocities of the inner and outer boundaries. Measurements from PCX taken by Cami Collins illustrate good agreement between the model and measurements of the flow in both argon and helium plasmas as shown in Fig. 1.2. If charge exchange collisions are frequent, the momentum is unable to penetrate very far in the plasma.

Understanding the stability of the flow profile to the MRI requires high-resolution measurements of the ion temperature and the flow. The unmagnetized viscosity scales like  $T_i^{5/2}$ . A measurement of the ion temperature and density with 10% uncertainty results in a 27% uncertainty of the calculated viscosity. Additionally, the droop in the profile can be used as a measurement of the viscosity as shown in Fig. 1.2. This motivates this thesis work to develop a high-resolution, high-throughput Fabry-Pérot spectrometer for measuring ion temperatures and velocities with time dynamics matching the equilibrium evolution ( $\sim 100$  ms).

These previous experiments were successful for spinning plasmas, but improvements were needed to achieve plasmas that could be unstable to the MRI. Ultimately, the neutrals played a crucial role in determining the flow profile making it hard to spin the plasma fast enough with enough flow shear using the center magnet stack. Higher ionization fraction plasmas would allow for faster flows and efficiently couple more of the momentum inward.

## 1.2 High $R_m$ flows on the Big Red Ball

The Big Red Ball (BRB), formerly the Madison Plasma Dynamo Experiment (MPDX), was developed as the successor to PCX for studying flow-driven plasma instabilities and now regularly achieves flows exceeding 5 km/s in helium with ionization fractions of 90% and 50% for argon and helium respectively. Neutrals still affect the momentum diffusion with the flow only penetrating  $\sim 1/3$  of the radius. A project to mitigate these issues by adding additional power through electron cyclotron heating (ECH) is discussed in Appendix C. The flows are an improvement over PCX and the momentum diffusion length is better, but the larger device still leads to charge-exchange collisions limiting the momentum coupling to the whole plasma from the edge stirring.

To avoid the reliance on momentum diffusion, a new method of stirring was needed for spinning plasmas that does not rely on momentum diffusion competing against charge-exchange collisions. Volumetric flow drive is a novel idea originally proposed for stirring liquid metals where a current is forced across a magnetic field to apply a  $\mathbf{J} \times \mathbf{B}$  torque on the entire plasma volume. Applying a body force removes the dependence on viscosity to couple momentum in the plasma, and charge-exchange collisions only function as a body force slowing down the flow and not affecting the overall profile shape. With a cylindrical geometry, the radial injected current is expected to scale like  $\sim 1/r$  creating a torque on the plasma with a centrally peaked flow with similar profile.

The first experiments of volumetric flow drive performed by Dave Weisberg are promising with a centrally peaked flow profile that could potentially be unstable to the MRI, but require more diagnosing [20, 21]. With the density in the  $10^{17} - 10^{18} \text{ m}^{-3}$  range with weakly magnetized ions, the plasma is firmly in the Hall regime. Initial data does show a centrally peaked flow consistent with our simple 1D MHD model, but the Hall term should be expected to modify the equilibrium.

Additionally, at the time of the original experiments, none of the existing probes were capable of measuring the magnetic field deep inside the plasma. With a probe designed and built by Ethan Peterson, all 3 components of the magnetic field can be measured with a linear array of Hall probes. The Hall probe array is discussed in more detail in Chapter 2. With measurements of the magnetic field and the plasma flow, the effects of Hall currents on the equilibrium and stability of the plasma are ready to be studied.

### 1.3 Thesis Outline

Plasmas offer a new exciting avenue for studying flow-driven plasma instabilities such as the dynamo and the MRI, but the plasma parameters necessary for high  $R_e$  and  $R_m$  require accounting for Hall physics. The stability criterion are directly related to the geometry of the flow and the viscosity presenting a need for high resolution measurements of the ion temperature and flow. Non-ideal effects such as the Hall effect play a large role in how the plasma interacts with the magnetic field. When the plasma is partially magnetized, the electrons decouple from the ions. The typical frozen-in flux condition ( $R_m \gg 1$ ) is modified to the magnetic field being frozen into the electron fluid. In low temperature Hall plasmas, most of the plasma pressure is in the electron fluid that is able to drift at large speeds relative to the ions resulting in large currents. These large currents lead to large magnetic fields relative to the ambient magnetic field and should modify the equilibrium. These effects beg the question: What role does the Hall effect play in the equilibrium and stability of flowing plasma driven by cross field currents?

Typically, plasmas generated with hot cathodes at WiPPL are low-collisionality without any direct heating to the ions resulting in long thermalization times and  $T_i \ll T_e$ . With the electrons drifting at speeds much larger than the sound speed and stationary ions, the plasma should be susceptible to kinetic instabilities. If that is the case, what role do the ions play? If there is an instability driven by the fast electron drift, it is possible that the ions could gain energy and momentum from the instability if the phase velocity is low enough. With a high-resolution spectrometer, can the changes to the ion distribution function be measured? With the upgraded Fabry-Pérot

spectrometer, ion temperatures can be measured with resolution better than 0.1 eV, perfect for inferring additional heating sources to the ions when comparing plasmas with similar collisionality and plasma production.

This thesis presents the results from flowing plasmas stirred by volumetric flow drive and how the Hall effect changes the plasma equilibrium and in some cases, leads to large non-axisymmetric fluctuations. The changes to the equilibrium from the Hall effect are documented extensively with the use of electrostatic probes and 3-axis Hall probes. First measurements of the ion temperature and flow profiles using a high-resolution Fabry-Pérot spectrometer upgraded during this thesis work are presented. Additionally, the Hall effect and the direction of the injected current lead to either quasi-Keplerian flow or solid body rotation profiles. Under the right conditions, the Hall effect leads to a new instability on PCX that only occurs with a finite- $\beta$ .

A brief outline of the thesis is presented here. Chapter 1 serves as motivation for building a high-resolution, high-throughput Fabry-Pérot spectrometer used in conjunction with other plasma diagnostics for studying the equilibrium and stability of partially magnetized, high- $\beta$ , flowing plasmas in the Hall regime. Chapter 2 describes the experiments and diagnostics used in this thesis work. Chapter 3 goes into detail the design, upgrade, and analysis for a high-resolution, high-throughput Fabry-Pérot spectrometer for measuring ion temperatures and flows. Chapter 4 discusses the equilibrium properties of volumetric flow drive in high- $\beta$  Hall plasmas with magnetic amplification/extreme diamagnetism depending on the current direction. MRI relevant flows are produced with volumetric flow drive, but the Hall effect provides stabilization to the equilibrium from the MRI. Chapter 5 describes a unique instability to high- $\beta$  Hall plasmas observed on PCX where the ions are ultimately heated and gain momentum from the electrons via the instability. Chapter 6 summarizes the results of this work and provides future avenues to continue studying high- $\beta$  Hall plasmas.

## Chapter 2

### Experimental Device

This chapter describes the Big Red Ball (BRB) device, formally known as the Madison Plasma Dynamo Experiment, and the Plasma Couette Experiment (PCX). The BRB and PCX are versatile machines at the Wisconsin Plasma Physics Laboratory (WiPPL) for studying a wide variety of plasma phenomena including but not limited to the dynamo, the magnetorotational instability, magnetic reconnection, flux-rope turbulence, and collisionless plasma shocks.

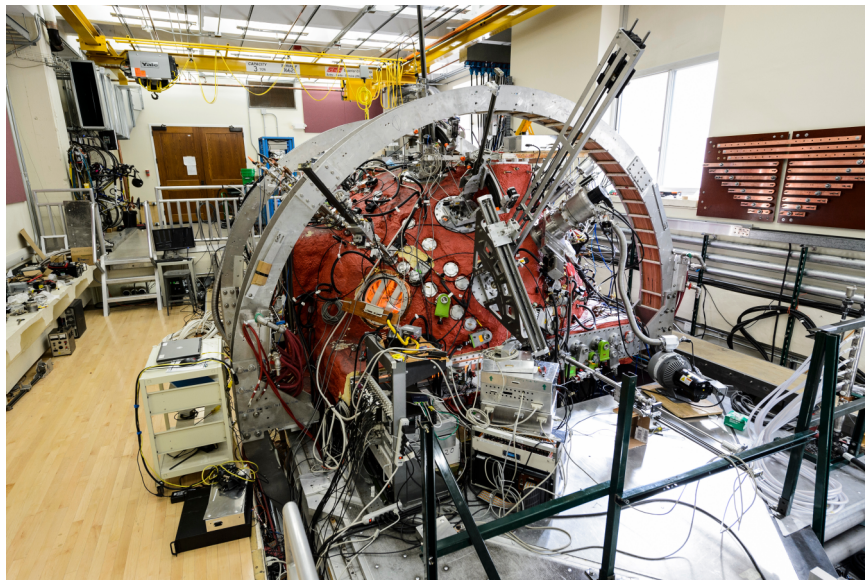


Figure 2.1: A photo of the Big Red Ball looking at the North Pole of the vessel. This photo was taken during the Parker spiral run campaign by UW Photographer Jeff Miller

## 2.1 The Big Red Ball

### 2.1.1 Vacuum Vessel

The BRB consists of two 1.25" thick cast aluminum 1.5 m radius hemispheres. One of the hemispheres is mounted on rails to allow the sphere to be opened for access inside the vessel. There are a large array of ports including 184 small, 14 large, and 12 box ports for diagnostic access. The small ports allow for probes to be inserted radially. The large 16" ports are used for 2D stages mounted with ball joints for scanning an arc in the poloidal plane. A CAD drawing of the vessel can be seen in Fig. 2.2. Some of the box ports have been converted to windows for viewing the plasma with optical diagnostics. The BRB has a large plasma volume with great port access making it a great platform for studying a wide range of plasma phenomena.

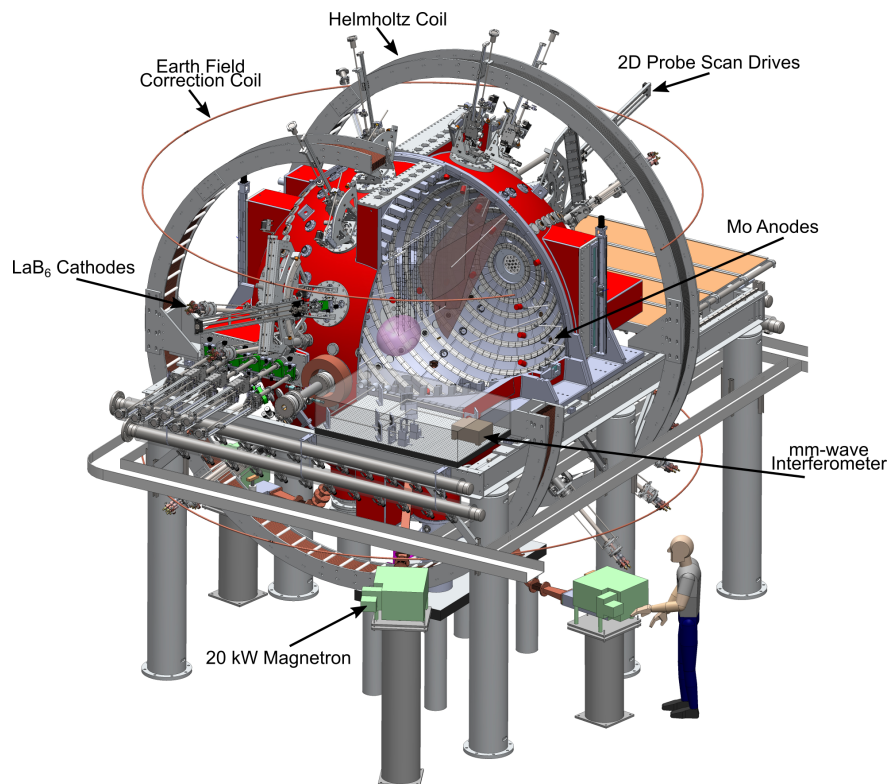


Figure 2.2: CAD drawing of the BRB device with cutout showing the rings of permanent magnets as well as diagnostic access from sweep stages.

## 2.1.2 Cusp Confinement

The BRB utilizes a multi-dipole cusp for plasma confinement with a large-volume unmagnetized core. There are 36 axisymmetric rings of samarium cobalt (SmCo) magnets with each ring alternating in polarity. Each ring is spaced  $5^\circ$  apart from  $-87.5^\circ$  to  $+87.5^\circ$ . Each magnet has approximately  $\sim 3$  kG surface magnetic field strength. Approximately 20 cm from the surface of the magnets, the magnetic field has decayed to almost Earth's magnetic field. As a result, the plasma has a large volume-to-loss-area ratio yielding high performance plasmas with confinement times on the order of milliseconds. A schematic of the magnetic field geometry and profiles of electron density and temperature are shown in Fig. 2.3. The inset shows the decay of the magnetic field along with the electron density and temperature profiles with a plasma edge located at  $\sim 140$  cm where the magnetic field is about 50 G. As a result of the confinement scheme, high performance plasmas are obtained with an unmagnetized core with gradients only in the edge.

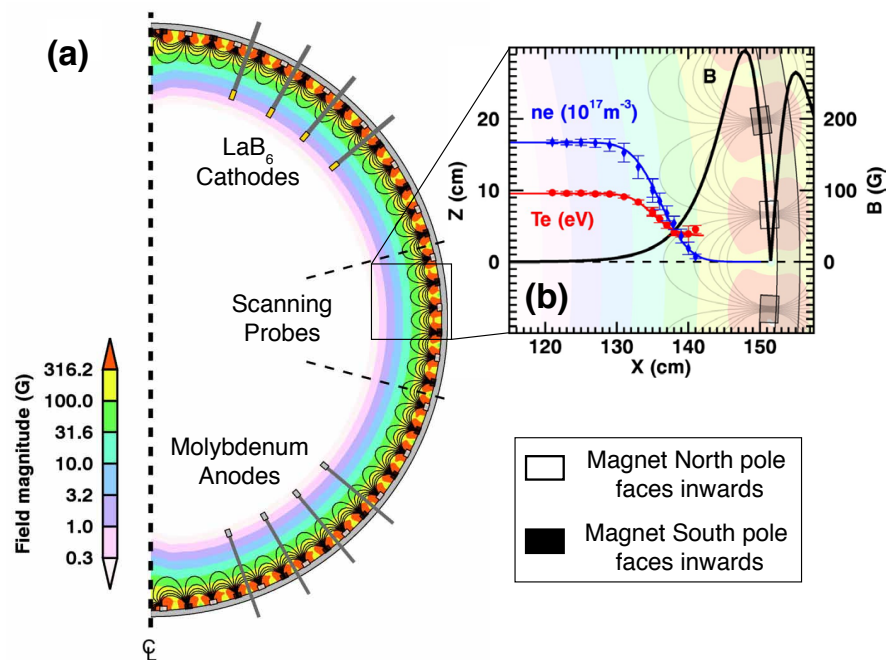


Figure 2.3: (a) Magnetic field drops off rapidly as a function of distance from the magnets. (b) Plasma is confined by edge magnetic field with the only gradients in the edge of the plasma.

## 2.2 The Plasma Couette Experiment

The Plasma Couette Experiment (PCX) is a 1 m diameter, 1 m tall cylindrical stainless steel vacuum vessel presented in Fig. 2.4. It is the prototype experiment for the BRB. During 2015, PCX was upgraded by Ken Flanagan in his thesis work to enlarge the plasma volume and increase the plasma performance. The old magnets were replaced with similar samarium cobalt magnets on the BRB. There are concentric rings of alternating polarity magnets forming a high-order multipole cusp magnetic field to confine the plasma. Two rings located at the top and bottom “corners” tilted at  $45^\circ$  were added to reduce plasma leakage. Part of the upgrade included adding water cooling lines for each magnet ring. The magnets are covered with alumina tile limiters to insulate the conducting magnets from the plasma. After the upgrade, PCX is capable of producing 5 eV,  $10^{18} \text{ m}^{-3}$  argon plasmas with  $> 50\%$  ionization fractions.

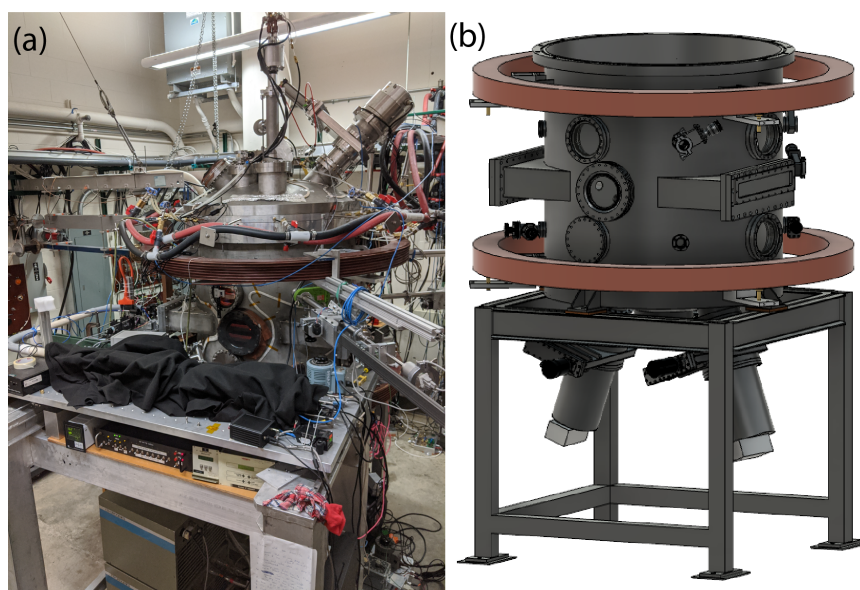


Figure 2.4: (a) Picture of PCX. A  $\text{LaB}_6$  cathode is mounted on top the vessel for volumetric flow drive experiments. The Fabry-Pérot spectrometer is located on the scannable optics table under the black-out cloth. (b) A CAD drawing of PCX. Two cryogenic pumps are located at the bottom with a turbo molecular pump mounted on top. The horizontal box port has a window for optical diagnostics. KF40 ports are used for probes, cathodes, and anodes.

PCX is a small versatile experiment that is perfect for testing diagnostics. The simple cylindrical geometry is ideal for testing chord measurements requiring Abel inversions. The upgraded Fabry-Pérot spectrometer, outlined in detail in Chapter 3, was tested and benchmarked on the scannable optics table of PCX. Details of the Fabry-Pérot measurements can be found in Chapters 4 and 5.

## 2.3 Plasma Production

The BRB is a versatile machine with many ways of producing plasmas. Originally, the main source of plasma was from hot emissive cathodes with plans to add electron cyclotron heating (ECH). Now, plasmas are also generated with ECH, plasma washer guns [22], and compact toroid injectors [23, 24]. As a result, a wide range of plasma parameters are possible in different gas species. A summary of the plasma parameters for the various plasma production sources is presented in Table 2.1.

	LaB <sub>6</sub>	ECH	Washer Guns	Compact Toroid Injector
Input Power	300 kW	40 kW	1 MW	1 GW
$n_e$ ( $10^{18} \text{ m}^{-3}$ )	0.1-2	0.01-0.3	0.1-10	0.5-50
$T_e$ (eV)	3-15	3-15	2-5	10-20
$\beta$ ( $P/P_{\text{mag}}$ )	$1 - \infty$	$1 - \infty$	0.1-100	0.1-100

Table 2.1: Plasma parameters for different plasma sources

### 2.3.1 Emissive Cathodes

Hot emissive cathodes are used to produce hot dense plasmas on both the BRB and PCX. Lanthanum hexaboride (LaB<sub>6</sub>) cathodes are heated to approximately 1700° C where its work function is very low and becomes a strong electron emitter. The cathodes are biased with respect to cold molybdenum anodes to strike a discharge. Primary electrons (100-400 V) emitted from the cathode collide with neutral atoms starting a cascade of ionization creating the plasma.

On the BRB, there are 12 installed cathodes. Each cathode has a graphite filament heater isolated from the LaB<sub>6</sub>. The heater is described in detail in Dave Weisberg's thesis work [20]. On PCX, a single LaB<sub>6</sub> cathode modified for deeper insertion is mounted on the top of PCX on the central axis. Each cathode is biased with its own 36 kW switching DC power supply with a maximum current of 120 A. The power supply has an initial breakdown feature allowing the voltage to rise up to  $\sim 1$  kV to assist with plasma breakdown. With this system, plasmas have been created with upwards of 300 kW of injected power from LaB<sub>6</sub> cathodes.

### 2.3.2 Electron Cyclotron Heating

Plasmas can be produced via high power microwaves. Currently, there are three 20 kW magnetrons operating at 2.45 GHz continuous wave (CW) installed on the BRB. These magnetrons operate at the same frequency as a standard microwave oven found in your kitchen, only 5-10x stronger. Depending on the input power and neutral fill pressure, plasmas can become over-dense where the electron density exceeds the cutoff density ( $7.75 \times 10^{16} \text{ m}^{-3}$ ) for 2.45 GHz. Breakdown is achieved by having electrons in the neutral gas resonate with the wave and the permanent magnetic field at 875 G. More details regarding the electron cyclotron heating (ECH) system and plasmas produced by it are presented in Appendix C.

### 2.3.3 Plasma Washer Guns

Electron cyclotron heating and emissive cathodes are designed for long duration plasmas. Other sources are used for pulsed experiments. The plasma washer guns create dense plasmas with a 10 ms duration. The plasma guns used on the BRB are the same array used on the Rotating Wall Machine (RWM) and the Line-tied Reconnection Experiment (LTRX). The plasma gun is coaxial with a cathode at the end where the gas is injected with an anode at the front. Molybdenum washers are placed coaxially and separated with boron nitride washers to help with breakdown. The discharge is initialized with a type-E pulse forming networking with an impedance of  $0.1 \Omega$  that lasts for 10 ms. The washer gun is a floating circuit that can be biased relative to an external anode to draw axial current through the plasma.

### 2.3.4 Compact Toroid Injector

Two compact toroid (CT) injectors are routinely used on the BRB for studying shock phenomena. The CT injector is a magnetized coaxial plasma gun consisting of two cylindrical electrodes. A bias coil supplies an initial poloidal field. The electrodes are biased via a high voltage capacitor bank with a low inductance design to create the initial plasma. The self-Lorentz force accelerates the plasma down the barrel at very high velocities  $\sim 100$  km/s. The very dense plasma leaves the magnetic barrel as a compact toroid that can expand into the BRB vessel to densities on the order of  $\sim 10^{19}$  m<sup>-3</sup>.

## 2.4 Diagnostics

The BRB has a large suite of diagnostics for probing various plasma properties. Electrostatic probes such as Langmuir and Mach are inserted into the plasma, but can perturb the plasma by increasing the plasma loss area and be a source of impurities. As a result, non-invasive diagnostics such as optical emission spectroscopy, mm-wave interferometry, and a Fabry-Pérot spectrometer were developed.

### 2.4.1 Single Tip Swept Langmuir Probe

A Langmuir probe consists of a metal tip (planar, cylindrical, etc.) inserted into the plasma and biased to draw current from the plasma. When the probe is biased negatively well below the floating potential,  $V_f$ , the probe is collecting ion current equal to the ion saturation current,  $I_{\text{sat}} = 0.6 n_e C_s A$ , where  $n_e$  is the electron density,  $C_s$  is the sound speed, and  $A$  is the probe area neglecting sheath effects. When the probe is biased well above the floating potential, the probe is collecting electron saturation current. Between those extremes, the current can be described by

$$I = I_{\text{sat}} \left( 1 - e^{(V-V_f)/T_e} \right) \quad (2.1)$$

[25]. There are a cornucopia of non-ideal effects that modify the ideal case in Eq. 2.1 including but not limited to sheath expansion, probe geometry, and hot electron populations [26].

Our Langmuir probe is biased with a sweeping voltage ranging from  $-120$  V to  $+30$  V using a power amplifier circuit. The current to the probe is measured with a line resistor and an isolation amplifier circuit designed by Mikhail Reifman widely used at WiPPL. The voltage is measured across a 30:1 voltage divider with another isolation amplifier.

### 2.4.2 Triple Probe

A triple probe is a three tipped probe inserted into the plasma to measure the plasma density, electron temperature, and floating potential. The main advantage of a triple probe over a voltage-swept Langmuir probe is that electron temperature, density, and floating potential can be estimated for a single time point instead of an average over a voltage sweep. This is extremely useful for fast fluctuating plasmas or when a ground referenced probe is not ideal because the plasma potential is extremely negative.

The operation of a triple probe is extremely simple compared to a Langmuir probe. A voltage is applied between two of the tips and the third tip is left floating in the plasma. The negatively biased tip collects ion saturation current and the positively biased tips collect an equal amount of electron current. From the ion saturation current, the plasma density can be inferred. The electron temperature is equal to the voltage between the positively biased tip and the floating tip divided by  $\ln(2)$ . The equation describing the current balance is given by

$$-I_{\text{sat}} = I_{\text{sat}} \left(1 - e^{e\Delta V/k_b T_e}\right) \quad . \quad (2.2)$$

The floating potential is measured via a voltage divider on the floating tip to ground. A diagram of the circuit can be seen in Fig. 2.5.

### 2.4.3 Mach Probe

Plasma flow can be measured by inserting Mach probes into the plasma. A Mach probe consists of two planar surfaces oriented perpendicular to the flow and biased negatively. The surface facing upstream collects more current than the oppositely directed surface. The mach number ( $M =$

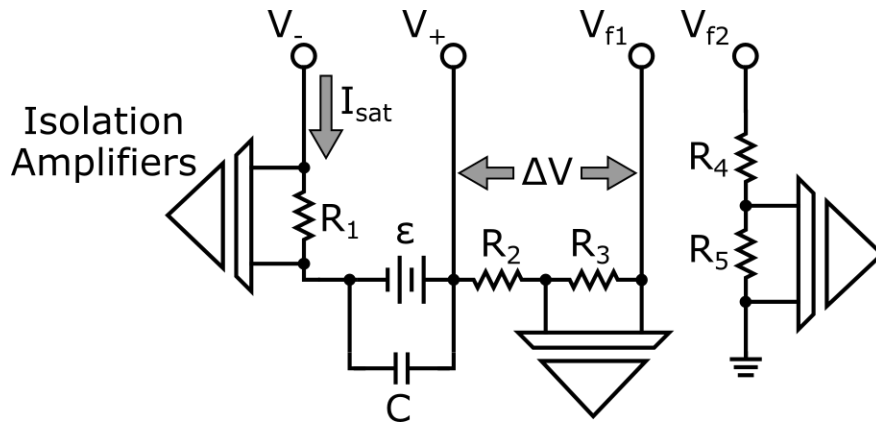


Figure 2.5: Electronic schematic of a triple probe circuit. Two floating tips ( $V_-$  and  $V_+$ ) are biased with voltage,  $\epsilon$ . The ion saturation current is measured over resistor,  $R_1$ . The electron temperature,  $T_e$ , is extracted by measuring the voltage difference between  $V_+$  and  $V_{f1}$  using a voltage divider. The floating potential,  $V_f$  is by a separate ground referenced voltage divider. Credit: Figure created by Ethan Peterson.

$V/C_s$ ) of the flow, the ratio of the velocity to the sound speed, is given by

$$M = 0.45 \ln \left( \frac{I_{up}}{I_{down}} \right) \quad (2.3)$$

where  $I_{up}$  is the upstream current and  $I_{down}$  is the downstream current [25]. The difference in probe area between the tips is calibrated by flipping the probe for two consecutive discharges and calculating an offset Mach number. In general, Mach probes have uncertainties on the order of  $\sim 0.5$  km/s which is ideal for fast flows. For flows below a km/s, high-resolution spectroscopic measurements inferring the velocity from Doppler shifts are better suited. Additionally, mach probes can be hard to interpret due to non ideal effects. For large bias voltages and large Debye lengths, the downstream probe can collect more current than the upstream probe [27, 28]. For PCX and BRB plasmas, the Debye lengths are small compared to the probe size.

#### 2.4.4 3-Axis Hall Probe Array

Magnetic fields are measured at WiPPL using linear arrays of 3-axis Hall probes developed by Ethan Peterson in his thesis work [29]. The probe array consists of 15 probes each measuring all

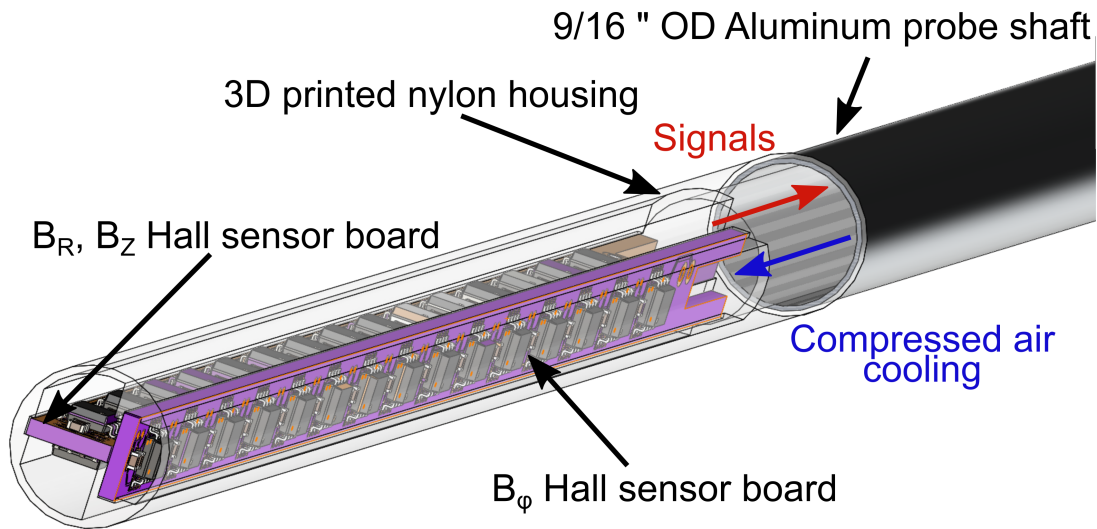


Figure 2.6: Linear array of 3-axis Hall probes with 1.5 cm spacing.  $B_R$  and  $B_z$  are mounted on opposite sides of a printed circuit board.  $B_\phi$  is located on a second printed circuit board perpendicular to the first. A 3D printed nylon housing was designed by E. Peterson to help with board alignment. The probe array is inserted in a quartz dip tube to measure magnetic fields in the plasma and is air cooled.

3 directions of the local magnetic field. The probe is inserted inside a quartz dip tube with forced air cooling to keep the probes from overheating from the plasma particle flux heating the quartz tube. There are two sensitivities depending on the the probe construction. The upgraded version used for volumetric flow drive experiments on PCX has 9 high sensitivity (28 mV/G) probes and 6 low sensitivity (10 mV/G) probes separated by 1.5 cm. The upgraded version is inserted into a 3D printed nylon housing for better alignment of the PCB boards. A CAD drawing of the upgraded Hall probe array is presented in Fig. 2.6.



where  $\omega$  is the angular frequency of the wave,  $c$  is the speed of light,  $n_c$  is the cutoff density for the wave,  $n_e$  is the electron density, and  $dl$  is the infinitesimal path length in the plasma [25].

The phase lag induced by the plasma is measured and analyzed by an FPGA. The mixers preserve the phase of the signals and output a new signal at the intermediate frequency. That signal is passed through a comparator circuit to give a digital signal that can be digitized by the FPGA. A algorithm run on a LabView field programmable gate array (FPGA) developed by Carl Wahl parses the two digital signals and calculates the phase difference in real time. The algorithm determines the phase in units of  $\pi$ . A phase difference of  $\pi$  corresponds to a density of  $2.4 \times 10^{17} \text{ m}^{-3}$  assuming a uniform density along the chord through the plasma. The upper density limit ( $1.3 \times 10^{21} \text{ m}^{-3}$ ) is set by the cut-off density for the wave traveling through the plasma. The density resolution depends on the clock frequency of the FPGA and the intermediate frequency. For a clock frequency of 200 MHz and an intermediate frequency of 1 MHz, the FPGA has 200 divisions for a fringe giving a density resolution of  $1.2 \times 10^{15} \text{ m}^{-3}$ . After the shot is finished, the data is saved to permanent storage and used to convert phase to plasma density.

## 2.4.6 Optical Emission Spectroscopy

Optical emission spectroscopy (OES) measures the passive spectra emitted by the plasma to infer properties about the plasma [30, 31, 32]. At WiPPL, the OES diagnostic consists of a compact USB spectrometer from Ocean Optics and a fiber-coupled collimator for the collection optics. In a coronal model [33], a free electron collides with a ground state atom exciting a bound electron to a higher energy state. Before the atom can interact with the plasma again, the electron relaxes back to the ground state spontaneously emitting photons at discrete energies. The emissivity for an emitted wavelength from upper state  $i$  to lower state  $j$  is given by

$$\epsilon \propto \Gamma_{ij} n_g n_e \langle \sigma v_e \rangle \quad (2.5)$$

where  $\Gamma_{ij}$  is the branching fraction,  $n_g$  is the ground state density for the atom,  $n_e$  is the electron density, and  $\langle \sigma v_e \rangle$  is the excitation cross-section.

The excitation cross-section depends on the electron distribution function and ideally could be used to estimate the electron temperature,  $T_e$ . In practice on the BRB and PCX, this is not ideal because of the injected primary electrons. The cross-section has a threshold energy for excitation and is most sensitive to the tail population of the electron distribution function. In other experiments, OES has successfully been used to measure electron temperature.

On the BRB, OES has been used to measure the profile of the neutral population [34]. Neutrals are diffusing inward from the wall and being ionized by the plasma. Due to geometric effects, one would expect there to be fewer neutrals in the center compared to the edge of the plasma. This diffusion process can be described by

$$\frac{\partial N_n}{\partial t} + \nabla \cdot \vec{\Gamma} = S_{\text{recomb}} - S_{\text{ion}} - S_{\text{CX}} \quad (2.6)$$

where  $\Gamma$  is the particle flux that obeys Fick's Law,  $S_{\text{recomb}}$  is the recombination rate,  $S_{\text{ion}}$  is the ionization rate, and  $S_{\text{CX}}$  is the charge-exchange rate.  $S_{\text{recomb}}$  is small for BRB plasmas and can be ignored.  $S_{\text{CX}}$  behaves similarly to ionization because a charge-exchange neutral becomes a fast neutral that leaves the plasma hitting the wall before it can interact with the plasma. The source terms have the form,  $n_n n_e \langle \sigma v_e \rangle$ , where the  $\langle \rangle$  denotes the average over the electron distribution function. Assuming steady-state with neutrals diffusing according to Fick's Law in a sphere with only radial dependence, the neutral density profile is given by

$$N_n(r) = N_n(R_{\text{edge}}) \left( \frac{R_{\text{edge}}}{r} \right) \frac{\sinh(r/d)}{\sinh(R_{\text{edge}}/d)} \quad (2.7)$$

where  $R_{\text{edge}}$  is the plasma edge,  $N_n(R_{\text{edge}})$  is the edge neutral density, and  $d$  is the neutral depletion length. The form for the depletion length is

$$d = \sqrt{\frac{D_n}{(\langle \sigma v \rangle_{\text{ion}} + \langle \sigma v \rangle_{\text{CX}}) n_e}} \quad (2.8)$$

where  $\langle \sigma v \rangle_{\text{ion}}$  is the ionization cross section,  $\langle \sigma v \rangle_{\text{CX}}$  is the charge exchange cross section, and  $D_n$  is the neutral diffusion coefficient. A similar profile in a cylindrical geometry can be derived for PCX. However, the shortest depletion lengths measured on BRB are still on the order of the system size for PCX.

### 2.4.7 Fabry-Pérot Spectrometer

A high-precision high-throughput Fabry-Pérot spectrometer has been developed for measuring ion temperatures and flows. The passive spectra is measured through an étalon that produces an interference pattern consisting of concentric rings. The rings can be analyzed to infer the ion distribution function. The diagnostic was originally designed by Fred Roessler and Chris Cooper, but was redesigned during my thesis work to enable higher time resolution with a new calibration procedure yielding accurate absolute wavelength calibrations. The diagnostic and analysis procedure are discussed in detail in Chapter 3.

## 2.5 Experimental Workflow and Data Acquisition

### 2.5.1 Control Software

The experiments are controlled by a LabView application that interfaces with the various equipment in the lab for creating and measuring plasma properties. The heater voltage and current for the cathodes on the BRB are digitized by a compactRIO, a National Instruments real-time computer system, and logged to a MySQL database. On PCX, LabView communicates with Arduino micro-controllers sending commands to power supplies. In addition, custom electronics were designed and built in-house to control various equipment.

### 2.5.2 Data Acquisition

Data is digitized at 250 kHz with 16 bit resolution on ACQ196 digitizers from D-tAcq Solutions. The digitizers are armed by shell scripts and triggered via the 20 Channel trigger box controlled by the LabView field-programmable gate array (FPGA). After a shot, the data is uploaded to the MDSplus [35] data server. The data is stored in the tree structure show in Fig. 2.8. In addition to storing raw data, nodes in the MDSplus tree have formulas referencing other nodes in the tree to compute processed values such as cathode current without having to store the data multiple times.

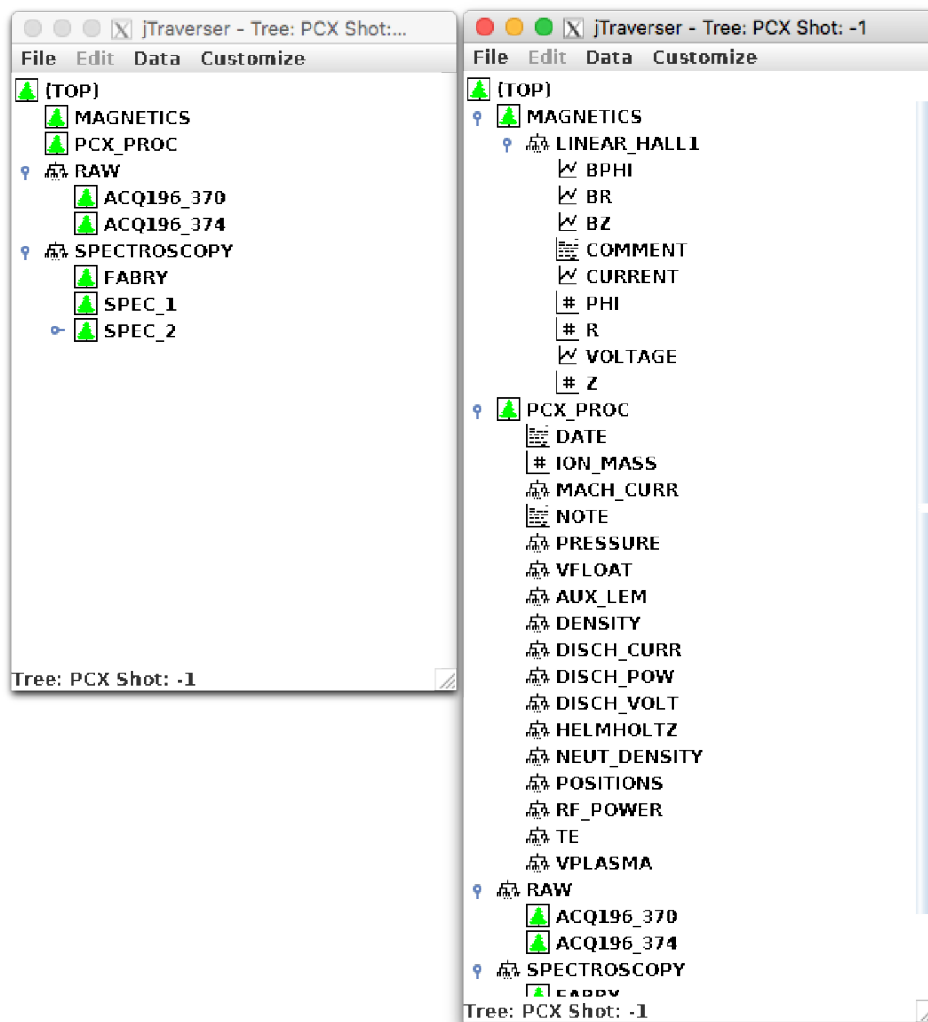


Figure 2.8: MDSplus tree structure for PCX. Raw data and processed data are stored in the top level PCX tree.

### 2.5.3 Data Visualization

Normally, data stored in MDSplus was viewed in a Java application called jScope [36]. Due to the long time duration at high digitization rates, jScope crashing became a significant hurdle for viewing data between shots. In response, I developed a python application with a GUI using the Qt framework utilizing Matplotlib [37] for displaying the data shown in Fig 2.9. It has a number of the same features from jScope. It utilizes the MDSplus thin client to retrieve data so the user does

not need to maintain a list of tree environment variables on their local machine. Data is retrieved with parallel calls to MDSplus to speed up large data transfers. In addition, data is cached locally to allow going back and forth through a series of shots looking for signal changes. For speed of plotting, data is decimated by default and the decimation is updated after the user zooms on a portion of a graph. Overall, PiScope has been a successful replacement of jScope for most use cases on the BRB and PCX.

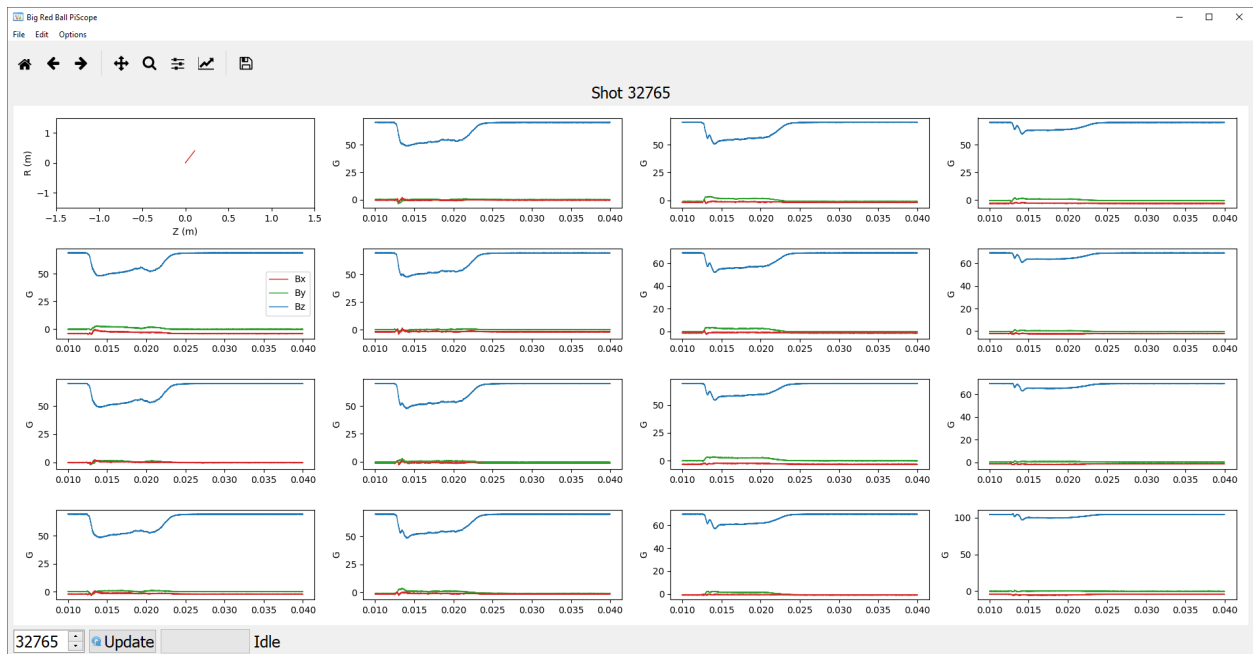


Figure 2.9: PiScope is a python app for viewing MDSplus data at WiPPL built to replace jScope. Shown here is the main window with 15 3-axis magnetic field measurements along with the location of each probe in the R-Z plane.

## Chapter 3

### A spectrometer for high-precision ion temperature and velocity measurements in low-temperature plasmas

Many processes and behaviors of low-temperature plasmas are heavily influenced by ion dynamics. Some examples include sheath expansion by warm ions [38, 39], atmospheric pressure plasmas and their medical applications for ions near room temperature [40], and the transport of momentum via kinematic viscosity in flowing plasmas. In each of these examples, it is extremely important to have a measurement of the ion temperature and velocity distribution in order to correctly predict and model behavior. In the case of flowing plasmas, Braginskii [9] developed a formula for kinematic viscosity using collisional theory showing that the momentum of an unmagnetized plasma diffuses at a rate set by the ion thermal speed,  $v_{Ti}$ , and the ion-ion collision time,  $\tau_{ii}$ . This combination of terms results in a particularly strong,  $T_i^{5/2}$ , dependence on the ion temperature. Propagating the error of a given ion temperature measurement to the resulting viscosity illustrates the need for precise measurements for estimating the theoretical value. For example, a singly-charged argon plasma with an ion temperature relative uncertainty of 10% and an electron density relative uncertainty of 10% (both reasonable uncertainties for well-diagnosed laboratory plasmas) yields a 27% uncertainty in the theoretical value of Braginskii viscosity. This level of error can greatly affect results of modeling flows in experimental data [19]. In a similar fashion, the viscosity can be experimentally determined from spatially resolved measurements of velocity that require accurate flow measurements. Motivated by the desire for accurate viscosity measurements and the ability to compare with theory, we have developed a high precision velocity and ion temperature diagnostic, which is applicable to many other low-temperature plasma applications.

Measurements of ion temperature and ion flow in the low-temperature regime can be quite challenging. Traditionally, basic plasma experiments have been diagnosed with probes inserted into the plasma. The flow velocity can be measured with a Mach probe [41, 42, 43, 27] and interpreted as an absolute velocity using the local sound speed measured by a Langmuir probe. The ion temperature is more difficult to measure with a probe. Retarded field energy analyzers (RFEA) [44, 45, 46] can be used to measure the ion energy distribution function directly, but shielding out the electrons is difficult. Probes can also be detrimental to the plasma performance by increasing loss area, sputtering of particles, and outgassing leading to a decrease in conductivity and an increase in neutral drag. Laser induced fluorescence (LIF) [47, 48] is another option, but it is expensive, more complicated, and has low time resolution. In addition, it is possible for the metastables to be produced from ionization instead of from ground state excitation [49]. Ion temperature and flows can be measured non-invasively by using optical diagnostics that are sensitive to both velocity and velocity shear. Straight forward measurements of ion emission require high resolution spectrometers and can suffer from lack of light with insufficient étendue.

In this chapter, we describe a high-throughput and simple-to-implement spectrometer capable of measuring the very small Doppler shifts and broadening of low-temperature plasmas, using a Fabry-Pérot étalon and a digital camera. Previous measurements with the Fabry-Pérot spectrometer demonstrated the ability to measure ion temperatures as low as room temperature up to a few eV [50, 51]. This chapter focuses on the design decisions and analysis for a complete overhaul of the Fabry-Pérot spectrometer. The diagnostic redesign included the use of a large cross section, high numerical aperture fiber and collimator and a rail mounted assembly resulting in a higher étendue spectrometer that is easy to align and is portable between the different laboratory spaces at the Wisconsin plasma physics laboratory (WiPPL) [50].

### 3.1 Fabry-Pérot Basic Theory

A Fabry-Pérot étalon consists of two parallel highly reflective plates separated by some distance,  $d$ . If the light entering the cavity satisfies the interference condition, then sharp circular rings are observed when the exiting light is focused. Light entering the étalon at angle  $\theta$  as shown

in Fig. 3.1 has a phase shift after two reflections given by

$$\phi = 2((2\pi nd \cos \theta / \lambda) - \psi) \quad (3.1)$$

where  $n$  is the index of refraction for air,  $\lambda$  is the wavelength of light, and  $\psi$  is the phase angle from reflection (0 or  $\pi$ ). The  $m^{\text{th}}$  ray exiting the cavity has an electric field given by

$$E_m = (A_i e^{j\omega\tau}) t^2 r^{2(m-1)} e^{-j\phi(m-1)} \quad (3.2)$$

where  $t$  is the transmission coefficient,  $r$  is the reflection coefficient, and  $A_i$  is the initial amplitude. The total electric field,  $E_{\text{total}}$ , after focusing the rays is the sum over all the rays exiting the cavity and is given by

$$E_{\text{total}} = \sum_{m=1}^{\infty} E_m = A_i t^2 r^{-2} e^{j(\omega\tau + \phi)} \sum_{m=1}^{\infty} (r^2 e^{-j\phi})^m = \frac{A_i t^2 e^{j\omega\tau}}{1 - r^2 e^{-j\phi}}. \quad (3.3)$$

The intensity of light,  $I$ , is given by

$$\begin{aligned} I &= E_{\text{total}} E_{\text{total}}^* = \frac{A_i^2 t^4}{1 + r^4 - r^2 e^{-j\phi} - r^2 e^{j\phi}} \\ &= \left( \frac{T^2}{(1 - R)^2} \right) \frac{I_i}{1 + \frac{4R}{(1-R)^2} \sin^2 \left( \frac{\phi}{2} \right)} \end{aligned} \quad (3.4)$$

where  $I_i$  is the initial intensity of the light ray entering the cavity,  $T = t^2$ , and  $R = r^2$ . The observed intensity pattern is at a maximum when the phase difference from reflections in the cavity is an integer multiple of  $2\pi$ .

The finesse,  $\mathcal{F}$ , is the ratio of the distance separating the peaks divided by the full-width at half-maximum of the peaks. The theoretical finesse is given by

$$\mathcal{F} = \frac{\pi}{2} \sqrt{\frac{4R}{(1-R)^2}} = \frac{\pi R^{1/2}}{1-R} \quad (3.5)$$

and is only a function of the quality of the mirrored interior surfaces. In practice, the finesse is reduced due to other effects including but not limited to surface flatness and non-parallelness of the plates. For our étalon, the theoretical maximum is around 30 but in practice is between 20 and 22.

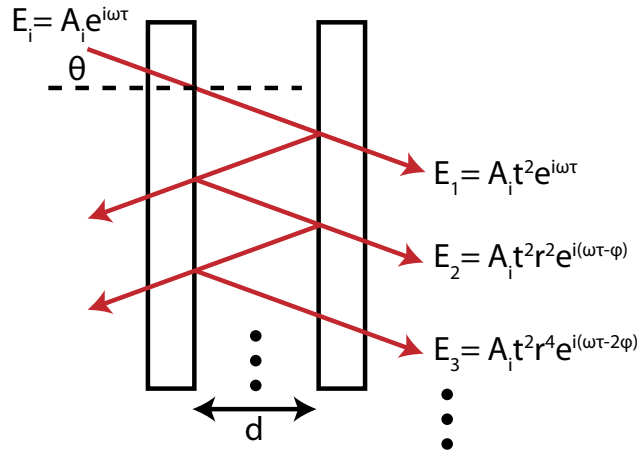


Figure 3.1: Ray enters the étalon and reflect many times on the inner parallel surfaces. At each reflection, a portion refracts through and exits at the same initial angle.

### 3.2 Design Considerations for high-resolution spectroscopy

Measuring ion temperatures below a few eV and velocities below 10 km/s spectroscopically in the visible range requires a spectrometer with a resolution of the order of a picometer. For low electron temperature plasmas ( $T_e < 10$  eV) at moderate densities ( $n_e \approx 10^{18} \text{ m}^{-3}$ ), ion emission in the visible spectrum is weak. Measurements could be made in the VUV, but then the spectrometer becomes an integral part of the vacuum vessel which can complicate adjustments and calibration. The combination of low radiance and the need to resolve ion equilibrium time dynamics sets the requirements for the light gathering capability of the diagnostic. These requirements can be satisfied by a traditional grating spectrometer, but a Fabry-Pérot spectrometer is more compact and has a simpler optical design that can be implemented at lower cost.

One of the first design considerations is the spatial resolution of the chord measurement. For typical plasmas at WIPPL, the electron density and temperature is uniform except for a steep edge gradient. For expected ion temperatures, the velocity gradient scale length is on the order of about 30 cm, so the spatial resolution requirements are modest. Therefore, the maximum optical throughput is set only by the optical access to the plasma which is constrained by the magnet spacing and

port size. The magnet spacing allows the use of two-inch collection optics which provide adequate light collection with sufficient resolution of velocity gradients. The light is collimated by the collection optics and transmitted over a fiber to the spectrometer. The collimator is attached to a linear stage mounted on a box port with a large window to allow many different views of the plasma cross section and to decouple the alignment of the diagnostic from the plasma view. To maximize the light collection, a large core diameter, high numerical aperture (NA) fiber was chosen to maximize the étendue,  $G = \pi S (\text{NA})^2$ . A multi-fiber bundle could also be used, but the packing fraction must be considered. The large NA requires very fast (low  $f/\#$ ) optics requiring aspherical lenses for collimation to limit spherical aberrations.

The main optical element in a Fabry-Pérot spectrometer is an étalon consisting of two highly reflective parallel plates separated by a small distance  $d$ . The high reflectivity allows for light to reflect many times before exiting the cavity. For a given wavelength,  $\lambda$ , the interference condition is given by

$$m\lambda = 2nd \cos \theta \quad m \in 0, 1, \dots, m_0 = \text{Floor} \left( \frac{2nd}{\lambda} \right) \quad (3.6)$$

where  $n$  is the index of refraction of air,  $\theta$  is the angle that light enters the étalon relative to the optical axis, and  $m$  is a nonnegative integer less than the maximum order,  $m_0$ . The light exiting the étalon is focused by a lens with focal length  $f_2$  down onto the camera sensor. The measured intensity pattern is a set of concentric rings (see Fig. 3.2) where the innermost ring corresponds to the maximum order  $m_0$ . The étalon is placed inside an optical telescope where the rays are within a small range of angles from horizontal to achieve the desired ring interference pattern.

The components in the optical assembly are chosen based on a few design criteria. As shown in Fig. 3.3, the assembly consists of a fiber with collimator, an optical telescope, an étalon placed inside the telescope, a bandpass filter, and a camera sensor. As discussed earlier, the étendue is set by the fiber and collection optics. The requirements for the detector are quite modest and depend mostly on pixel sensitivity, pixel size, and read noise. As such, the first measurements are conducted with a commercial digital camera. The camera lens with focal length  $f_2$  was chosen to have 5 sets of concentric rings such that the central ring of interest is near the optical axis away from any adverse effects such as spherical aberration. The objective lens of the telescope was

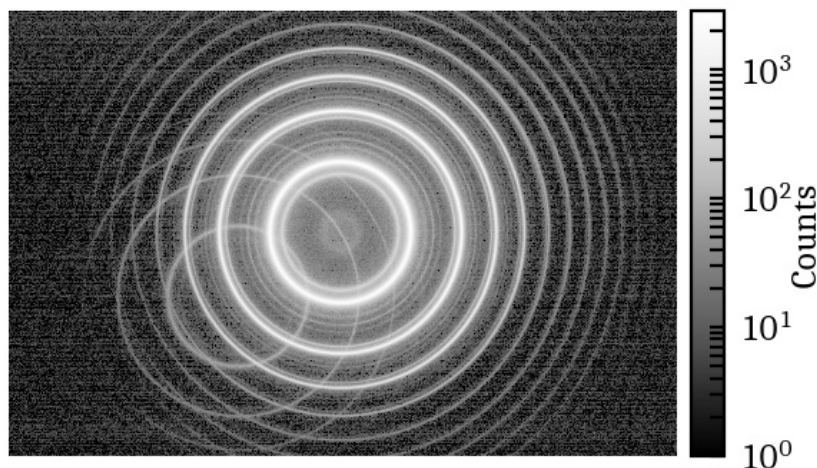


Figure 3.2: Fabry-Pérot image of Th Ar-fill hollow cathode lamp. The calibration lamp's complicated spectra in this wavelength range consists of two dominate lines (ThI 487.873302 nm, ArII 487.98634 nm) [52] and many low amplitude ThI lines. Contributions from the nuisance lines are mitigated using three Andover 1 nm FWHM bandpass filters at 488 nm. The three two-cavity filters provide a -30 dB rejection ratio of wavelengths outside twice the bandpass. The log scale emphasizes the undesirable secondary ring pattern from misalignment.

chosen to match the illuminated part of the lens from the collection optics to the sensor size. The filter must be placed in a region where the rays have a small angle with respect to the optical axis otherwise more light than expected will pass through the filter. A picture of the assembled diagnostic can be see in Fig 3.3.

Achieving good alignment of the Fabry-Pérot spectrometer is crucial for high spectral resolution. Alignment requires all elements centered on, and perpendicular to, the optical axis. If any of the components are offset from the optical axis the intensity profile will be shifted from the center of the image plane resulting in rings lacking azimuthal symmetry in intensity. The étalon plates can be made parallel with three adjustment screws controlling the amount of pressure applied via springs. The camera sensor must be placed such that the sensor images at infinity, otherwise the

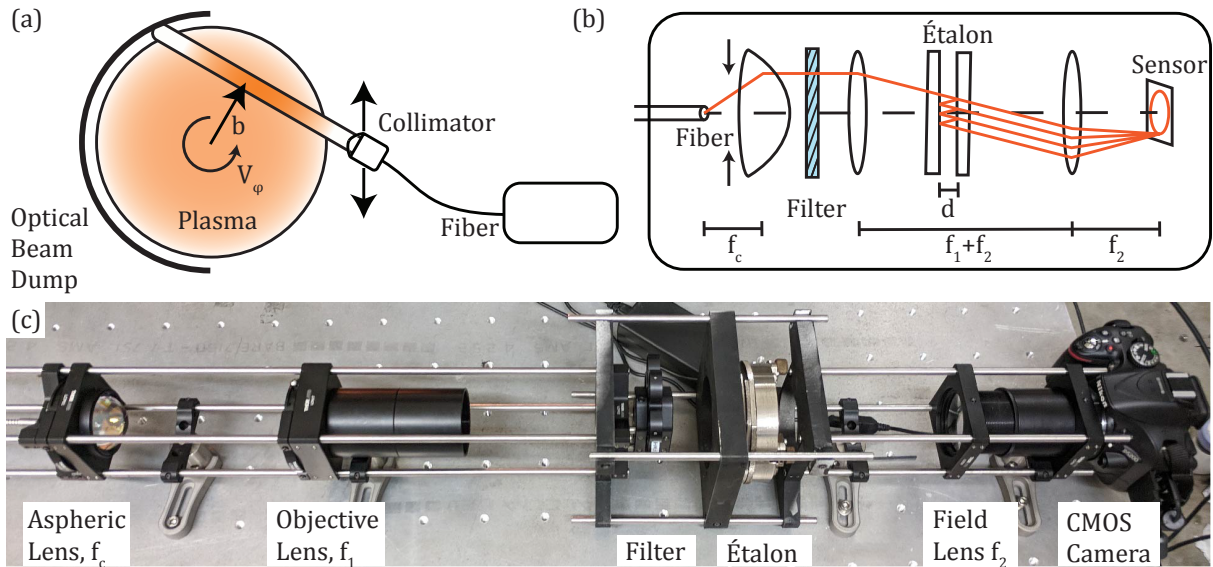


Figure 3.3: (a) Fabry-Pérot optical schematic. Light is collected from the plasma with a  $f/1.0$  collimator mounted on a linear stage to allow scanning of the plasma volume. The chord's closest distance to the origin is labeled by its impact factor,  $b$ . An optical beam dump is located on the far side of the vessel to limit reflected light from entering the collimator. (b) Optical Schematic of Fabry-Pérot. (c) Picture of Fabry-Pérot. Light from the fiber is collimated by a  $f/1.0$  collimator and focused by the objective lens ( $f_1 = 350$  mm) onto 5 mm spot size on the étalon ( $d = 0.88$  mm). The light exiting the étalon is focused onto the CMOS sensor via the field lens ( $f_2 = 150$  mm) as concentric rings due to the interference condition (Eq. 3.6). All lenses are 50.8 mm in diameter and the camera is a 24 MP Nikon D5200 digital camera.

rings will be out of focus and extra Gaussian broadening will need to be accounted for in the analysis. With the high-throughput collection optics, these effects are reduced *in situ* by collecting light from a calibration lamp and observing the ring pattern while adjusting the placement of each optical element.

### 3.3 Image Processing

The model for intensity on the sensor is a function of wavelength and pixel distance relative to the center of the concentric rings. To increase signal-to-noise and decrease the number of pixels (24 million) in the calculation, a technique called annular summing [53, 54] is used where pixels are binned into annuli with equal area. The location of the  $n^{\text{th}}$  bin edge is given by

$$r_n = \sqrt{n(2r_N - \Delta)\Delta} \quad n \in 0, \dots, N \quad (3.7)$$

where  $r_N$  is the largest bin radius and  $\Delta = r_N - r_{N-1}$ . Each pixel in a bin can be treated as an independent identically distributed measurement because the count rate on a particular pixel is uncorrelated with other pixels. For each annuli, the mean and standard deviation of the mean are calculated from the histogram of points in an annulus to account for differences in the number of pixels in each annulus from mapping discrete pixels to annuli. Pixels that have counts outside  $\pm 3$  standard deviations from the mean are treated as outliers and discarded.

Before the final annular sum can be analyzed, the center of the ring pattern must be known to within a few tenths of a pixel. The center is determined by iteratively performing annular sums on halves of the CCD based on an initial center-of-mass estimate. A new center guess is calculated based on the misalignment of the individual peaks. This procedure is iterated until a threshold for the next step size is met. A portion of an annular sum is shown compared against the raw pixel intensities in Fig. 3.4. The expected noise is mostly from photon counting statistics. The read noise and dark counts are on the order a few counts each. With annular summing, small features and overlapping peaks are identifiable with a significant increase in signal to noise ( $\approx 50\times$ ).

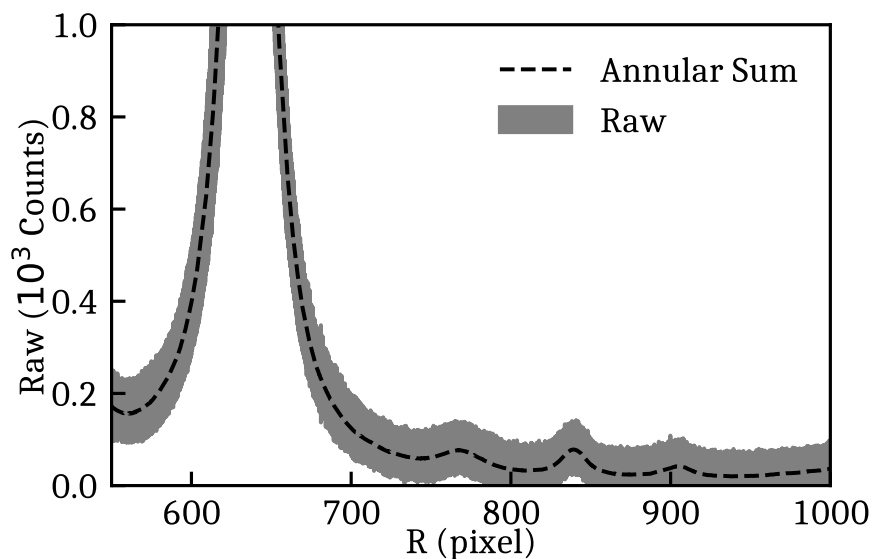


Figure 3.4: Intensity in counts is shown as a function of radius from the center of the ring pattern. The noise is the result of mostly photon counting statistics. The read noise and dark counts are on the order of a few counts. Annular Summing reduces the uncertainty of the mean counts in a bin to approximately 1 count.

### 3.4 Bayesian Method for Analysis

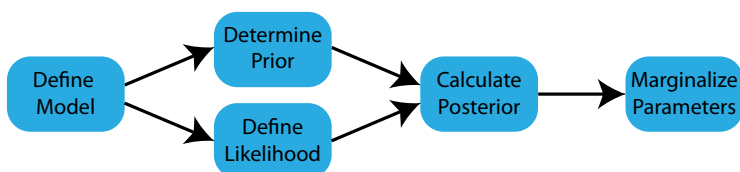


Figure 3.5: Procedure for solving a problem with a Bayesian approach.

The following section outlines the procedure implemented to calibrate the spectrometer using the Bayesian methodology illustrated in Fig. 3.5. An introduction to the probability math and overview of the analysis is given in Appendix A. First, a model for generating spectra is chosen. Each pixel is considered to be an independent measurement and have a probability likelihood distribution equal to a Normal distribution with mean and standard deviation estimated from the

annular summing technique described in Sec. 3.3. The prior probability distribution is determined from known physical constraints on parameters such as "temperatures are positive." Finally, the posterior distribution is found via a Monte Carlo calculation which draws samples from the prior distribution and evaluates the likelihood. Any extra parameters in the model, such as amplitudes or offsets, are integrated over to give marginal posterior probabilities for the parameters of interest.

**Define the Model:** The model for intensity on the sensor is a function of wavelength and pixel distance relative to the center of the concentric rings. To increase signal-to-noise and decrease the number of pixels (24 million) in the calculation, a technique called annular summing [53, 54] is used where pixels are binned into annuli with equal area. Each pixel in a bin can be treated as an independent identically distributed measurement because the count rate on a particular pixel is uncorrelated with other pixels. For each annuli, the mean and standard deviation are calculated from the histogram of points in an annulus to account for differences in the number of pixels in each annulus from mapping discrete pixels to annuli. Pixels that have counts outside  $\pm 3$  standard deviations from the mean are treated as outliers and discarded. Before the final annular sum can be analyzed, the center of the ring pattern must be known to within a few tenths of a pixel. The center is determined by iteratively performing annular sums on halves of the CCD based on an initial center-of-mass estimate. A new center guess is calculated based on the misalignment of the individual peaks. This procedure is iterated until a threshold for the next step size is met. A portion of an annular sum is shown compared against the raw pixel intensities in Fig. 3.4. The expected noise is mostly from photon counting statistics. The read noise and dark counts are on the order a few counts each. With annular summing, small features and overlapping peaks are identifiable with a significant increase in signal to noise ( $\approx 50\times$ ).

Calibration of a Fabry-Pérot spectrometer with fixed spacing and stable cavity pressure requires knowing the étalon spacing,  $d$ , and the camera focal length,  $f_2$ , for an absolute wavelength calibration and the finesse,  $\mathcal{F}$ , for the instrument point spread function. The absolute wavelength calibration is performed using spectroscopic methods because it is impossible to measure the étalon spacing to within  $\lambda/2$  to determine the absolute order number,  $m_0$ . Normally, the étalon spacing is

calibrated by placing the étalon in a chamber and scanning the pressure to vary the index of refraction. The exact spacing is not known during the pressure scan but the change in spacing is known very precisely [55]. Our constraints on time resolution where the entire spectra is measured simultaneously makes the pressure scanning technique impossible to implement and requires a fixed étalon spacing calibration procedure. The maximum possible finesse can be calculated from the reflectivity of the interior surfaces of the étalon, but the effective finesse depends on other factors such as plate flatness, the parallelism of the plates, and the clear aperture.

The calibration procedure involves solving for  $f_2$ ,  $d$ , and the finesse  $\mathcal{F}$  by forward modeling the spectra from a thorium hollow cathode lamp with argon gas fill measured by the Fabry-Pérot spectrometer. Thorium was chosen because it is a heavy element with only one long-lived isotope allowing for simultaneous wavelength and point-spread function calibrations. The point-spread function, PSF, is given by

$$\text{PSF}(\lambda) = \left( 1 + \left[ \frac{2\mathcal{F}}{\pi} \sin \left( \pi \frac{2nd \cos \theta}{\lambda} \right) \right]^2 \right)^{-1} \quad (3.8)$$

and at a maximum when the interference condition defined in Eq. 3.6 is satisfied. The point-spread function can easily be mapped to pixel radius  $r$  by using the trigonometric relationship:

$$\cos \theta = \frac{f_2}{\sqrt{f_2^2 + r^2}} \quad (3.9)$$

Finding the étalon spacing,  $d$ , to the precision needed is difficult because the uncertainties in the measurements lead to finding many solutions corresponding to adjacent order numbers. To solve this issue, a Bayesian approach called Multimodal Nested Sampling is used which is encoded in the software package MultiNest [56, 57, 58, 59] which was adapted from the Nested Sampling algorithm [60]. This method finds the probability distribution which best describes the uncertainty in the calibration parameters conditioned upon background information that constrains the reasonable range for these parameters. Our analysis uses a mostly non-informative prior except for highly informed edges to limit the scope of the Monte Carlo search since it is a computationally expensive procedure.

The goal of calibration is to calculate the marginal posterior probability distribution for  $f_2$ ,  $d$ , and  $\mathcal{F}$  given a hollow-cathode lamp spectrum. The model for the calibration spectrum consists

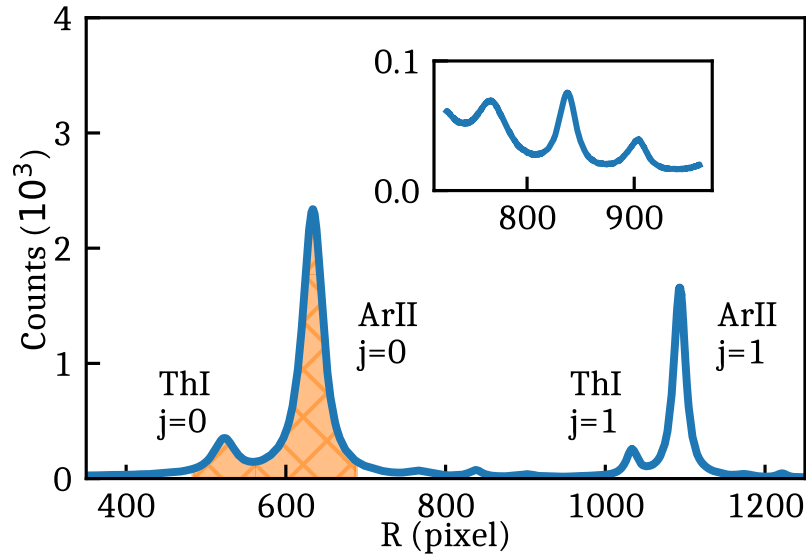


Figure 3.6: Annular sum of the Th-Ar hollow cathode lamp using the 3 Andover 1nm FWHM bandpass filters at 488 nm to reduce contributions from weak Th I lines. A Th I line (487.873302 nm) and an Ar II line (487.98634 nm) have been identified for their first and second relative order numbers. The orange region represents a calibration fit and shaded for emphasis. INSET: The central peak is a Th I line (487.800942 nm). The two remaining peaks are thought to consist of multiple unresolved lines.

of 6 parameters: the camera focal length,  $f_2$ , the étalon spacing,  $d$ , the finesse,  $\mathcal{F}$ , the Ar II amplitude  $A$ , the Th I amplitude relative to the Ar II amplitude  $A_{\text{rel}}$ , and the Ar ion temperature,  $T_i$ . The thorium temperature is assumed to be 1000 K<sup>1</sup>; however, the modeled spectrum shows very little change when varying the temperature from room temperature up to 2000 K. These calibration parameters will be noted as  $\theta_C$  for brevity. As noted in Fig. 3.6, three filters are used to limit the contribution from nearby Th I peaks so that the tails of the dominant lines due to the Lorentzian point-spread function can be distinguished. The goal of performing the calibration is to acquire sufficiently precise data to minimize the uncertainty in  $f_2$ ,  $d$ , and  $\mathcal{F}$ . The marginal

<sup>1</sup>based on correspondence with F.L. Roesler

posterior probability distribution for these calibration parameters is given by

$$p(f_2, d, \mathcal{F}|\{C_r\}, I) = \int p(\theta_C|\{C_r\}, I) dA dA_{\text{rel}} dT_i \quad (3.10)$$

where  $\{C_r\}$  represent the set of calibration measurements at each radii,  $I$  is any additional background information such as known wavelengths, and  $p(\theta_C|\{C_r\}, I)$  is the posterior probability distribution including extra parameters, such as amplitudes, needed for modeling the spectrometer image of the calibration lamp spectra. The full marginal posterior in Eq. 3.10 can be rewritten using Bayes' theorem [61, 62] as

$$p(\theta_C|\{C_r\}, I) = \frac{p(\{C_r\}|\theta_C, I)p(\theta_C|I)}{p(\{C_r\}|I)} \quad (3.11)$$

where  $p(\{C_r\}|\theta_C, I)$  is the likelihood,  $p(\theta_C|I)$  is the prior probability, and  $p(\{C_r\}|I)$  is the evidence. We follow the flowchart in Fig. 3.5 to determine the calibration parameters and their uncertainties from  $p(\theta_C|\{C_r\}, I)$ .

**Define the prior:** The prior probability consists of 6 independent uniform distributions—one for each parameter. The prior distribution used for  $f_2$  is a uniform distribution between [145.5, 154.5] mm which assumes with high confidence that  $f_2$  is within three standard deviations of the manufacturer's specification of  $150 \pm 1.5$  mm. The prior probability range for  $d$  is determined by back-lighting the étalon with a Hg lamp and counting the number of fringe orders that pass as the alignment screws are adjusted. Estimating 40 orders at 500 nm yields a shift in  $d$  of 0.01 mm giving a range of [0.87, 0.89] mm. The lower bound for the finesse is set by calculating the ratio of the distance between adjacent Ar II orders in pixels-squared and the full-width half-maximum in pixels squared. The upper bound for the finesse prior is set by estimating the ideal finesse from the reflectivity of the coating (92%) [63]. Combining these results gives us the expectation that the finesse lies in the range [20, 32]. The prior ranges for the amplitudes are set using a lower bound of 75% and an upper bound of 200% of the counts at the peak location. Very little is known about the specific conditions of the plasma inside the hollow cathode calibration lamp. A relatively naive uniform prior for the argon ion temperature ranging from room temperature to 1 eV was used. This prior for  $T_i$  is justified *post facto* since the resulting marginal posterior is Gaussian in shape and well within the prior boundaries.

**Define the likelihood:** The last component needed for calculating the marginal posterior is the likelihood probability distribution. Since each data point in  $\{C_r\}$  is characterized by a Gaussian uncertainty, a maximum entropy argument [62] for assigning a particular distribution yields a  $\chi^2$ -distribution. Since each pixel is an independent measurement, the resulting distribution is given by

$$p(\theta_C|\{C_r\}, I) = \prod_{r=1}^N \frac{1}{\sigma_r \sqrt{2\pi}} \exp \left[ -\frac{(C_r - M_C(r))^2}{2 \sigma_r^2} \right] \quad (3.12)$$

where  $M_C(r)$  is the calibration forward model for the lamp spectrum and  $\sigma_r$  is the uncertainty associated with the data point  $C_r$ .

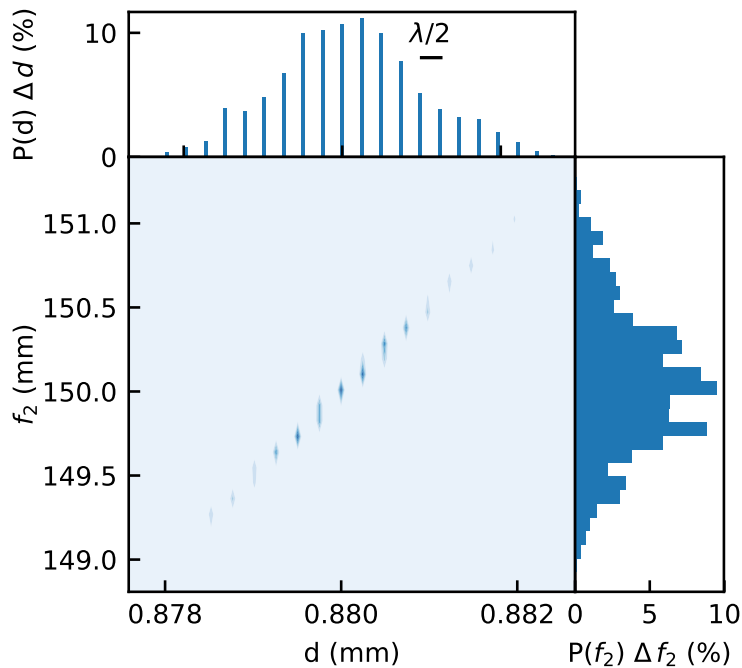


Figure 3.7: Marginal posterior probabilities for focal length  $f_2$  and étalon spacing  $d$  for a synthetic calibration. The empty space in the  $d$  posterior displays the discrete separation by  $\lambda/2$  for the possible solutions to the maximum order number. The synthetic image was created using 150 mm and 0.88 for  $f_2$  and  $d$  respectively.

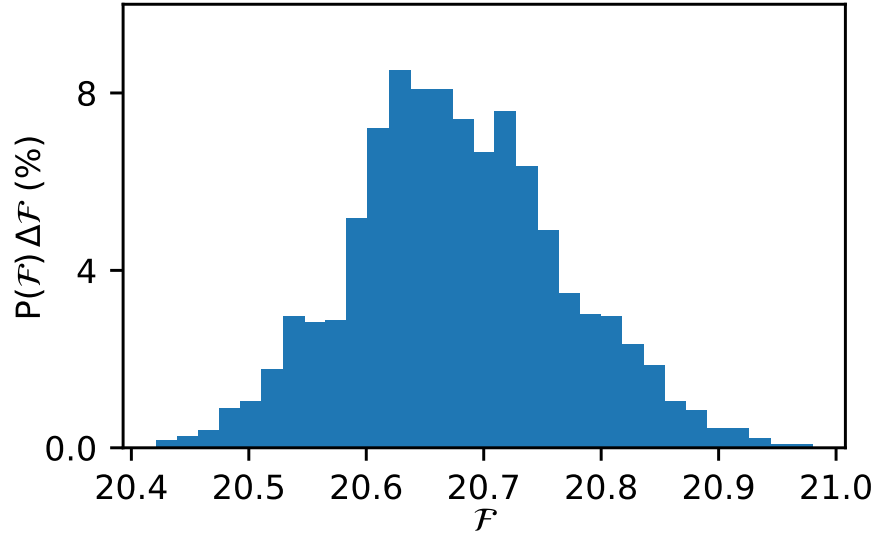


Figure 3.8: Marginal posterior probability for the finesse,  $\mathcal{F}$ , from a synthetic calibration generated with a true value of 20.7. Marginal posterior is mostly Gaussian in shape and can be described by a mean and standard deviation of 20.68 and 0.09 respectively.

**Calculate posterior and marginalize parameters:** To verify the calibration procedure, a synthetic calibration image with just two dominant peaks was generated using  $f_2 = 150$  mm,  $d = 0.88$  mm, and  $\mathcal{F} = 20.7$  for the focal length, étalon spacing, and finesse respectively. Noise was then added to the image based on photon counting statistics. The synthetic image was processed by the procedure outlined in Section 3.3. The marginal posterior results are shown in Figures 3.7 and 3.8. The joint marginal distribution for  $f_2$  and  $d$  highlights the need for multimodal nested sampling. The bin widths for the  $d$  axis are  $\lambda/10$  to show there are many possible solutions within our precision. The peaks are separated by  $\lambda/2$  which corresponds to a different maximum order,  $m_0$ . There is also a positive correlation with  $f_2$  as  $d$  is increased to the next order solution. It should be noted that this is a difficult problem to solve because of the many solutions and many regions of low likelihood. This solution was run on 240 processors on the high-performance cluster (HPC) at the UW-Madison Center for High-Throughput Computing with 1000 live points sampling over a 150 million points from the prior probability space with only 47,452 accepted points and took

approximately 18 hours to complete. Once a calibration is performed, determining the plasma flow velocity and ion temperature is much less computationally intensive.

### 3.5 Plasma Analysis

The analysis of a plasma is performed in a similar manner to the calibration. Ultimately, the goal is to calculate the marginal posterior for  $T_i$  and  $V$  given emission measurements from the plasma. This is accomplished by marginalizing over the nuisance parameters (such as the amplitude,  $A$ ) and the calibration resulting in

$$P(T_i, V | \{P_r\}, I) = \int_{\mathcal{V}} P(\theta_P, \theta_C | \{P_r\}, \{C_r\}, I) d\theta_C dA \quad (3.13)$$

where  $\theta_P$  are the plasma model parameters,  $\{P_r\}$  are the intensity measurements from a plasma image, and  $P(\theta_P, \theta_C | \{P_r\}, \{C_r\}, I)$  is the joint probability of the plasma model parameters and the calibration parameters conditioned upon all of the measurements. The integrand in Eq. 3.13 can be rewritten as

$$P(\theta_P, \theta_C | \{P_r\}, \{C_r\}, I) = P(\theta_P | \{P_r\}, \theta_C, I) P(\theta_C | \{C_r\}, I) \quad (3.14)$$

where  $P(\theta_P | \{P_r\}, \theta_C, I)$  is the marginal posterior for the plasma parameters given the calibration parameters and  $P(\theta_C | \{C_r\}, I)$  is the calibration marginal posterior determined in Sec. 3.4. The marginal posterior for the plasma parameters will be computed using MultiNest.

The posterior for the plasma parameters given a calibration can be rewritten using Bayes' theorem as

$$P(\theta_P | \{P_r\}, \theta_C, I) = \frac{P(\{P_r\} | \theta_P, \theta_C, I) P(\theta_P | I)}{P(\{P_r\} | \theta_C, I)} \quad (3.15)$$

where  $P(\{P_r\} | \theta_P, \theta_C, I)$  is the likelihood probability distribution,  $P(\theta_P | I)$  is the prior distribution for the plasma parameters, and  $P(\{P_r\} | \theta_C, I)$  is the evidence. The likelihood is the same as Eq. 3.12 with a plasma forward model for the annular bin counts  $M_P(r)$  given by

$$M_P(r) = \int d\lambda \text{PSF}(\lambda) \times A \exp \left[ -\frac{1}{2} \left( \frac{\lambda - \lambda_0(1 - V/c)}{\sigma_{T_i}} \right)^2 \right] \quad (3.16)$$

where  $\lambda_0$  is the wavelength of the Ar II line,  $V$  is the toroidal velocity,  $A$  is the amplitude, and  $\sigma_{T_i}$  is the thermal broadening. For now, chord effects are neglected for simplicity of analysis. Future work will incorporate a velocity gradient along the line-of-sight in the forward model and multiple chord measurements will be used to resolve the velocity gradient. The prior range for  $T_i$  is between room temperature and the electron temperature since the only ion heating mechanism is through electron collisions. The prior range for  $V$  is likewise assumed to be subsonic ( $|V| < \sqrt{kT_e/m_i}$ ). The prior range for the amplitude is set at 75% and 200% of the peak counts in the image.

### 3.6 Initial Results

A calibration for measuring Ar II emission was taken using 3 stacked 1 nm full-width half-maximum 488 nm central wavelength filters with an integration time of 3 seconds. The resulting image can be seen in Fig. 3.2 with a log-scale for the counts. Most of the extraneous lines have been reduced to just above the background level as seen in Fig. 3.6. Performing the calibration procedure outlined in Section 3.4 yielded poor results for the wavelength calibration. As a solution, a known third emission line was added to the calibration. The middle nuisance peak in the Fig. 3.6 inset is identified as a singlet from the NIST Atomic Spectra Database [52] using the posterior wavelength calibration with two known lines. The resulting posterior distributions using 3 emission lines for  $f_2$  and  $d$  are shown in Fig. 3.9. All other marginal posterior distributions resemble Gaussian distributions and can be characterized by a mean and standard deviation. The finesse was measured to be  $22.71 \pm 0.04$ . The addition of the third wavelength in the calibration significantly constrains the marginal posterior for the étalon spacing. Any errors in the absolute wavelength calibration result in a systematic offset for the velocity. Refitting the Ar II peak with a velocity shift yields a systematic error of 20 m/s.

Initial data for the Fabry-Pérot spectrometer was taken on the plasma Couette experiment (PCX) [19, 64, 65]. Plasmas were created with a lanthanum hexaboride ( $\text{LaB}_6$ ) emissive cathode [66, 50] placed in the center and biased relative to a grounded molybdenum anode to produce an argon plasma with an electron density of  $4 \times 10^{17} \text{ m}^{-3}$  and electron temperature of 4 eV. Using

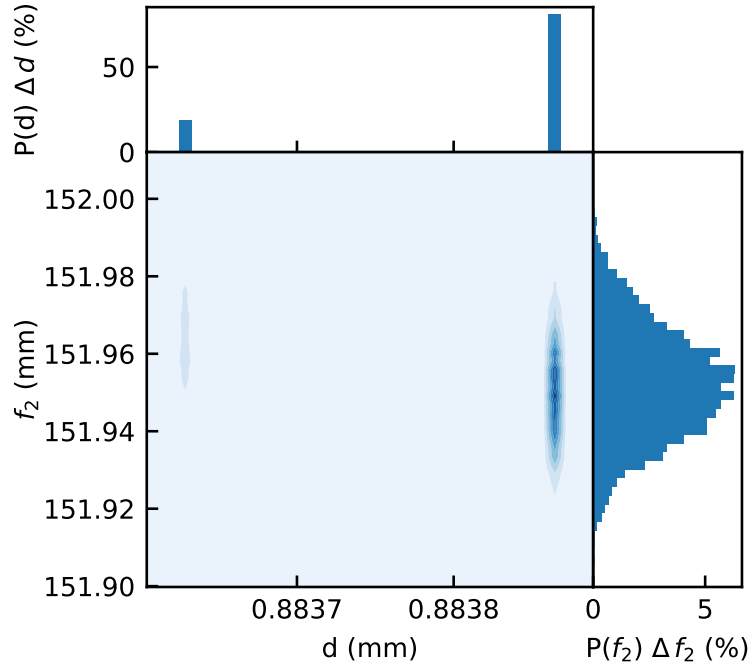


Figure 3.9: Marginal joint posterior probabilities for  $f_2$  and  $d$  from a calibration lamp image using a model with 3 wavelengths each with one order. The probability distributions are better constrained than the synthetic results due to the third wavelength used in the model. The estimated systematic uncertainty in the wavelength calibration can be characterized by a Doppler shift of 20 m/s for the ArII line.

the marginalized calibration posterior for  $f_2$ ,  $d$ , and  $\mathcal{F}$  in the analysis outlined in Section 3.5, preliminary results show an ion temperature of  $0.339 \pm 0.007$  eV and an ion velocity of  $-3 \pm 4$  m/s for a chord very close to the axis of symmetry for the vessel where no flow is expected because of the regularity condition at  $r = 0$ . The marginal joint posterior probabilities for  $T_i$  and  $V$  can be seen in Fig 3.10. Initial results from a volumetric flow drive (VFD) [21] plasma on PCX measured ion velocities of 250 m/s.

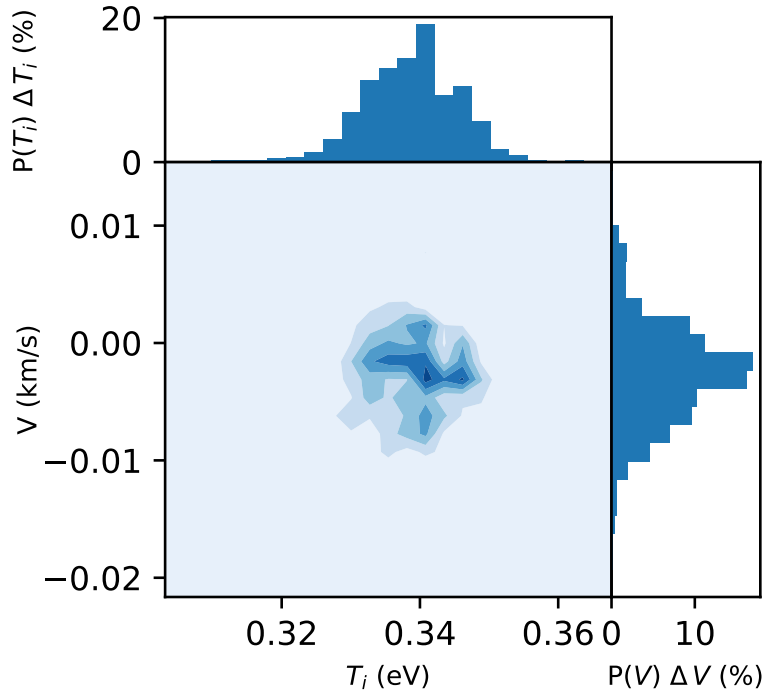


Figure 3.10: Marginal joint posterior probabilities for  $T_i$  and  $V$  from an argon plasma on the PCX experiment. The plasma was generated using a single LaB6 cathode. The spectrometer chord was near the axis of symmetry where the toroidal flow velocity must go to zero. The marginal probabilities resemble Gaussian distributions, and the marginal joint posterior shows very little correlation.

### 3.7 Camera Upgrade

Initial results with the Nikon D5200 digital camera were promising, but there were a few issues that needed to be addressed. The pixels are relatively small at  $4 \mu\text{m}$  requiring integration times greater than a few hundred milliseconds. Although, annular summing greatly increases the signal to noise, we want the tails of the spectrum to be above the dark counts which sets the minimum integration time. In addition, knowing the exact time of exposure is difficult because the delay between the camera recording an image and the trigger is approximately 240 ms. The camera is also limited to 3 frames per second (fps). The goal was to pick a monochrome camera capable of

taking more than 10 images per one second plasma, with minimal delay between the trigger and data acquisition.

At the time of considering an upgrade, the WiPPL lab owned two candidate cameras: the Nikon D5200 and an Andor iStar ICCD. The Andor camera is an intensified CCD that would allow short integration times at very specific times but would only allow for 3 fps. We chose to look at CMOS cameras offered by ThorLabs that allow higher fps and are monochrome. A summary of the 3 cameras can be see in Table 3.1. To determine if the ThorLabs camera would suit our needs, we needed to estimate the integration time. The minimum integration time is set by the number of counts in the wings of the airy function measured by the Fabry-Pérot spectrometer. Assuming the optics is designed such that every ray entering the system is collected at the sensor, the ratio of pixel size to sensor size is the important factor to consider. For the Nikon D5200, the ratio of pixel size to sensor size is  $0.004 \text{ mm} / 15.6 \text{ mm} = 0.026\%$  where for the ThorLabs DCC3260M it is  $0.082\%$ . With only changing the camera and a single lens, we can obtain a 3x reduction in integration time. A sample of a quick linear least squares fit to a stationary plasma is shown in Fig. 3.11 showcasing the new time dynamics that can be measured by the Fabry-Pérot spectrometer.

	Nikon	ThorLabs	Andor iStar
Sensor Type	CMOS	CMOS	CCD
Sensor Dimensions	(6000, 4000)	(1936 x 1216)	(1024, 1024)
Pixel Size ( $\mu\text{m}$ )	4	5.86	13
FPS	3	41	3
Read Noise (e-)	3	7	5
Quantum Efficiency	0.5	0.75	0.5

Table 3.1: Camera comparison table

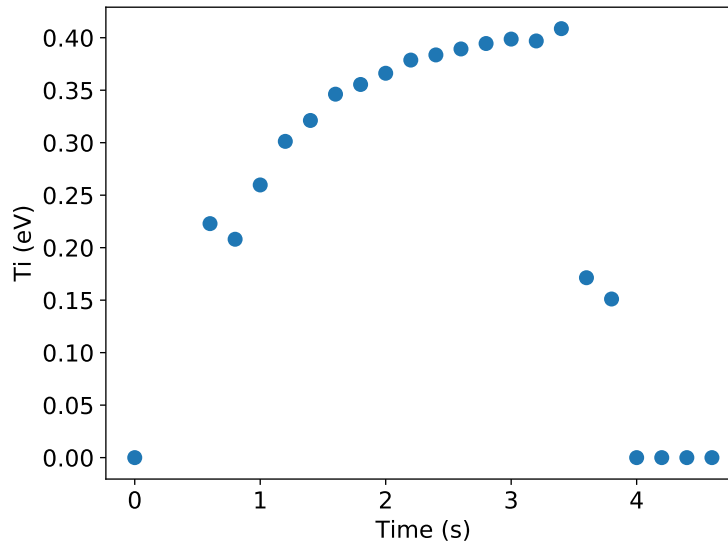


Figure 3.11: Quick  $T_i$  fit for FP to demonstrate time dynamics.

### 3.8 Étalon Temperature Stabilization

The goal of measuring profiles of velocity with the Fabry-Pérot spectrometer requires temperature stabilization of the étalon spacers. Initial calibration measurements showed the zero velocity calibration drifting as much as 1 km/s over the course of a few hours as the temperature in the lab varied. As a result, we decided we needed to implement a proportional-integral-derivative controller (PID) to achieve better stabilization of the calibration over time. For  $1^\circ\text{C}$ , an étalon spacer made of fused quartz would expand 0.5 nm. A 1 km/s velocity shift is equivalent to an expansion of 3 nm for the étalon spacing. Glass is a factor of 10 worse than quartz and Invar is a factor of 2 worse. For 10 m/s stability with a quartz spacer, we need to have  $0.06^\circ\text{C}$  temperature stability. Our design goal was to regulate the étalon temperature to within 0.1 degree C.

We purchased a PID controller from Omega for étalon temperature stabilization. The controller measures the temperature of the étalon housing using a thermistor. The heater consists of two 1 cm x 5 cm strips of flexible polyimide insulated heat tape with a power density of  $5\text{ W/in}^2$ . The PID controller is controlling the temperature by minimizing this function,  $u(t)$  given by

$$u(t) = K_p e(t) + K_i \int_0^t e(\tau) d\tau + K_d \frac{d}{dt} e(t) \quad (3.17)$$

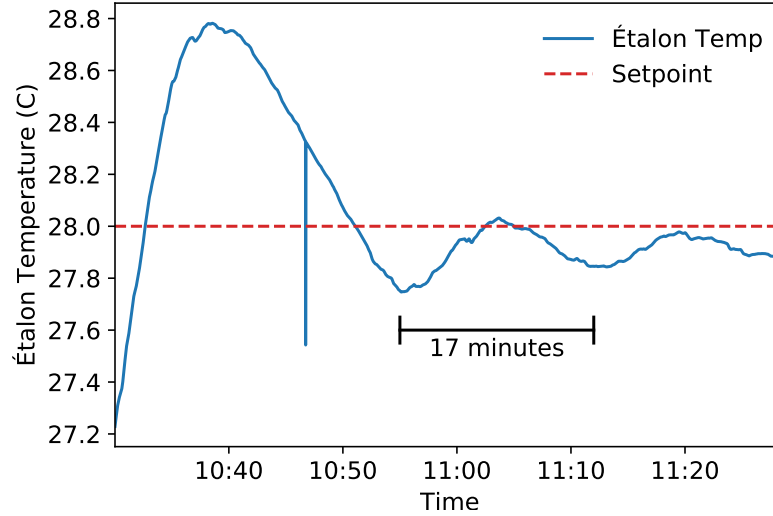


Figure 3.12: Étalon temperature during Ziegler-Nichols PID tuning. At a gain of  $K_p = 90$ , oscillations started with a period of 17 minutes.

where  $e(t)$  is the difference between the temperature and the setpoint,  $K_p$  is the proportional gain,  $K_i$  is the integral gain, and  $K_d$  is the derivative gain. The PID was tuned using a Ziegler-Nichols method [67] which entails increasing the proportional gain with integral and derivative gains set to zero until oscillations begin. The results from increasing the gain until oscillation can be seen in Fig. 3.12. The gain that causes oscillation,  $K_u$ , and the period of oscillation,  $T_u$  are used to calculate the three parameter using these equations:

$$K_p = 0.6K_u \quad (3.18)$$

$$K_i = 1.2K_u/T_u \quad (3.19)$$

$$K_d = 3K_uT_u/40 \quad (3.20)$$

The results from tuning can be seen in Fig. 3.13 where the étalon has been slowly ramped to a specified setpoint.

After temperature stabilization, the étalon zero velocity calibration became more stable, but not stable enough for a plasma scan. The drift of the zero flow calibration can be seen in Fig. 3.14 during a run day. These fluctuations lead me to believe that the spacers are not made of quartz, but

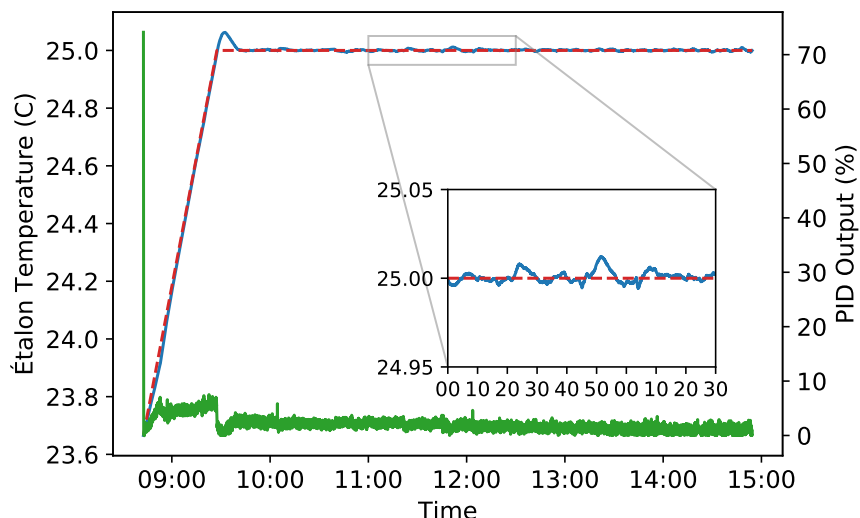


Figure 3.13: Étalon temperature ramping from room temperature to a setpoint of 25 degree C. A linear ramp was used to limit overshoot. According to the controller, the temperature is regulated to better than 0.03 degree C. After reaching the setpoint, the controller can be left on indefinitely.

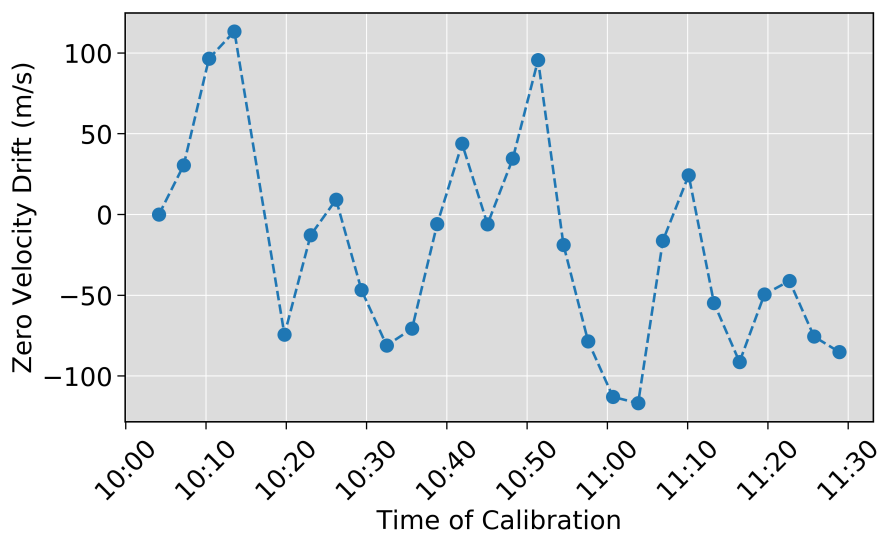


Figure 3.14: Drift of the zero velocity calibration over time taken using setup described in Fig. 3.15.

possibly normal glass which has a thermal expansion coefficient that is 10 times worse than quartz. To counteract this issue, Ken Flanagan designed, ordered, and 3D printed parts for a linear stage

to move a 45 degree mirror in front of the collection optics collimator so calibration images can be taken after every plasma discharge. A CAD drawing of the stage can be see in Fig. 3.15. The new étalon spacing can be determined by using the run day's calibration with an offset velocity compared to a new étalon spacing with zero velocity. This relationship in peak location given by

$$r_{\text{peak}} = f_2 \left[ \left( \frac{2d/(\lambda(1 - v/c))}{m_0} \right)^2 - 1 \right]^{1/2} = f_2 \left[ \left( \frac{2(d + \Delta d)/\lambda}{m_0} \right)^2 - 1 \right]^{1/2} \quad (3.21)$$

where the order  $m_0$  is assumed unchanged,  $v$  is the offset velocity,  $\Delta d$  is the change in étalon spacing,  $r_{\text{peak}}$  is the location of the calibration peak, and  $f_2$  is the camera lens focal length. Solving for  $\Delta d$  yields this relationship with the offset velocity:

$$\Delta d = \frac{dv}{c} \left( 1 + \frac{v}{c} \right) \quad . \quad (3.22)$$

With this relationship, it is now possible to measure flow profiles with the Fabry-Pérot where the limiting factor is the shot to shot reproducibility and not the absolute wavelength calibration.



Figure 3.15: Linear stage for positioning a calibration mirror in front of the collection optics immediately after the plasma discharge. The stage was designed, 3D printed, and assembled by Ken Flanagan.

### 3.9 Summary

A high throughput, high étendue Fabry-Pérot spectrometer has been built for measuring ion temperatures and velocities to high precision. A Bayesian technique for calibration was developed to handle the uncertainty in the absolute order number. To counteract drifts in the wavelength calibration, both étalon temperature stabilization and a linear stage enabling automatic calibrations for every plasma discharge were implemented. As a result, the Fabry-Pérot spectrometer is able to measure ion temperatures and velocities multiple times per shot with unprecedented uncertainties for low temperature argon plasmas.

## Chapter 4

### Volumetric Flow Drive

As discussed in Chapter 1, PCX and the BRB were built to study plasma hydrodynamics and flow-driven instabilities such as the dynamo and the magneto-rotational instability (MRI). Cami Collins had amazing results with spinning plasmas on PCX using cathodes embedded in a cusp magnetic field [19, 18, 64]. With the center stack equipped with small tungsten cathodes, a centrally peaked flow was achieved. Unfortunately, there were a few issues with the flow for exciting the MRI: the cathodes were fragile and prone to breaking, applying a weak magnetic field changed the optimal location for cathode placement for driving flow, and the shape of the flow profile was stable to the MRI because of the momentum diffusion length. As a response to these issues, volumetric flow drive was proposed as a solution to driving the flow globally instead of locally and relying on viscosity to couple momentum. First results on the BRB were promising but needed more diagnostic coverage. This chapter describes the latest experiments with volumetric flow drive on the BRB and PCX.

#### 4.1 Overview of Volumetric Flow Drive

Volumetric flow drive is the process of drawing current across a weak uniform magnetic field applying a body force to the plasma. As a result, the neutrals only play a role as a body force to slow the plasma down and not inhibit the transfer of momentum like in the edge-driven case. With a cylindrical geometry, we naively expect to have the radial current,  $J_r$ , scale like  $\sim 1/r$ . The resulting body force would give rise to a centrally peaked flow similar to Keplerian flow that could be unstable to the MRI ( $k_z V_A < -\partial\Omega^2/\partial \ln r$ ).

The applied magnetic field is considered weak when the plasma  $\beta$ , the ratio of the plasma pressure to the magnetic pressure, is on the order of 1 or higher and the ions are weakly magnetized. When  $\beta > 1$ , the plasma is able to push the magnetic field around. Electrons and ions are considered magnetized when the particle is able to complete many gyro-orbits around a field line without collisions with other particles and the system wall. Summaries of the various frequencies and length scales for typical argon plasmas at WiPPL can be seen in Fig. 4.1. The electrons are almost always magnetized with the cyclotron frequency greater than the collision frequencies with ions and neutrals. The ions remain relatively unmagnetized for fields less than 50 G with the ion-electron collisions being more frequent than ion-neutral collisions.

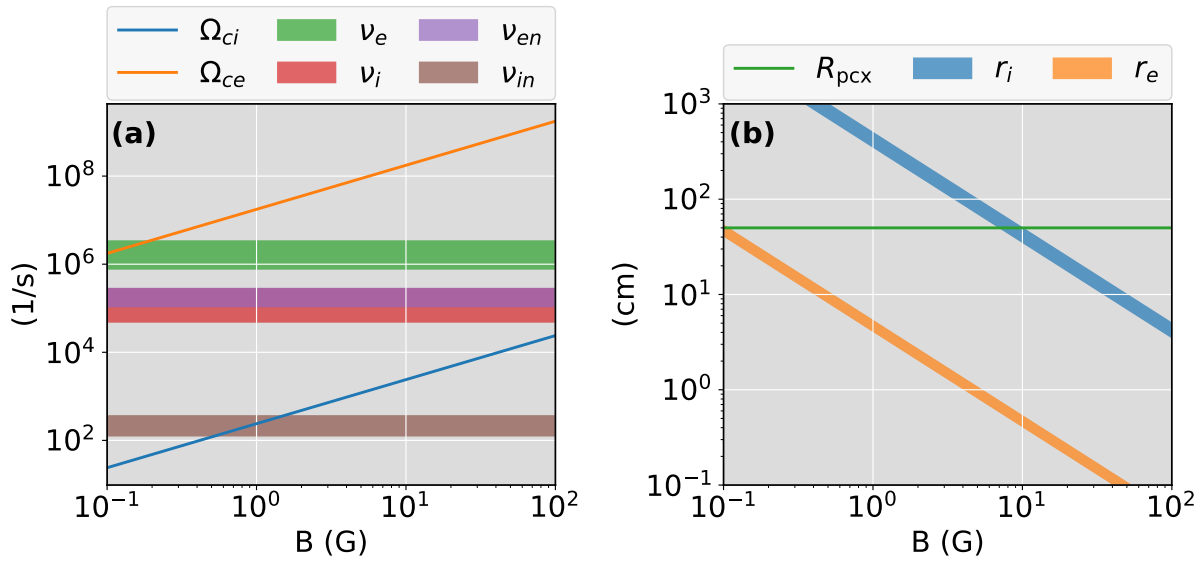


Figure 4.1: (a) Collision frequencies and cyclotron frequencies as a function of magnetic field for typical argon plasmas. (b) Ion and electron Larmor radii as a function of magnetic field compared to the PCX system size for typical argon plasmas. Parameter ranges are:  $T_e \in [3.0, 5.0]$  eV,  $T_i \in [0.3, 0.6]$  eV,  $n_e \in [3, 6] \times 10^{17} \text{ m}^{-3}$ , and  $n_n \in [3, 6] \times 10^{17} \text{ m}^{-3}$

## 4.2 Volumetric Flow Drive on the BRB

For the VFD experiments run on the BRB, the cathode anode configuration was set up to draw current radially outward. The decision to run the experiment with cathodes at the equator was based on the ease of installation and the MRI is more unstable in Hall-magnetohydrodynamics (Hall-MHD) when the angular momentum vector is anti-parallel to the applied magnetic field [4, 3, 18]. The 6 cathodes were located near the equator with two ring anodes at the north and south poles of the device. The cathodes were located at  $-15^\circ$ ,  $-5^\circ$  (x2),  $+5^\circ$  (x2), and  $+15^\circ$ . The ring anodes were designed by John Wallace are shown in Fig. 4.2 and are a stainless steel ring with an inner diameter of 20 cm and an outer diameter of 33 cm. A cartoon depicting the experimental setup is presented in Fig. 4.2.

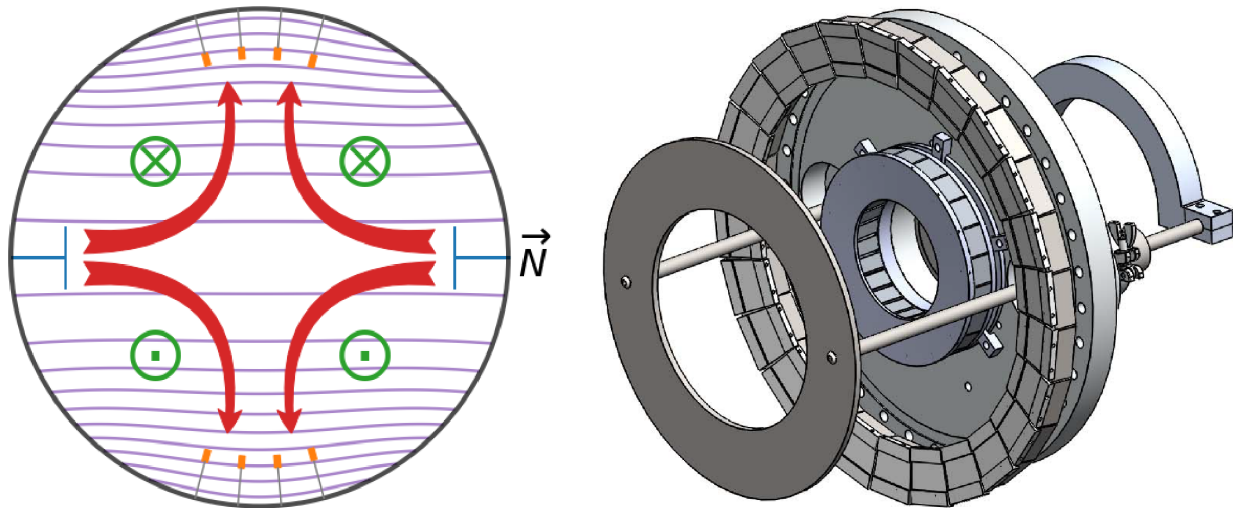


Figure 4.2: Volumetric flow drive setup on the BRB. Cathodes (yellow) are installed near the equator at  $\pm 15^\circ$  and  $\pm 5^\circ$ . There are two stainless steel polar anodes (blue, shown on the right) installed on each hemisphere's pole. A weak uniform axial magnetic field (purple) from the 4 m Helmholtz coil is applied. The cathodes are biased relative to the grounded anodes drawing current (red) across the plasma radially outward. Flow (green) is expected to flow in  $-\hat{\phi}$  direction with respect to the N pole.

The two main diagnostics for the experiment were a linear array of 3-axis Hall probes spaced 3 cm apart for measuring the magnetic field and a Mach-Triple probe for measuring plasma flow, electron temperature, and electron density. Each probe was mounted on a 2D stage capable of scanning in the poloidal plane mapping out a “pie” slice of the plasma. The two stages were located at  $+15^\circ$  and  $+65^\circ$ . A simplified schematic showing the location of cathodes, anodes, and probes is shown in Fig. 4.3. All 3 axes of the magnetic field were measured for the two pie slices. The density, electron temperature, and ion velocities were measured for a cylindrical radius scan at  $z = +40$  cm shown as a vertical magenta line in Fig. 4.3. Four 3-axis Hall probes were mounted on the wall of the BRB near the equator each separated  $90^\circ$  to monitor non-axisymmetric effects.

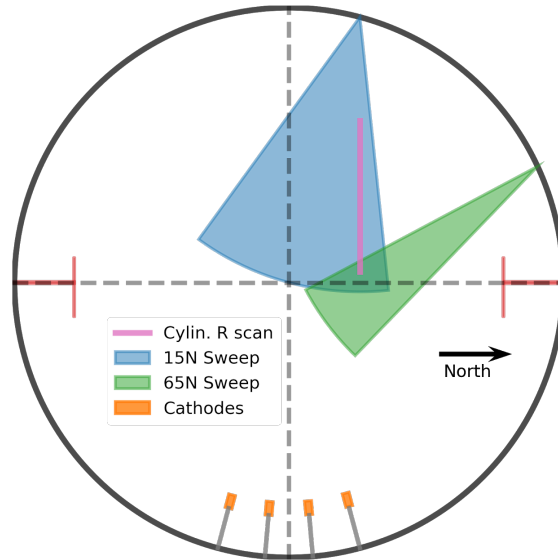


Figure 4.3: Simplified schematic of the BRB showing diagnostic access. Two sweep stages are mounted at  $15^\circ$  and  $65^\circ$ .  $65^\circ$  is limited in travel to avoid the other probe and the Earth’s magnetic field correction coil. Cathodes are inserted near the equator with ring anodes at the poles.

For the BRB experiments, 4 cases of applied magnetic field were carried out: -1.4, -0.9, -0.4, and 0.4 G. The current was limited to approximately 300 A because of the plasma self-extinguishing. It is worth noting that there is a residual magnetic field from the permanent magnets that resembles a large dipole with a field strength of approximately  $\sim 0.4$  G. Time traces of density, electron temperature, magnetic field, and injected current are presented in Fig. 4.4. The

electron density and temperature are measured with a triple probe at  $r = 26$  cm,  $z = 40$  cm. The applied magnetic field is initially small, but almost immediately increases to a large value as the injected current ramps up. It can be seen that north pole anode is preferentially collecting more current over the other. This could be due to an imbalance in the injected cathode current or an asymmetry in the magnetic field that is not captured in the measurements.

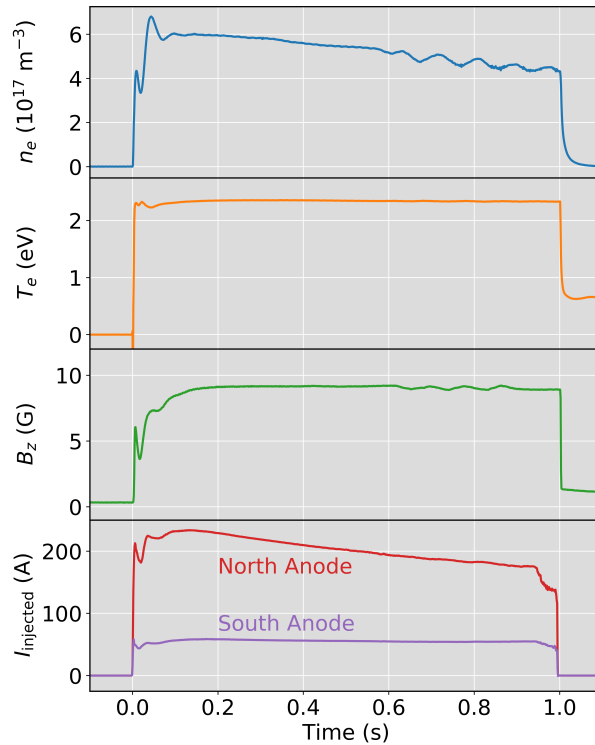


Figure 4.4: Typical time traces for VFD experiments on the BRB. Electron density,  $n_e$ , and electron temperature,  $T_e$  are measured with a triple probe at  $r = 26$  cm,  $z = 40$  cm. The initial magnetic field is  $+0.4$  G pointing toward the north pole of the vessel. The magnetic field increases with the injected current with the north anode preferentially drawing more current.

In all magnetic field cases, a large increase in the magnetic field in the center of the device is observed. Depending on the initial field strength, the increase is between 10-20x the initial field. Examining the initial flux compared to the final plasma flux shows that this final magnetic field cannot be explained solely by compression of the initial field. Measurements of the axial magnetic

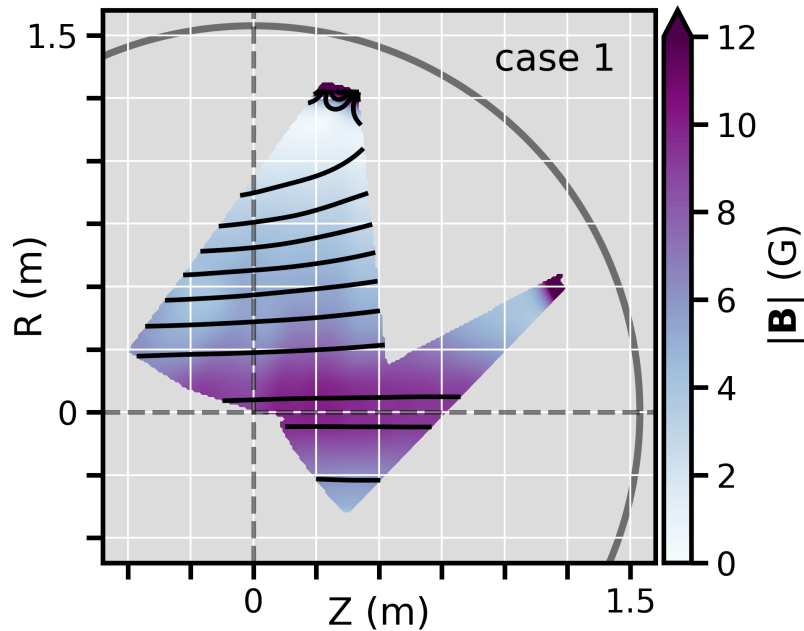


Figure 4.5: Magnetic field measurements for  $B_{z0} = 0.4$  G. Axial field lines are shown in black. The colormap represents the magnitude of the magnetic field. Near the axis, the magnetic field lines are mostly straight. The field is peaked on axis with a value of  $\sim 10$  G yielding approximately  $\sim 20$ x the initial applied magnetic field.

field and flux lines can be seen in Fig. 4.5. The field lines show that the field is mostly straight in the  $z$  direction. A 1D cut shown in Fig. 4.6 shows an approximately  $\sim 10$  G field at the center with a gradient decreasing over a large portion of the plasma. The plasma beta is large ( $> 0.3$ ) throughout the plasma. For the  $+0.4$  G applied field case,  $\beta$  is  $0.4$  near the axis and  $\sim 2$  at  $r = 20$  cm. At the peak flow, the Alfvén velocity,  $V_A$  is as high as  $\sim 1.5$  km/s giving an Alfvén Mach number,  $M_A$ , near  $\sim 0.5$ . In all magnetic field cases, the plasma is in a regime where the plasma pressure and flow are strong enough to modify the magnetic field structure as is clearly shown in Figures 4.4, 4.5, and 4.6.

In addition to the large magnetic field in the center, the plasma density is unexpectedly hollow. The profile of the electron density from the Triple probe can be seen in Fig. 4.6. In hindsight, it should be obvious that if there is a steady-state magnetic field gradient in the plasma, that the

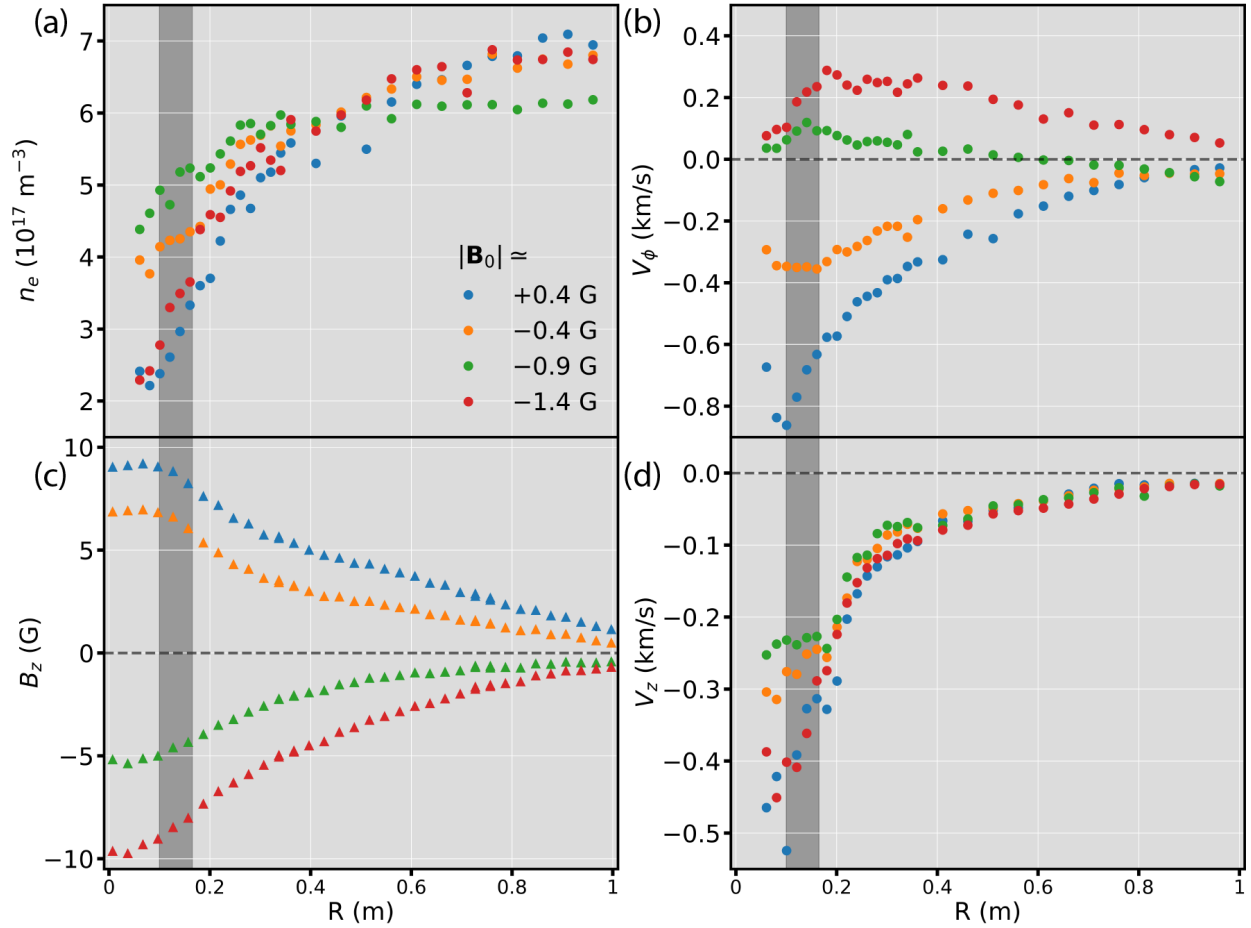


Figure 4.6: Radial profiles at  $z = +40$  cm for 4 cases of applied axial magnetic field of (a) electron density, (b) toroidal velocity, (c) axial field  $B_z$ , and (d) axial flow  $V_z$ .

plasma is in MHD equilibrium and must satisfy  $\vec{J} \times \vec{B} = \nabla P - n_i m_i V_\phi^2 / r$ . Using the assumption that the dominant component is  $B_z$  and the centrifugal term is small, the MHD equilibrium in the radial direction is

$$\frac{dp}{dr} = J_\phi B_z = -\frac{B_z}{\mu_0} \frac{\partial B_z}{\partial r} \quad (4.1)$$

where Ampère's law has been used to replace  $J_\phi$ . Since  $B_z$  and its derivative are always oppositely signed in these plasmas, the pressure gradient is always positive and the plasma density must be lower at the origin compared to the plasma bulk.

The dominant terms contributing to the plasma equilibrium that are neglected in our simple model are two fluid effects including the Hall term and the electron pressure gradient in the generalized Ohm's law. The generalized Ohm's law is given by

$$\vec{E} + \vec{V} \times \vec{B} = \eta \vec{J} + \frac{\vec{J} \times \vec{B}}{ne} - \frac{1}{ne} \nabla p_e \quad (4.2)$$

where  $\vec{V}$  is the single fluid velocity ( $\vec{V} \approx \vec{V}_i$ ),  $\eta$  is the plasma resistivity,  $\vec{J} \times \vec{B}/ne$  is the Hall term, and  $\nabla p_e$  is the electron pressure term. In resistive MHD, the Hall term and the electron pressure term are neglected. The Hall term scales with the ion skin depth ( $d_i = c/\Omega_{pi}$ ) and becomes important at low to moderate densities where the collisionality is low. For relevant plasma parameters on the BRB and PCX, the ion skin depth is on the order of 50 cm and can be larger than the system size. When the Hall term dominates and the plasma resistivity is low, the traditional frozen-in flux condition with the ion fluid is now with the electron fluid. In the case of our experiment, the current direction is radially outward resulting in electrons flowing radially inward dragging the magnetic field inward. In addition, they are drifting in the  $\text{Sign}(B_z)\hat{\phi}$  direction enhancing the applied magnetic field.

In addition to the magnetic field amplification and hollowed out density profile, the plasma is successfully spinning with a centrally peaked profile shown in Fig. 4.6. Even though the ions are not fully magnetized, they should feel a portion of the  $E \times B$  torque causing the plasma to flow. Outside of the core where the magnetic field is largest, the ions are completely unmagnetized and viscosity couples momentum radially outward. For the +0.4 G case, the peak toroidal flow in argon is almost 1 km/s. The flow profile is in a regime that could potentially be unstable to the MRI with decreasing angular velocity and increasing angular momentum with radius, but the magnetic field is too strong. Strong axial flow was measured at a cylindrical radius at  $z = 40$  cm away from the anodes consistent with the ion current direction. The full 2D velocity profile requires further study but is promising for spinning fast flows in a lighter gas species such as helium.

### 4.3 Results on PCX

The next set of experiments with the current direction flipped were run on PCX where it is easier to install a single  $\text{LaB}_6$  cathode at the center and anodes ( $r = 32$  cm) near the edge. For this experiment, the diagnostic suite includes an upgraded linear array of 3-axis Hall probes with 1.5 cm separation, a Mach-Langmuir probe, a Triple-probe, and a Fabry-Pérot spectrometer. A schematic in Fig. 4.7 shows a top-down view displaying the locations of the cathode, anodes, and diagnostics. With the Hall probes, we expect to see the plasma expel the magnetic flux from the core of the plasma, based on the two-fluid effects observed on the BRB and NIMROD [68] simulations presented in Ken Flanagan's thesis work.

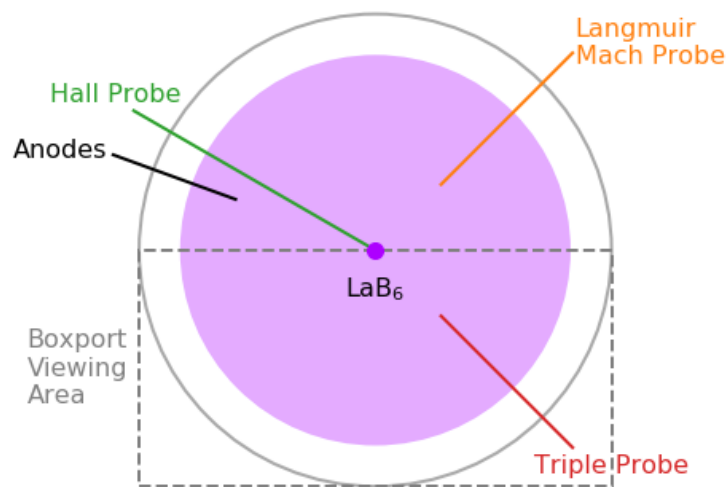


Figure 4.7: Top down view schematic of volumetric flow drive on PCX. A  $\text{LaB}_6$  cathode is installed at  $r = 0$  with 4 anodes at  $r = 32$  cm. A Mach-Langmuir probe is installed at  $45^\circ$  where vertical is  $0^\circ$ . The Triple probe is located at  $135^\circ$ . The linear array of 3-axis Hall probes is located at  $300^\circ$  with a maximum insertion to  $\sim 3$  cm. The box port viewing area allows for optical diagnostics to be scanned across the plasma. The Fabry-Pérot is capable to reaching an impact factor of 3 cm.

For a typical VFD discharge on PCX, the injected current ranges between 50 and 100 A. Within 100 ms, the plasma has expelled most of the flux in the core. Typical time traces of density, electron temperature, cathode voltage, cathode current, and magnetic field for a VFD discharge on PCX is

presented in Fig. 4.8. Unsurprisingly, the amount of flux left in the plasma depends on the injected current with more current removing more flux. The injected current is being deflected into the  $\hat{\phi}$  direction via the Hall effect resulting in a  $J_\phi$  opposing the initial magnetic field.

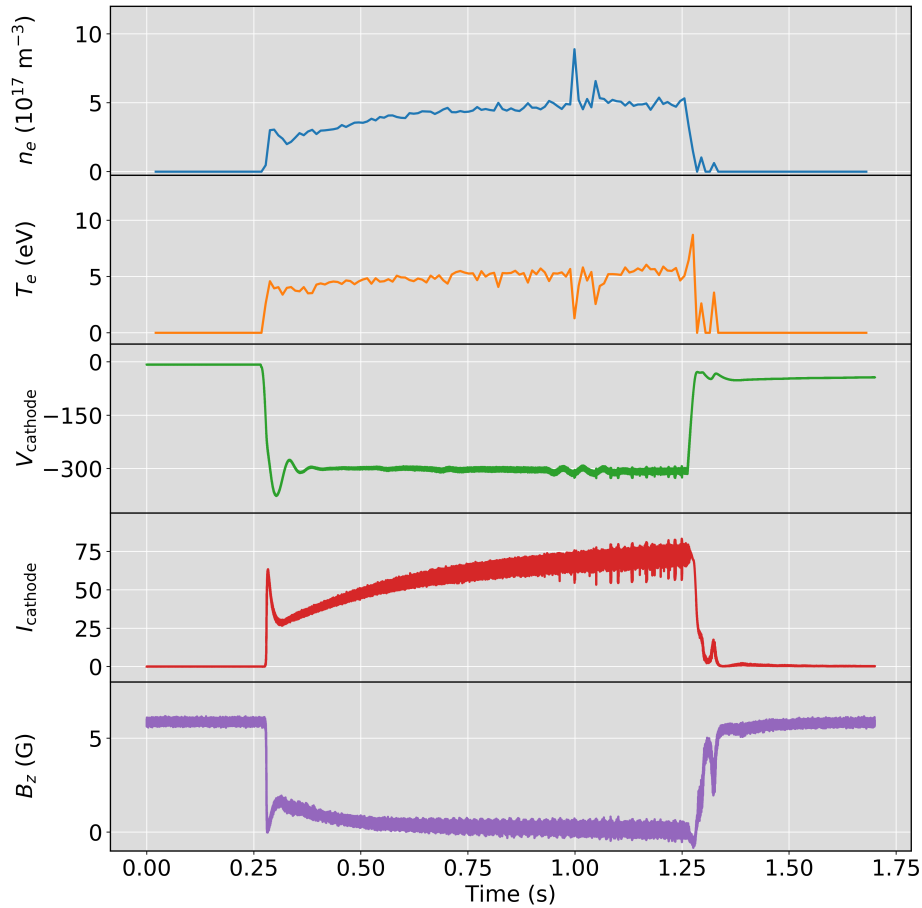


Figure 4.8: Typical time trace from a stable VFD plasma on PCX. Density,  $n_e$ , and electron temperature,  $T_e$ , are measured with a Langmuir probe. The injected current initially rises to a large value removing most of the magnetic flux from the plasma. Afterward, there is a slow ramp in the injected current expelling more of the plasma flux.

Typically, the plasma equilibrium on PCX is similar to the BRB, but that is not the case with volumetric flow drive. For edge-driven plasmas there is a region of localized gradients at the plasma edge and an unmagnetized uniform plasma core. With VFD, the gradient extends much

deeper into the plasma. The equilibrium profiles including the magnetic field and plasma density can be seen in Fig. 4.9 along with a reconstruction of the density profile using the MHD equilibrium. The magnetic field is expelled from the core of the plasma with a large density in the core. The electrons are mostly magnetized with the cyclotron frequency ( $\Omega_{ce}$ ) exceeding the electron-ion collision frequency ( $\nu_e$ ) except at the very center where the field is zero. The plasma  $\beta$  is much larger than one everywhere except at the very edge of the plasma where the magnetic cusp field is strong. Measurements of the floating potential and plasma potential show very little electric field in the plasma. The elongated density profile coupled with the large toroidal current are the biggest differences when comparing to edge-driven plasmas.

The long density gradient extends well past what is considered the edge of PCX plasmas and is unexpected. For VFD plasmas on PCX where the resistivity is low, the extended gradient is a feature of two fluid effects. For ion momentum balance, the only terms are the radial electric field, the centrifugal term, and the ion pressure gradient. The radial ion flow is considered small and is neglected in the analysis. Measurements from the Fabry-Pérot spectrometer discussed later do not see any increased broadening from a radial ion flow. For the electrons, the momentum balance gives

$$E_r = \frac{J_\phi B_z}{ne} - \frac{1}{ne} \nabla p_e = \frac{\nabla p_i}{ne} - \frac{m_i V_\phi^2}{er} \quad (4.3)$$

where the MHD equilibrium has been inserted. The plasma currents and magnetic field balance the total pressure gradient, but the two fluid effects in Ohm's law leave a small electric field to balance the small centrifugal ion flow term and the density gradient to confine the ions radially. The ion flow is small, and the centrifugal term for PCX contributes very little. Measurements of the flow with the Fabry-Pérot spectrometer show solid body rotation with a peak flow of  $\sim 200$  m/s. Details of the flow measurements are found in Section 4.4. On the BRB, the effect is the opposite where the radial electric field draws ions away from the origin. This effect of density piling up or hollowing out based on the current direction was seen in high density plasmas on the COBRA device [12] where the Hall effect can still be important even at large densities.

The large azimuthal current ( $J_\phi$ ) can be explained by examining the toroidal direction of the generalized Ohm's Law (Eq. 4.2) where the only forcing terms are resistivity and the Hall term.

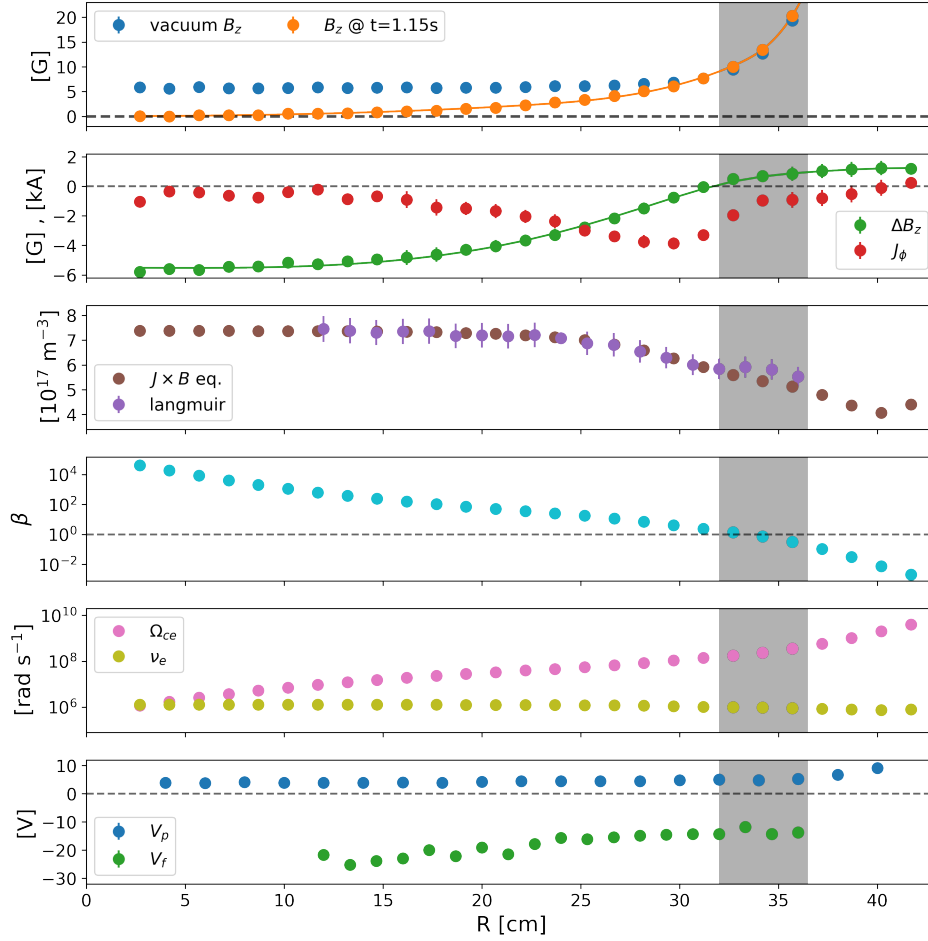


Figure 4.9: Typical equilibrium profiles from VFD experiments on PCX. Initial applied magnetic field is reduced to essentially zero in the plasma bulk with a  $\Delta B_z$  of  $\sim 6$  G, a result from the toroidal current caused by the drifting electrons. The plasma density gradient extends deep into the plasma compared to the typical 3-5 cm for a standard discharge. Plasma  $\beta$  is greater than 1 almost everywhere in the plasma until the very edge where the magnetic cusp field is strong. There is a small radial electric field at large radii which is negligible from 20 cm inward.

The ions are assumed unmagnetized, and the only gradients in the plasma are in the radial direction. The electric field in the toroidal direction is identically zero because there is no steady-state inductive electric field. In equation form, this yields

$$E_\phi \equiv 0 = \eta J_\phi - \frac{J_r B_z}{ne} \Rightarrow J_\phi = \frac{\Omega_{ce}}{\nu_e} J_r \quad (4.4)$$

where Spitzer resistivity has been used to relate resistivity to the electron collision frequency,  $\nu_e$ . For a small injected current,  $J_r$ , a large  $J_\phi$  can develop because the electrons are magnetized with weak fields. In addition, the direction of  $J_\phi$  is determined by the sign of  $J_r B_z$ . On PCX where  $J_r < 0$ , the induced toroidal current will always be in the direction to reduce the magnetic field in the plasma. For the experiment on BRB where  $J_r > 0$ , the induced toroidal current will always be in the direction to increase the magnetic field in the plasma.

#### 4.4 VFD Ion Temperature and Flow Profiles

The Fabry-Pérot spectrometer was installed on PCX to measure flow and ion temperature profiles. For VFD experiments, integration times for sufficient photon counts were between 50 to 200 ms depending on the chord location and density of the plasma. To verify the plasma was flowing with volumetric flow drive, the Fabry-Pérot measured spectra at an impact factor of 21 cm. The chord was treated as a point source to get an estimate of the velocity. The results from different applied fields are presented in Fig. 4.10. Positive velocity indicates flow moving toward the Fabry-Pérot spectrometer. The sign of the velocity flips with the applied magnetic field and matches the  $\mathbf{J} \times \mathbf{B}$  direction. A positive applied field with current radially inward results in flow in the  $+\hat{\phi}$  direction which corresponds to flow away from the spectrometer.

Measuring the ion temperature and velocity radial profiles requires modeling the emissivity along the chord. The emissivity,  $\epsilon$ , from a position in the plasma along the line of sight is given by

$$\epsilon(s) = \frac{c}{4\pi\lambda_0} n_e(r) n_i(r) \langle \sigma v \rangle \exp \left( -\frac{(\lambda - \lambda_0 [1 - V_\phi(r) \cos \theta / c])^2}{\sigma_{T_i}^2(r)} \right) \quad (4.5)$$

where  $V_\phi$  is the toroidal ion velocity,  $\sigma_{T_i}$  is thermal broadening, and  $\theta$  is the angle between the line of sight and the  $\hat{\phi}$  direction. The radiance,  $\mathcal{L}$ , measured by the spectrometer is the line integral of the emissivity along the line of sight. The signal measured by the spectrometer is the radiance convolved with the instrument function. More detail can be found in Chapter 3.

The measured spectra is modeled with a few parameters. The ion temperature is generally presumed to be constant in the plasma bulk. With VFD, there is large density gradient and higher magnetic fields. With this in mind, we have chosen a simple linear profile that allows a nonzero

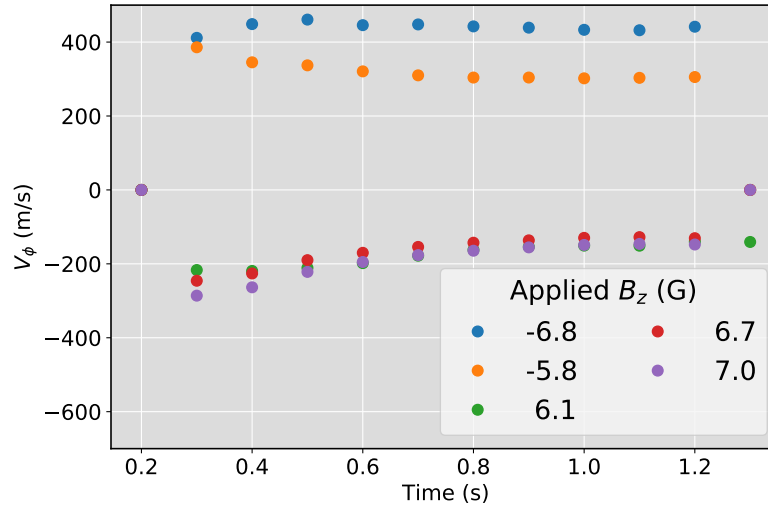


Figure 4.10: Time trace of velocity from the Fabry-Pérot spectrometer for different applied magnetic fields. Flow flips direction with the magnetic field direction. Positive velocity corresponds to flow toward the spectrometer.

temperature gradient in the plasma. The proposed ion temperature model can be seen in Fig. 4.11(a). The model is defined with a central temperature and an edge temperature with no constraints other than temperatures must be positive and a maximum allowed temperature ( $\sim 3$  eV). If the posterior probability is hindered by the upper bound, the solver can be rerun with a higher upper bound.

The ion velocity is presumed to be strictly in the toroidal direction. This ad hoc assumption is revisited later. Measurements from Mach probes and preliminary results from the Fabry-Pérot suggest simple solid body rotation. An offset velocity has been included to account for small misalignment of the collimator and systematic error in the absolute wavelength calibration. The toroidal velocity model can be seen in Fig. 4.11(b). The model is defined with an offset velocity and a peak velocity at the anode location. The velocity profile is kept flat, even if nonphysical, beyond the anodes because the Fabry-Pérot is less sensitive in that region where the density is low.

The profiles of  $T_i$  and  $V_\phi$  are found by measuring multiple chords at different impact factors and running them through our Bayesian analysis. Each image has an amplitude and uses the global  $T_i$  and  $V_\phi$  profiles that have been discussed. The density profile from probe measurements is used

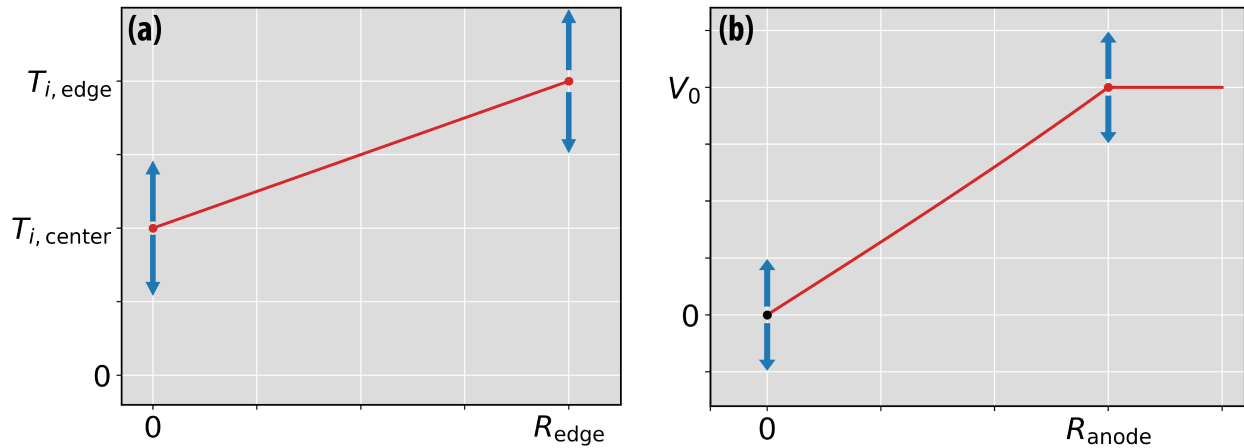


Figure 4.11: Ion model for Fabry-Pérot. (a) Linear  $T_i$  profile that allows the center to be colder or hotter than the edge temperature. If the temperature is indeed flat, the two temperatures will not be statistically different from each other. (b) Solid body  $V_\phi$  profile until the anode location. Profile is flat afterwards where the Fabry-Pérot is less sensitive due to a lack of light. The center allows an offset velocity to account for systematic uncertainties such as misalignment of the collimator and wavelength calibration error.

to model the emission along a chord, but is not used to determine the amplitude for a given image. The procedure is the same as described in Chapter 3. The likelihood for a radii in a given image is the Normal distribution with a mean and standard deviation derived from annular summing. The prior is once again mostly non-informative. We use PyMultiNest to sample efficiently from the prior to calculate the posterior probability and the evidence.

For  $n$  images, the prior consists of  $n+4$  independent prior probabilities for each parameter. The amplitude priors are truncated Normal distributions with zero probability for amplitudes less than zero. The two temperature parameters are Uniform distributions from room temperature 0.025 eV to 3 eV. The offset velocity has a Uniform prior from  $-500$  to  $+500$  m/s. The peak flow velocity has a Uniform prior from  $-5$  to  $+5$  km/s to include velocities up to the sound speed for a hot Ar plasma. If the posterior looks influenced by any of the prior variables, it is widened until it is no longer affected. For computation speed, the prior volume can be reduced as long as the posterior distribution remains unaffected.

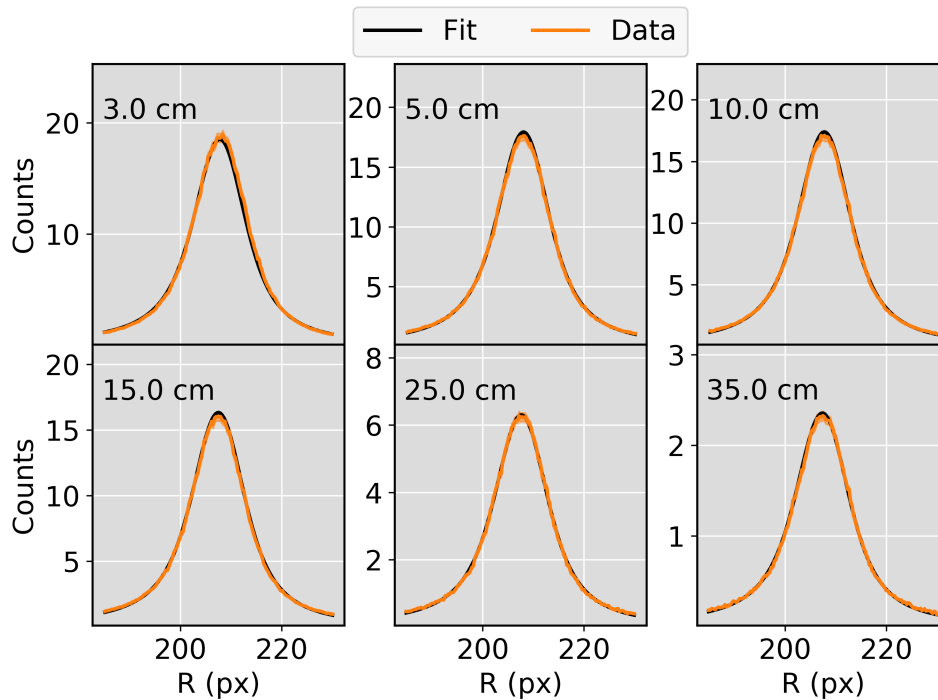


Figure 4.12: Fabry-Pérot measurements and fits for the 6 chords.

For the VFD experiment, 6 chords were used to calculate the posterior for the ion temperature and flow profiles. The chords were located at 3, 5, 10, 15, 25, and 35 cm. The peak location ( $r_{\text{anode}}$ ) was at  $r=32$  cm. Unfortunately, the Fabry-Pérot is unable to reach  $r=0$  due to physical constraints. In future work, the angle with respect to the machine could be changed to allow passing through the origin. Each image has its own calibration taken within 5 seconds of the plasma discharge to ensure an accurate velocity calibration. The fill pressure was  $1.3 \times 10^{-5}$  Torr. The bias voltage was 300 V and the applied magnetic field was 5.7 G. The fits for the 6 chords are presented in Fig. 4.12 and show great agreement with the data. Each fit shown is the mean of models generated by sampling from the posterior distribution.

The full posterior probability resembles a multivariate Normal distribution with each individual marginal probability resembling a Normal distribution. Examining the 2D joint marginal distribution for two of the parameters yields one of two cases: circular contours (no correlation) or tilted elliptical contours (linearly correlated). In this posterior, there were no unexpected correlations

in the posterior. The amplitudes show correlation with the temperature because increasing the amplitude also increases the tails of the distribution and resembles temperature broadening.

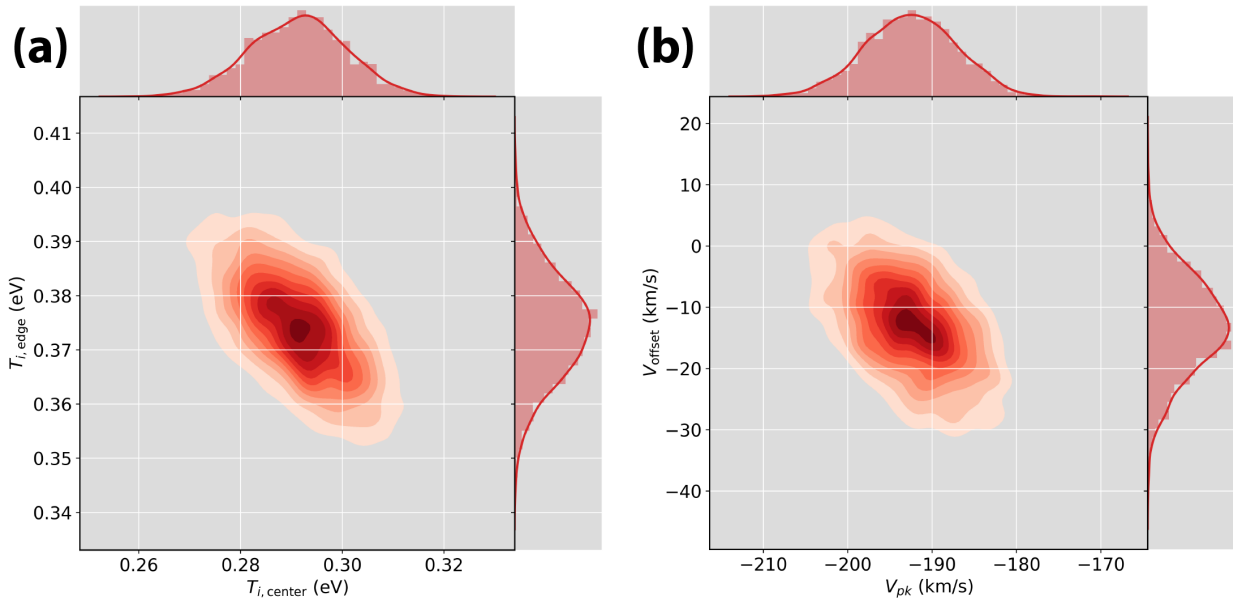


Figure 4.13: (a) Joint marginal posterior probability for the edge and center  $T_i$  values. The individual marginal probabilities do not overlap indicating the assumed linear profile is statistically significant. (b) Joint marginal posterior probability for the peak toroidal velocity and the offset velocity at  $r = 0$ . The mean of the offset is close to zero but is not included within one standard deviation.

The joint marginal posterior for the two ion temperatures shows the center of the plasma is colder than the edge. The 2D posterior can be seen in Fig. 4.13(a). There is a correlation between the two variables because of the parameterization. If the center is hotter, the edge can be colder to achieve the same broadening for inner chord measurements. The two marginal posteriors resemble Normal distributions with slight deformities that might go away with more sampling points in the solver. The  $T_i$  profile is interpreted to be statistically significant because the marginal posteriors do not overlap.

The joint marginal posterior for the two velocities is presented in Fig. 4.13(b). The peak toroidal velocity is  $\sim 190$  m/s. The negative sign means the flow is away from the Fabry-Pérot ( $+\hat{\phi}$

direction). The measured offset velocity is  $\sim 12$  m/s with zero not included in one standard deviation. The offset velocity is an estimate of the systematic errors in the diagnostic including chord position / alignment and absolute wavelength calibration. In the model, the velocity is assumed to be completely in the toroidal direction. If there was radial flow, our Doppler shift would need a  $V_r \sin(\theta)/c$  correction. Because  $\sin$  is an odd function, radial velocity would look like temperature broadening. The broadening would be most pronounced at chords near the origin where the chord is close to being radially aligned. Figure 4.13(a) shows the inner temperature to be colder than the edge temperature indicating any radial flow must be too small to measure with this spectrometer.

The profiles of  $T_i$  and  $V_\phi$  from the Bayesian solver are presented in Fig. 4.14. The confidence intervals are created by sampling from the posterior distribution using them to compute the radial profiles from the model.  $T_i$  shows the temperature increasing radially outward. The ions are unmagnetized and transport should be fast enough to remove any temperature gradients. The velocity profile has a peak flow near 200 m/s with a small offset velocity at the origin as previously discussed. The ions flow fastest where they are partially magnetized near the anodes with viscosity coupling the momentum inward.

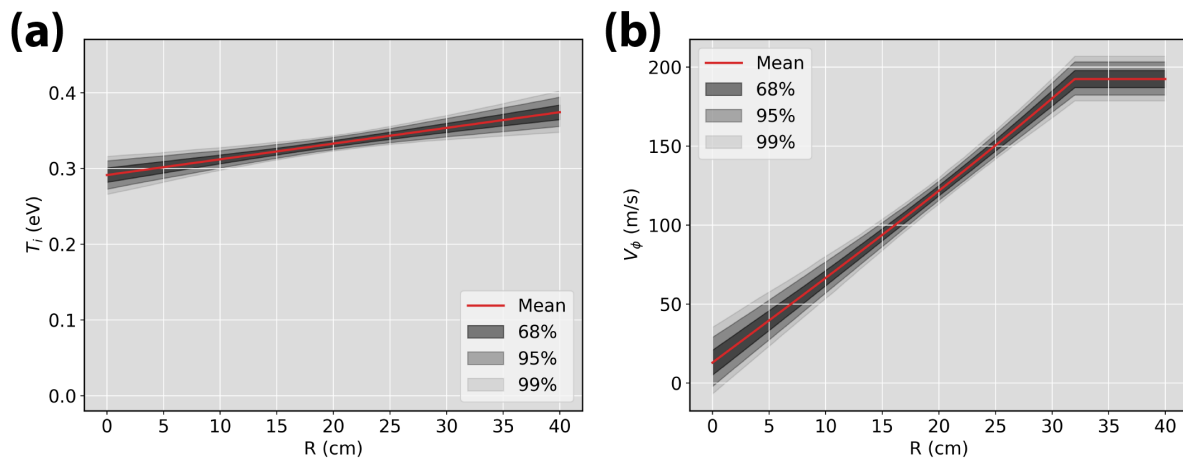


Figure 4.14: (a)  $T_i$  profile from the Bayesian solver. Black levels show 68%, 95%, and 99% confidence intervals for the radial profile. (b)  $V_\phi$  profile from the Bayesian solver.

The Fabry-Pérot takes many images over the course of the plasma discharge. The beginning of the discharge has a lot of variability and is not used for the Bayesian profile solver. The results for the inner and edge  $T_i$  and peak  $V_\phi$  are displayed in Fig. 4.15. The inner  $T_i$  is initially lower but equilibrates with the outer temperature over the course of the discharge. The transport physics remains poorly understood because the ions are mostly unmagnetized and should be mobile. However, the results shown here seem to be consistent with previous non VFD plasmas with a cathode on axis. In those plasmas, an increase in the ion temperature is observed and could be the result of collisional heating from the fast electron population in the magnetic cusp. The increase in the inner ion temperature is consistent with the increase in plasma density and collisionality over the course of the plasma discharge. The flow is initially at its highest speed when the density is lower. As the density rises in time, the flow slows down to  $\sim 150$  m/s. The initial peak flow is most likely the result of a lower density plasma spinning fast during the initial current increase. After the first 100 ms of plasma, the current drastically reduces and slowly ramps up over the remaining portion of the discharge. As the density increases, the peak velocity decreases due to momentum diffusion and charge-exchange collisions. Late in the discharge, the ions are able to flow slightly faster as the drive increases with the injected current.

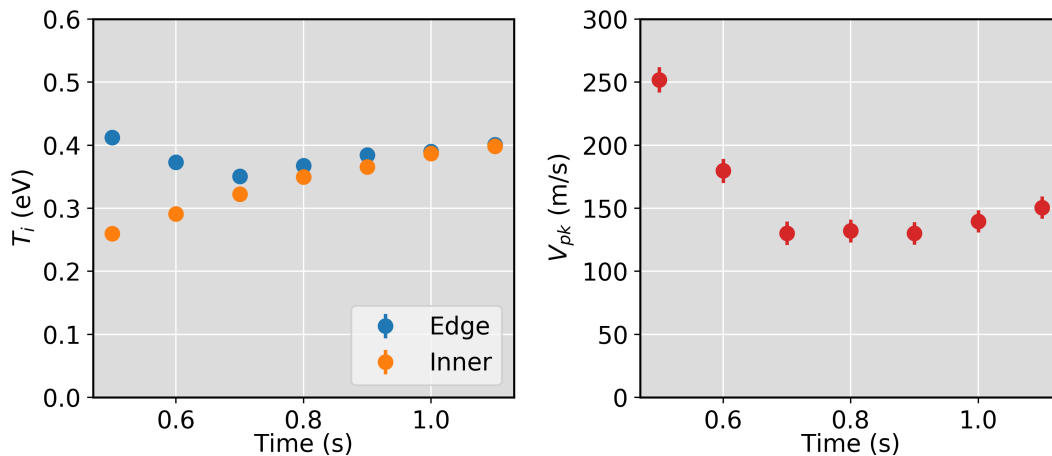


Figure 4.15: Time trace of  $T_i$  and  $V_{pk}$  using Bayesian solver for each time point.

## 4.5 Summary

A high- $\beta$  Hall plasma equilibrium has been described on the BRB and PCX with opposite direction currents for the two experiments. With radially outward current, the electrons carry most of the current and drag the magnetic field lines inward. In addition, the Hall electric field deflects electrons into the toroidal direction creating a toroidal current much larger than the injected current. The resulting magnetic field at the center is much greater than the initial applied field. The centrally peaked flow is promising for exciting the MRI, but the increased magnetic field on axis is stabilizing to the MRI. On PCX with radially inward current, the electrons travel radially outward and are deflected in the toroidal direction to remove flux from the plasma.

The increased magnetic field on the BRB is fascinating because of the similarities it shares with the homopolar disk dynamo. The initial magnetic field plays the role of a fixed field threading the conducting disk in the dynamo. The radially injected current will either reinforce the applied field if the electrons are deflected in the correct toroidal direction. For the case of BRB, the electrons move radially inward and drift to reinforce the magnetic field. In contrast, on PCX, the electrons move radially outward and drift in the opposite direction toroidally to expel the applied magnetic field similar to the homopolar dynamo where the growth rate only occurs if the disk is spinning in the right direction. The analogy breaks down because the system is driven but is still useful to think about how the Hall electric field can generate currents that can reinforce or destroy magnetic field.

In both cases, volumetric flow drive produced flows measured with either with Mach probes or a Fabry-Pérot spectrometer. The Fabry-Pérot flow and temperature results are an absolute achievement in precision and time-scale for low-temperature plasmas. For the BRB, volumetric flow drive is a triumph in creating a high-Alfvén Mach number flow ( $M_A \sim 0.5$ ) that is centrally peaked with lots of flow shear. On PCX, the flow is small but does increase with the strength of the applied magnetic field. In both cases, the ions are flowing where the magnetic field is large enough to partially magnetize them resulting in a local torque. The momentum diffuses away from the driving

location to the rest of the plasma resulting in qausi-Keplerian flows for the BRB case and solid body flows for the PCX case.

## Chapter 5

### Electromagnetic Gradient Drift Instability

The goal of volumetric flow drive on PCX was to drive fast flowing ions for the purpose of studying flow-driven plasma instabilities. Experiments on PCX shown in the Chapter 4 show the development of solid-body rotation at slow speeds for moderate applied magnetic fields. We chose to keep increasing the applied magnetic field in hopes to achieve a faster flow. For a fixed cathode voltage and neutral pressure, increasing the magnetic field increased the injected current substantially and saw some improvement in the max flow speed. However, once the applied field passed some threshold, large coherent fluctuations appeared on every measureable quantity except for the applied voltage as shown in Fig. 5.1.

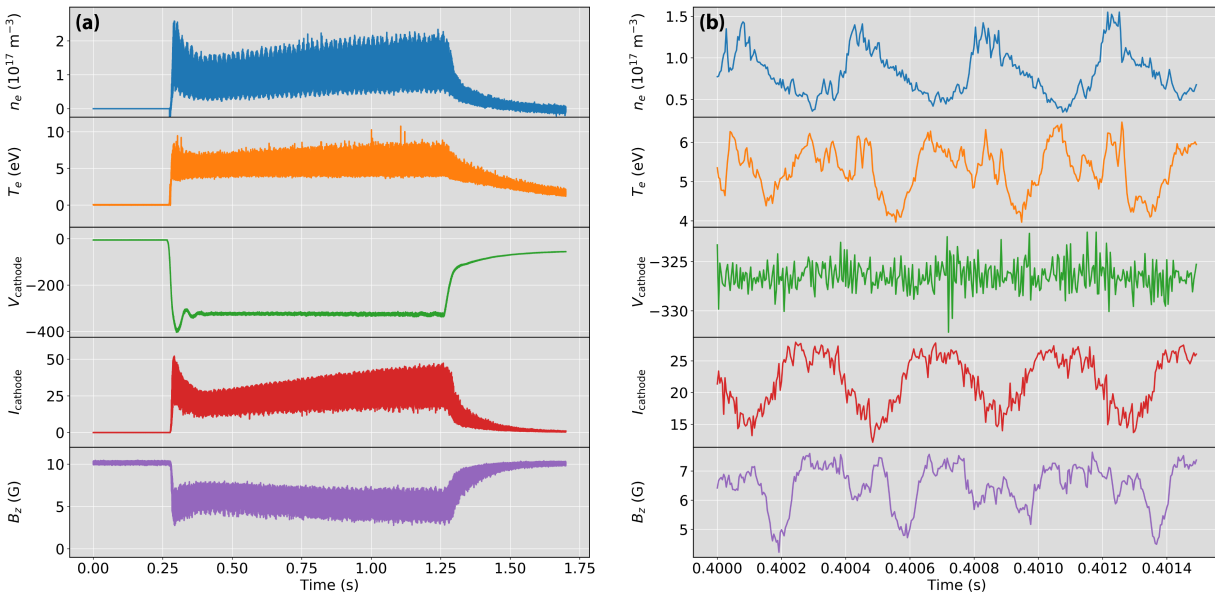


Figure 5.1: Fluctuations on PCX. (a) Time trace from a typical unstable plasma on PCX. (b) Zoomed in view of the fluctuations showing large coherent fluctuations on every signal except for the applied voltage.

## 5.1 Fluctuation onset on PCX

The stability of the plasma is dependent on the strength of the magnetic field. The stable plasmas presented in Chapter 4 show almost complete expulsion of the applied magnetic field. For a fixed neutral pressure and cathode voltage, increasing the applied field leads to an instability. Figure 5.2 shows almost complete flux expulsion for the stable cases with very little removed flux as the magnitude of the applied field increases for the unstable cases. The marginal stability case is when the initial injected current is small with very little flux expelled and the plasma becomes unstable. As time progresses during the discharge, the injected current increases with more flux expelled and the plasma becomes stable. The stability threshold is near  $B_z \sim 1.5$  G for this particular neutral fill pressure and cathode bias voltage.

The flux expulsion is dependent on the strength of the injected current. The stability threshold was probed again by keeping the magnetic field fixed at one of two cases (6.75 and 7.3 G). For

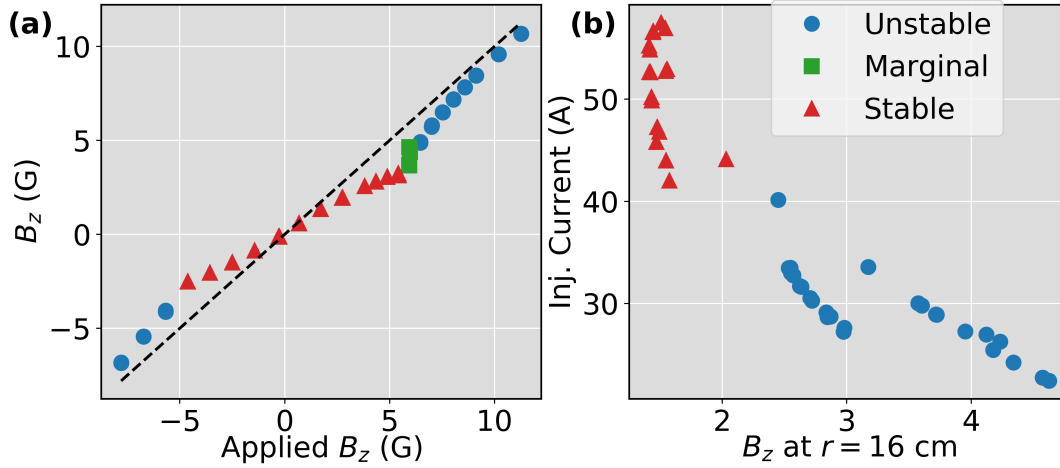


Figure 5.2: (a) Mean  $B_z$  at  $t = 1$  s vs  $B_0$  for a fixed neutral pressure ( $n_n = 2.5 \times 10^{17} \text{ m}^{-3}$ ) and cathode bias voltage (300 V). Deviation from unity line (black dashed) shows flux expulsion from the core of the plasma. (b) Mean injected current  $I$  vs mean  $B_z$  for two different applied magnetic fields (6.75 and 7.3 G) with fixed neutral pressure ( $n_n = 2.5 \times 10^{17} \text{ m}^{-3}$ ). Injected current is varied by varying the applied cathode voltage.

each case, the neutral pressure was held constant and the cathode bias was varied to control the injected current. The results of the scan are presented in Fig. 5.2. For large injected currents, most of the flux is removed and the plasma is stable. For low cathode voltages, little flux is expelled from the plasma and is unstable. The stability threshold is again around  $\sim 1.5$  G again for plasma parameters similar to the previous scan. The dependency on the magnetic field strength in the plasma is probably related to the plasma  $\beta$  and is discussed in more detail in Section 5.4.

## 5.2 Mode structure

The fluctuations measured on PCX have a frequency of 2 – 3 kHz, which lies between the ion cyclotron frequency,  $\Omega_{ci}$ , and the electron cyclotron frequency,  $\Omega_{ce}$ . Figure 5.1 shows fluctuations on  $B_z$ ,  $I_{\text{cathode}}$ ,  $T_e$ , and  $n_e$ . The magnetic fluctuations are predominately in  $B_z$  with fluctuations in  $r$  and  $\phi$  being too small to measure ( $< 0.1$  G). The magnetic flux decreases drastically from

the initial applied field exactly like the stable plasmas in Chapter 4, but is not quiescent. The temperature measurements from the triple probe are suspect because the electrons are probably non-Maxwellian. The voltage measurement on the cathode shows no fluctuations meaning that the fluctuations are from the plasma and not the power supply. Not shown is the density measurement from the second electrostatic probe that is out of phase with the shown time trace indicating non-axisymmetric fluctuations ( $m \neq 0$ ).

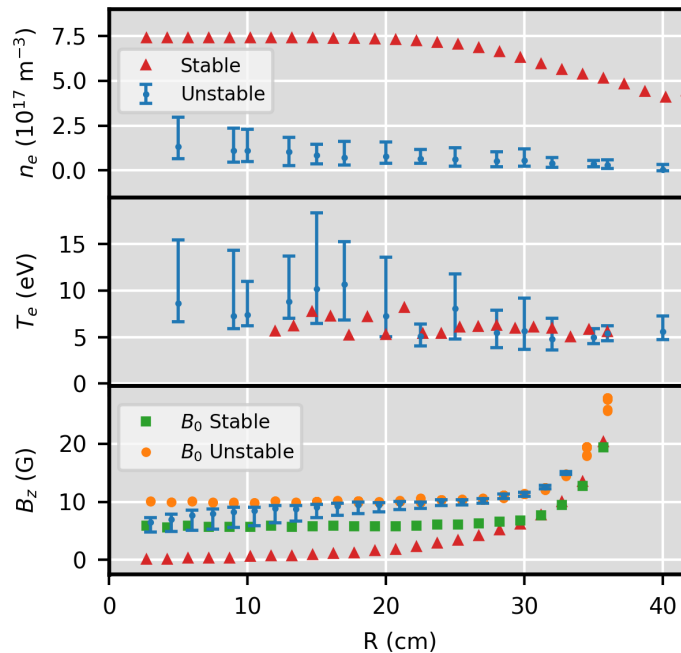


Figure 5.3: Profiles of  $n_e$ ,  $T_e$ ,  $B_z$ , and the vacuum  $B_0$ . Error bars indicate the median of the fluctuations with the upper and lower limits indicating the extrema of the fluctuations.

The power spectral density for  $B_z$ ,  $I_{\text{sat}}$ , and  $T_e$  is presented in Fig. 5.4. Every fluctuating signal has matching peaks in the power spectral density. There is a dominant peak in the 2 – 3 kHz range with a few additional harmonics. The strength of the harmonics depends on the magnetic field in the plasma. For large initial magnetic fields, the harmonics are greatly reduced and the fluctuations are much closer to being a pure single mode.

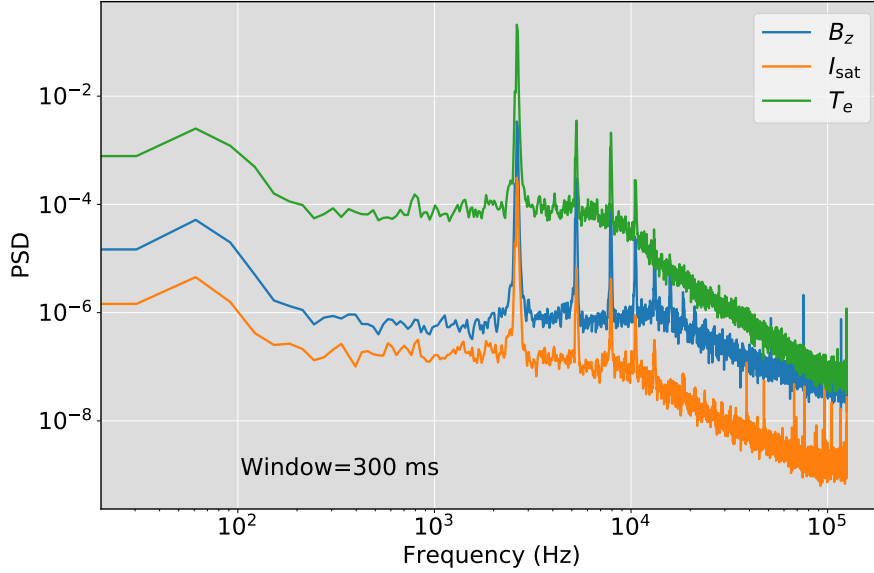


Figure 5.4: Power spectral density for  $B_z$ ,  $I_{\text{sat}}$ , and  $T_e$  signals in fluctuating plasmas.

The fluctuations were recorded with a high-speed camera mounted on the mid-plane of PCX equipped with a fish-eye camera lens. Three image stills from the video recorded at 27 kHz are shown in Fig. 5.5. The light dominated by neutral emission shows a dense column of plasma rotating around the central axis of PCX indicating a predominately flute-like  $m=1$  mode. Measurements of the rotation period match the measured fluctuation frequencies from the magnetic and Langmuir probes.

The main analysis tool for examining time traces from different sources is the normalized cross-correlation. The cross-correlation gives a measure of how similar two time traces are. The discrete form for the normalized cross-correlation for two signals,  $f$  and  $g$  of length  $N$  with lag  $j$  is

$$(f \star g)(j) = \frac{1}{N} \frac{\sum_{i=1}^N (f[i+j] - \bar{f})(g[i] - \bar{g})}{\sqrt{\text{Var}(f)\text{Var}(g)}} \quad (5.1)$$

where  $\bar{f}$  is the mean of  $f$ , and  $\text{Var}(f)$  is the variance of  $f$ . The normalized auto-correlation ( $f = g$ ) gives a measure of the coherence time of a fluctuation.

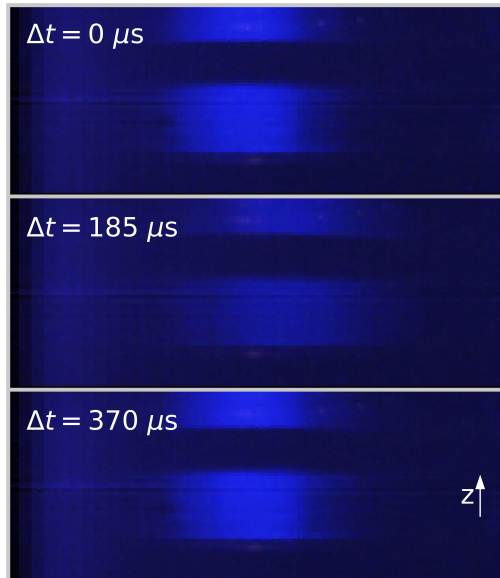


Figure 5.5: Three image stills from phantom camera recorded at 27 kHz with  $36 \mu s$  exposure. Mach-Langmuir probe is visible on the left side. Column of plasma rotates about the central axis of PCX.

Figure 5.6 presents the cross-correlation between  $B_z$  and the  $I_{\text{sat}}$  measurements as well as the auto-correlation of  $B_z$  for approximately 3 periods. The auto-correlation of  $B_z$  shows a coherence time much longer than a single period and actually extends to the end of the plasma duration indicating a very long lived coherent state rotating around the central axis of PCX. Accounting for the toroidal position of each probe, the cross-correlations show that  $B_z$  is mostly out of phase with  $I_{\text{sat}}$  within probe location error. With  $\beta > 1$ , it is expected that large density fluctuations would expel the magnetic field with local diamagnetic currents.

Ion saturation current fluctuations are measured by two electrostatic probes separated by  $45^\circ$  toroidally and 18.5 cm vertically. For a positive applied magnetic field, the mode rotates in the anti-clockwise direction when viewed from above. In Fig. 5.6,  $B_z$  and probe 1 are time shifted

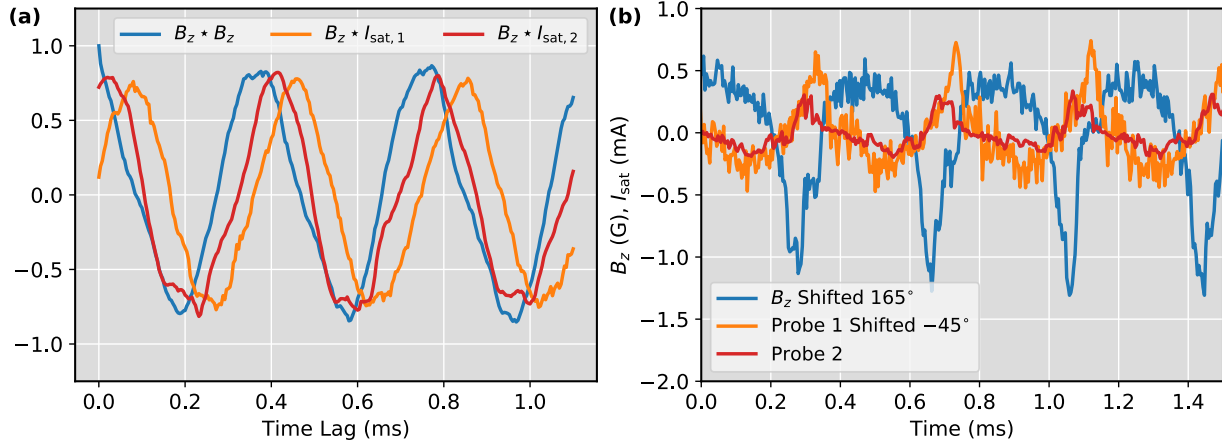


Figure 5.6: (a) Auto-correlation of  $B_z$  and cross-correlations for  $B_z$  with  $I_{sat}$  from two electrostatic probes. (b) Time traces of  $B_z$  and  $I_{sat}$  with toroidal shift correction.  $B_z$  is almost completely out of phase with density fluctuations.  $I_{sat}$  from the two probes show good agreement with each other.

to probe 2's location using  $\Delta t = \Delta\phi/(2\pi f)$  where  $\Delta\phi$  is the toroidal separation in radians. The probes match reasonably well and show good agreement with a  $m=1$  flute mode with  $k_z \sim 0$  when the toroidal shift is accounted for. With the toroidal separation accounted for, the magnetic fluctuations are almost out of phase with the density fluctuations. Errors with radial probe locations are not accounted for here.

Figure 5.7 presents a 2D reconstruction of the mode structure. The Langmuir probe was scanned radially across the plasma volume with the hall array fixed. Each time trace was filtered at the mode frequency determined by the fast Fourier transform of  $B_z$  and synced by maximizing the cross-correlation in  $\delta B_z$ . The mode structure is recovered by mapping time to the toroidal direction ( $2\pi ft \rightarrow \phi$ ). The full signal is used for the mapping, but it is worth noting that the dominant mode is chosen to be  $m=1$  with the toroidal mapping. The mode shown in Fig. 5.7 includes the toroidal shift between the Hall probe array and Probe 2. The peak density of the mode has a much steeper gradient compared to the stable equilibrium and is out of phase with the magnetic field where most of the magnetic flux expelled.

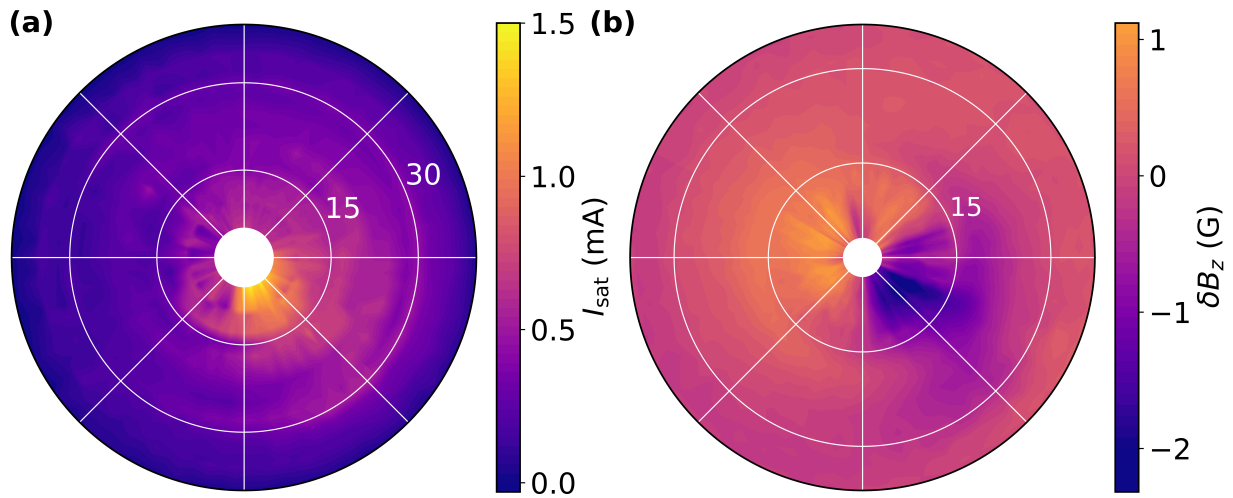


Figure 5.7: (a) 2D structure of the ion saturation current,  $I_{\text{sat}}$ . Blob of increased density at  $-45^\circ$  rotates around the central axis counter-clockwise. (b) 2D structure of the magnetic fluctuation,  $\delta B_z$ . At the location of the blob, the magnetic field decreases significantly. The perturbation rotates with the density blob.

### 5.3 Ion heating and flow

The Fabry-Pérot spectrometer was used to measure the ion temperature and velocity profiles for the unstable plasmas. The Bayesian model is exactly the same as used in Chapter 4 except that no offset velocity was included. This model is a first attempt to model the dynamics in the plasma and does not account for the fluctuations in  $n$  or  $V$ .

Figure 5.8 shows the profiles from the Bayesian solver. The confidence interval for  $V_\phi$  is constrained to be zero at the origin in the model. The most surprising element is the large temperature increase from the core to the edge of the plasma and is discussed in more detail later. The ions are unmagnetized and radial transport should be extremely fast to squash any temperature gradients. The marginal posterior is shown in Fig. 5.9. The joint marginal posterior of  $T_i$  shows clear separation between the inner  $T_i$  and the outer  $T_i$  pointing to a broadening mechanism that is radially dependent.

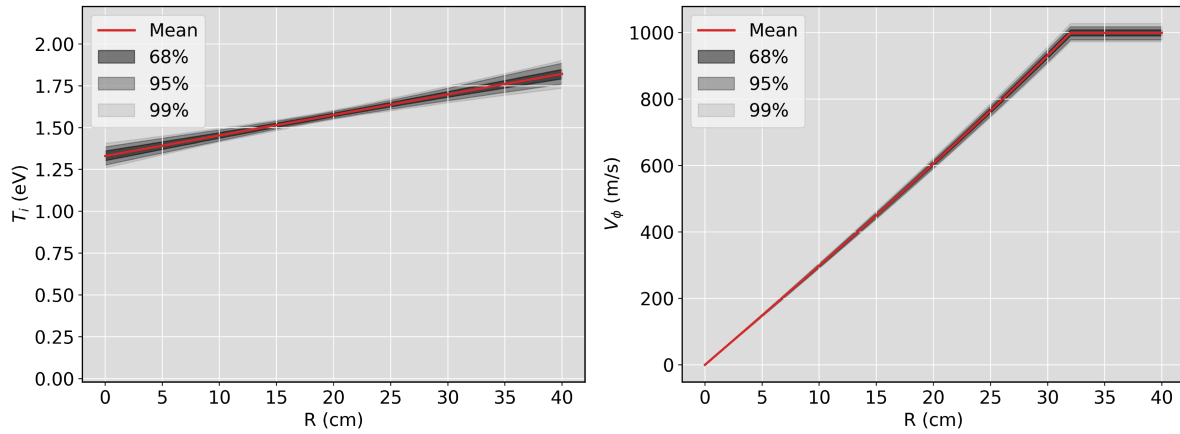


Figure 5.8: Bayesian posterior solution for  $T_i$  and  $V_\phi$  profiles. Model includes a linear  $T_i$  and  $V_\phi$  profile with  $V = 0$  forced at the origin. No oscillating quantities from the instability have been included.

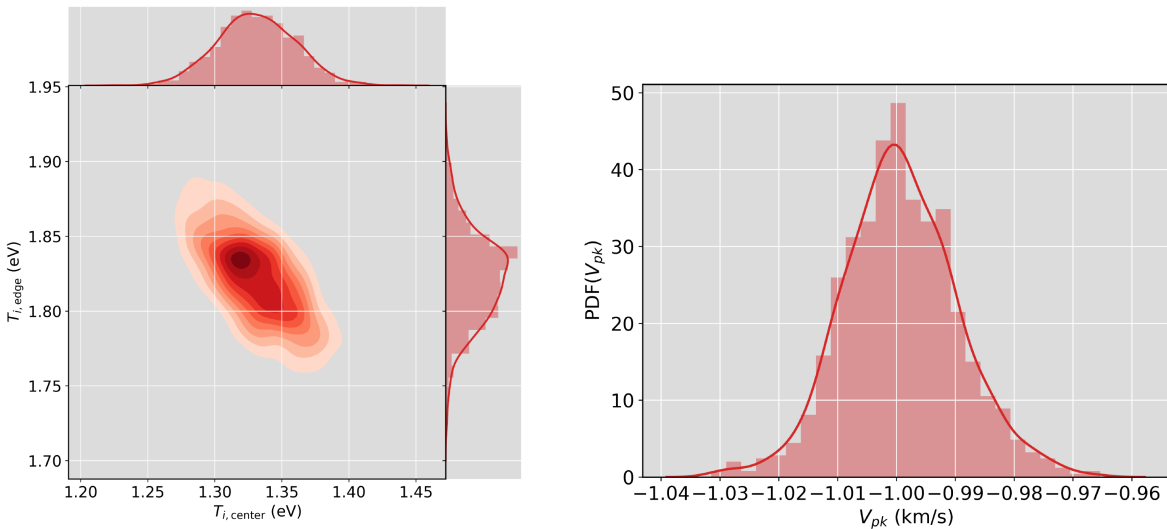


Figure 5.9: Marginal posterior for  $T_{i,\text{center}}$ ,  $T_{i,\text{edge}}$ , and  $V_{pk}$ .

The 6 individual fits from the solver are presented in Fig. 5.10. The chords show great agreement with the model for radii inside of 15 cm. For chords outside of 15 cm, the left side of the fit which corresponds to higher velocities moving away from the spectrometer deviates from the data. The zero velocity location in pixel space is marked with a red dashed line and the mode rotation

velocity is marked with a black dashed line. The deviation of the fit from the data is exactly in the region of the mode rotation velocity suggesting heating via Landau damping. Ions with velocities near the phase velocity of the wave are able to gain energy from the saturated instability. The energy deposited in the tail of the ion distribution function redistributes over time resulting in ion heating and higher ion temperatures overall. The Landau damping is easier to detect at large radii where the rotation velocity of the mode is largest.

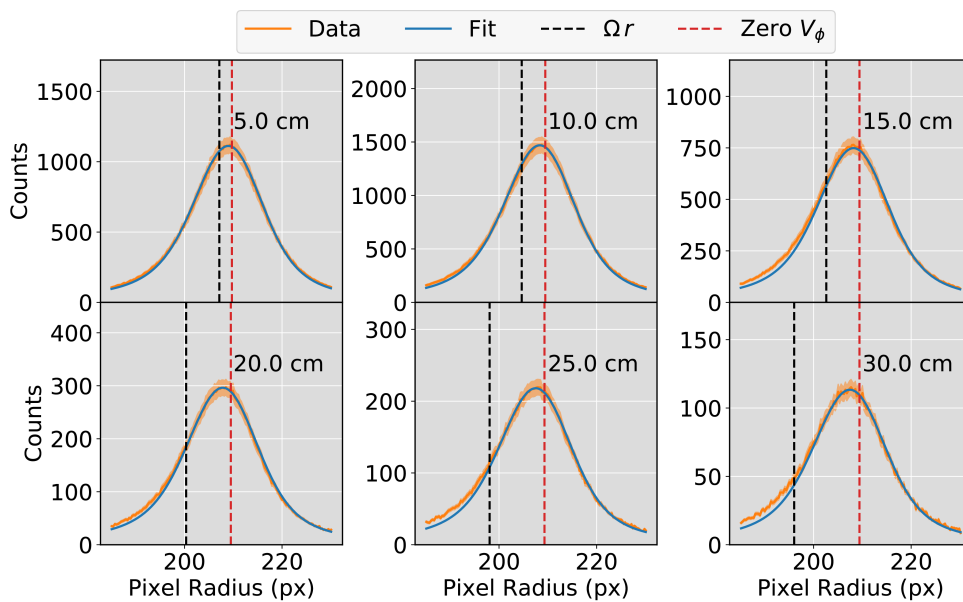


Figure 5.10: Fabry-Pérot measurements and fits for the 6 chords of the unstable plasma. The zero velocity (red dashed) position and the mode rotation velocity (black dashed) are marked in pixel space. The naive model with solid-body rotation agrees well with measurement with the high velocity tail deviating from the fit as the chords move out in radius.

The amazing precision of the Fabry-Pérot spectrometer allows us to question the validity of a  $\sim 0.5$  eV difference in temperature over the radial profile. The Bayesian model is too simplistic to explain the broadening measured by the spectrometer. The next step is to add in the fluctuating velocity the ions experience from the wave. The ion quiver velocity can be estimated from the

density fluctuations and is given by

$$\tilde{V} = \hat{k} \left( \frac{\omega - \mathbf{k} \cdot \mathbf{V}_{i0}}{k} \right) \frac{\tilde{n}}{n_0} . \quad (5.2)$$

See Appendix B and the next section for more details about the linear mode analysis. A chord at  $r = 30$  cm treated as a local measurement was modeled using a flowing thermally broadened Gaussian with a quiver velocity estimated from the density fluctuations and Eq. 5.2 time averaged over one period. The time averaging was done via numerical integration. Results from the fitting are presented in Fig. 5.11. Twice the quiver velocity and thermal velocity are shown with arrows. The ion temperature decreased by  $\sim 0.4$  eV consistent with the profile measurement discrepancy between the edge and the core. The quiver velocity should decrease as the radius approaches the central axis because the mode is rotating at a fixed angular velocity.

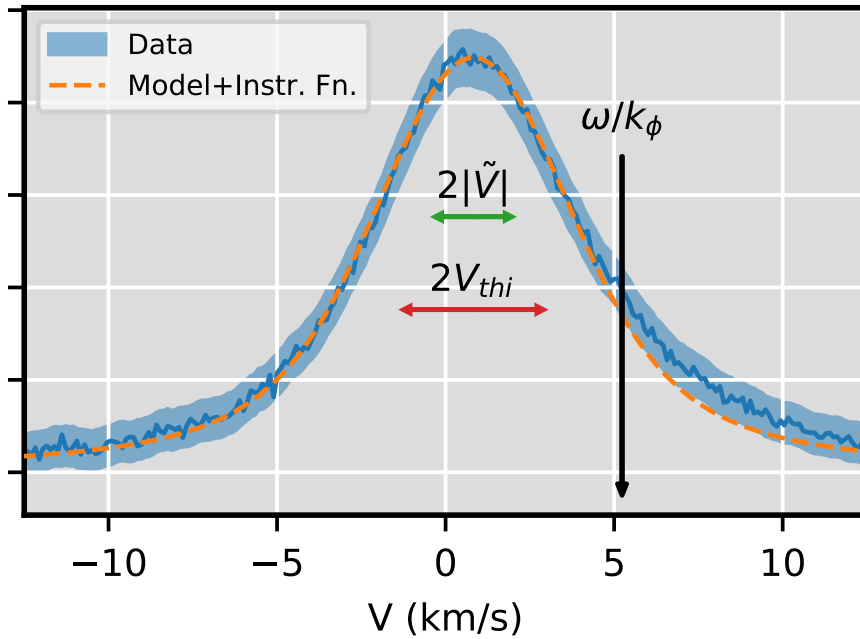


Figure 5.11: Spectrum from the Fabry-Pérot spectrometer. The model is a thermally broadened Gaussian with a fluctuating  $|\tilde{V}|$  velocity estimated from probe data. The right tail deviates from the model where Landau damping heats the tail of the ion distribution function.

Full modeling of the chord requires a proper WKB analysis for the fluctuations in the radial direction where the radial derivatives are not approximated as local oscillating quantities ( $\frac{\partial}{\partial r} \rightarrow$

$ik_r$ ). Solving for the fluctuations in the radial direction becomes a boundary valued problem that can be solved numerically using eigenfunctions and eigenvalues [69]. Once the full problem is solved, the fluctuating density and velocity with phase information can be used to model the time-average of a Fabry-Perot chord measurement. This calculation is not the subject of this thesis, but could be done in future work.

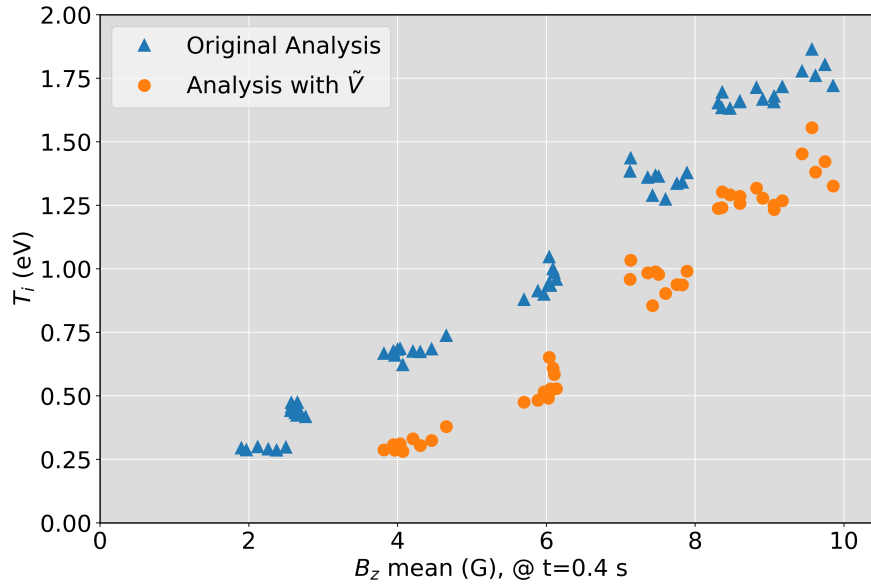


Figure 5.12:  $T_i$  vs  $B_z$  mean. Blue shows the original  $T_i$  analysis without  $\tilde{V}$ . Orange is with the  $\tilde{V}$  correction. The decrease is  $\sim 0.4$  eV for the all measurements. After the correction, the ions still show heating via Landau damping from the saturated instability.

With the injected current varied for multiple applied magnetic fields, the Fabry-Pérot spectrometer measured the ion light at a tangency radius of 30 cm. The original analysis along with the quiver velocity correction are shown in Fig. 5.12 as a function of the mean magnetic field early in the discharge. In both cases, the spectrum broadening varies linearly with the mean magnetic field. The difference between the two temperatures is approximately 0.4 eV consistent with the analysis shown in Fig. 5.11. The amount of ion heating observed relative to the magnetic field is not understood at this time.

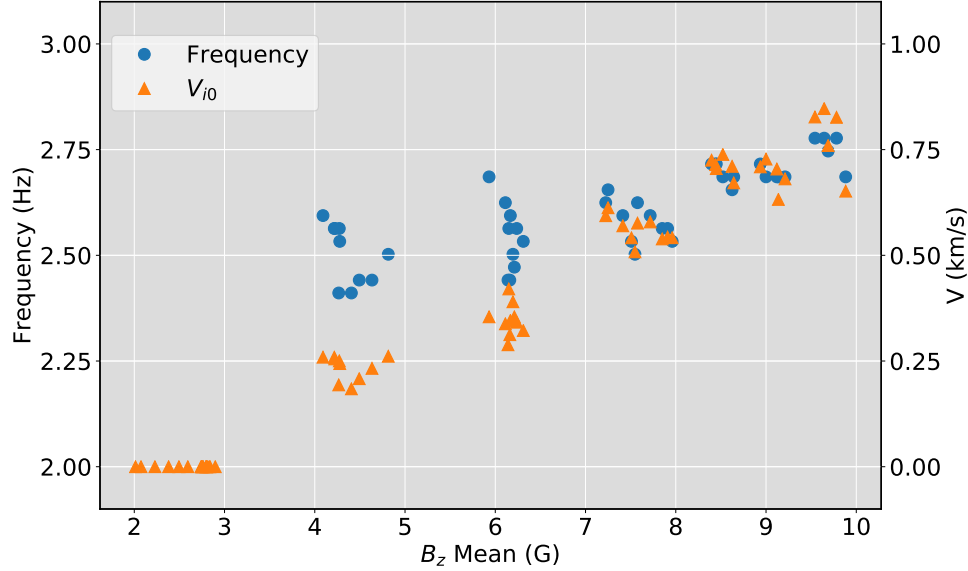


Figure 5.13: Mode frequency and peak ion velocity,  $V_{i0}$ , vs mean  $B_z$ . Each data point represents a single shot with an injected current and applied magnetic field.

With the same scan, the mode frequency and plasma peak velocity,  $V_{i0}$ , show a similar linear pattern with the mean magnetic field as shown in Fig. 5.13. The frequency has a general linear trend but with a lot of variance, especially at lower magnetic fields. The peak ion flow is mostly linear with the magnetic field, but the flow is not detectable below  $\sim 3$  G. The discussion regarding the variance of the mode frequency and the relationship to the peak ion velocity is presented later.

The mechanism for energy exchange between the ions and the wave is still undetermined, there is enough energy in the wave to explain the observed ion temperature increase in the case of instability if a collisionless mechanism like Landau damping were involved. Using an ion acoustic wave as a proxy, we can estimate the energy damping rate of the wave to estimate the amount of power absorbed by the ions. The imaginary part of the frequency for an ion acoustic wave can be used to estimate the power deposited into the ions from the wave. The imaginary part is given by

$$\omega_i = -\frac{|\omega_r|}{(1 + k^2\lambda_{De}^2)^{3/2}} \sqrt{\frac{\pi}{8}} \left[ \sqrt{\frac{m_e}{m_i}} + \left(\frac{T_e}{T_i}\right)^{3/2} \exp\left(-\frac{T_e/(2T_i)}{1 + k^2\lambda_{De}^2} - \frac{3}{2}\right) \right] \quad (5.3)$$

where  $\omega_r$  is the real part of the frequency and  $\lambda_{De}$  is the electron Debye length [70]. The difference in energy for the ions in PCX from the stable case (0.4 eV) to the unstable case (1.4 eV) at the same density of  $2 \times 10^{17} \text{ m}^{-3}$  is  $\sim 0.1 \text{ J}$ . The estimated total power deposited into the ions is  $\sim 25 \text{ W}$  assuming a 1 G magnetic fluctuation. Depositing 0.1 J with a power input of 25 W results in a heating time of  $\sim 4 \text{ ms}$  which is comparable to the ion confinement time. Based on these calculations, the energy lost by the wave via Landau damping is sufficient to explain the heating measured in the ions.

## 5.4 The Electromagnetic Gradient Drift Instability

The fluctuations seen on PCX are from the saturated state of the electromagnetic gradient drift instability, a high- $\beta$  cousin of the gradient drift instability [17]. In addition to having the electron drifts becoming unstable with the ions with free energy in the density and magnetic field gradients, the magnetic field can fluctuate as well through Ampère’s law. The derivation follows Section II of Frias et al. The full derivation can be found in Appendix B.

The derivation assumes that all quantities have a non-oscillating component denoted by “0” and an oscillating component with zero mean denoted with a “ $\sim$ ”. We assume a Fourier solution,  $\exp(-i\omega t + i\mathbf{k}_\perp \cdot \mathbf{r})$ , with  $\mathbf{k}_\perp \perp B_0 \hat{\mathbf{z}}$  in the Boussinesque approximation,  $k_x L_x \gg 1$ , where  $x$  is any of the coordinate directions. With our assumed solution, the linearized continuity equation combined with the linearized ion momentum equation gives

$$\frac{\tilde{n}}{n_0} = \frac{k_\perp^2}{(\omega - \mathbf{k}_\perp \cdot \mathbf{V}_{i0})^2 - k_\perp^2 V_{thi}^2} \frac{e\tilde{\Phi}}{m_i} \quad (5.4)$$

for the relationship between the density ( $\tilde{n}$ ) and electrostatic fluctuations ( $\tilde{\Phi}$ ) where  $\mathbf{V}_{i0}$  is the equilibrium ion flow velocity and  $V_{thi}$  is the ion thermal velocity. Equation 5.4 is only valid when  $\omega - \mathbf{k}_\perp \cdot \mathbf{V}_{i0} \gg k_\perp V_{thi}$ , otherwise kinetic effects need to be accounted for. With  $T_e$  still 2 – 3x larger than  $T_i$ , the wave is expected to be damped on the ions but the real frequency should remain close to the fluid theory.

The fluctuating magnetic field is derived from the linearization of Ampère’s law assuming that the radial current is dominated by the electron current,  $J_r \approx -neV_r^e$ . The radial component of the

fluctuating drifts for the electrons is shown in Eqn. B.7. The relationship for  $\tilde{B}$  is given by

$$\frac{\tilde{B}}{B_0} = \frac{\beta}{2} \left( \frac{e\tilde{\Phi}}{T_e} - \frac{\tilde{n}}{n_0} \right) \quad (5.5)$$

where  $\beta$  is the electron  $\beta$  and  $T_e$  is the electron temperature.

The electron continuity equation is more complicated than the ions because the compressibility of the electron flow must be accounted for. The combined continuity and momentum equations are shown in Eqn. B.6. After linearization and assuming a Fourier solution, the relationship between the fluctuating density and electrostatic potential is given by

$$\frac{\tilde{n}}{n_0} = \frac{(1 - \beta)v_* - v_D - \beta v_E}{(\omega/k_\phi) - (1 + \beta)v_E - v_D - \beta v_*} \frac{e\tilde{\Phi}}{T_e} \quad (5.6)$$

where  $v_* = -T_e \kappa_n / (eB_0)$  is the electron diamagnetic drift,  $v_D = -2T_e \kappa_B / (eB_0)$  is the magnetic drift,  $v_E = -E_0 / B_0$  is the  $E \times B$  drift, and  $\kappa_n = \partial \ln n / \partial r$  and  $\kappa_B = \partial \ln B / \partial r$  are the inverse gradient length scales for  $n$  and  $B$  respectively.

Combining Eqns 5.4 and 5.6 via quasi-neutrality gives the dispersion relation:

$$\omega = \mathbf{k}_\perp \cdot \mathbf{V}_{i0} + \frac{1}{2} \frac{k_\perp^2}{k_\phi} \frac{C_s^2}{\mathcal{A}} \left( 1 \pm \sqrt{1 - 4 \frac{k_\phi^2}{k^2} \frac{\mathcal{A}}{C_s^2} (\mathcal{B} - V_{i0})} \right) \quad (5.7)$$

where  $\mathcal{A}$  and  $\mathcal{B}$  are given by

$$\mathcal{A} = (1 - \beta)v_* - v_D - \beta v_E \quad (5.8)$$

$$\mathcal{B} = (1 + \beta)v_E + v_D + \beta v_* \quad (5.9)$$

The plasma is unstable to the electromagnetic drift instability when

$$\mathcal{A}(\mathcal{B} - V_0) > \frac{1}{4} \frac{k_\perp^2}{k_\phi^2} C_s^2 \quad (5.10)$$

For PCX, the electron drift velocities are on the order of 10 km/s with the  $E \times B$  drift being lower because the electric field is small.  $\mathcal{A}$  and  $\mathcal{B}$  are large in comparison to the sound speed and peak ion velocity but are required to have the same sign for the plasma to be unstable.

The frequency as a function of the main parameters,  $\kappa_n$ ,  $\kappa_B$ ,  $\beta$ , and  $B_0$  is shown in Fig. 5.14. PCX with  $\kappa_n < 0$  and  $\kappa_B > 0$  is always stable to the GDI for weak electric fields. Only with finite

$\beta$  is PCX unstable. As  $\beta$  increases, the region of instability in  $\kappa_n$  and  $\kappa_B$  space rotates clockwise approaching the vertical axis. The angle between the marginal stability boundary also shrinks as  $\beta$  increases. As a result, the mode is stabilized at high- $\beta$ . A frequency of  $\pm 2.5$  Hz (+ denotes rotation vector parallel to  $\hat{z}$ ) has been marked on the 4 panels to show where the frequency range of PCX is located in the 4D phase space. For PCX, unstable plasmas have  $\beta$  in the range of 1 – 4, while stable plasmas have  $\beta > 5$ .

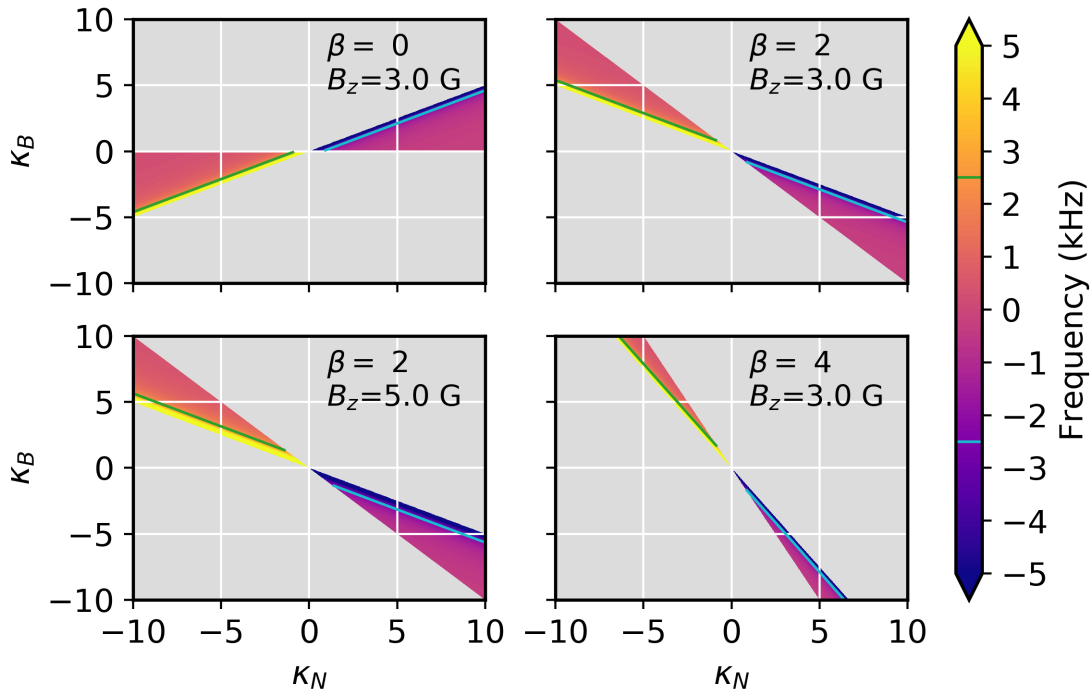


Figure 5.14: Frequency vs  $\kappa_N$  and  $\kappa_B$  at fixed  $\beta$  and  $B_z$ . PCX with  $\kappa_N < 0$  and  $\kappa_B > 0$  is stable at  $\beta = 0$ . Mode disappears at high- $\beta$ .

## 5.5 Comparison of theory and experiment

The dispersion relation for the electromagnetic gradient drift instability predicts that the frequency is linear in  $\mathbf{k} \cdot \mathbf{V}_{i0}$ . Figure 5.15 shows the relationship between the measured frequency and measured peak ion velocity. A straight line with slope  $\mathbf{k} \cdot \mathbf{V}_{i0}$  with an intercept of 2.3 kHz is

compared to the experimental data. Most of the variance in the frequency shown in Fig. 5.13 is explained by the ion flow velocity. The remaining variance is due to hard-to-measure quantities including  $\kappa_n$  and  $\kappa_B$ . The frequency of the mode diverges at one of the marginal stability boundaries making exact predictions of the frequency difficult.

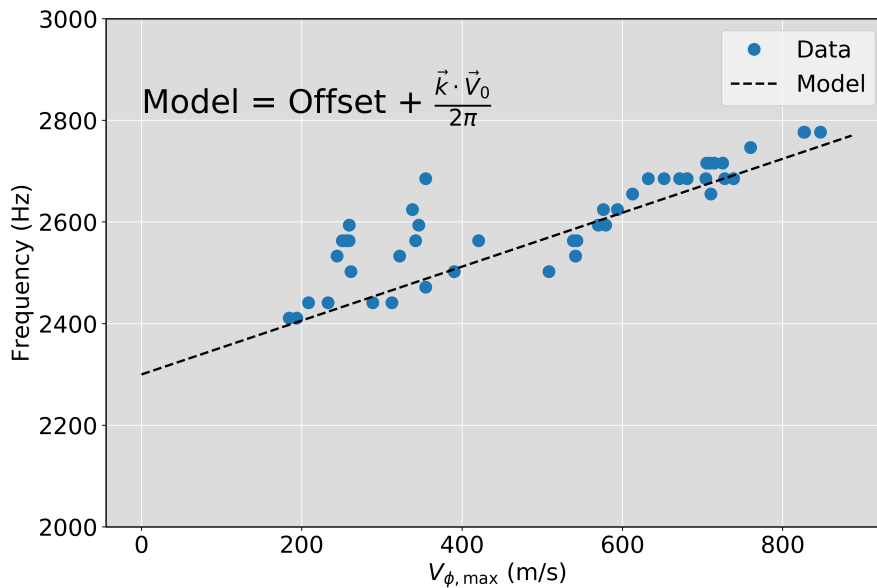


Figure 5.15: Frequency vs peak ion velocity. Most of the variance in the frequency is explained by the  $\mathbf{k} \cdot \mathbf{V}_{i0}$  Doppler shift in the dispersion relation. The remaining variance is from hard to measure quantities such as  $\kappa_B$  and  $\kappa_n$ .

The growth rate squared as a function of  $\beta$  is shown in Fig. 5.16. Only for a small range of  $\beta$  is the mode unstable ( $\gamma^2 > 0$ ). The growth rate also diverges at the high- $\beta$  limit for marginal stability. This behavior matches well with experiment. For large injected currents,  $B_z$  drops to a low value of  $\leq 1.5$  G at higher densities with  $\beta \gg 1$ . As a result, the plasma remains stable to the electromagnetic gradient drift instability. When the injected current is low, the plasma density is much lower with  $\beta \sim 2 - 4$ . In this range, PCX is unstable and immediately shows fluctuations in the saturated state.

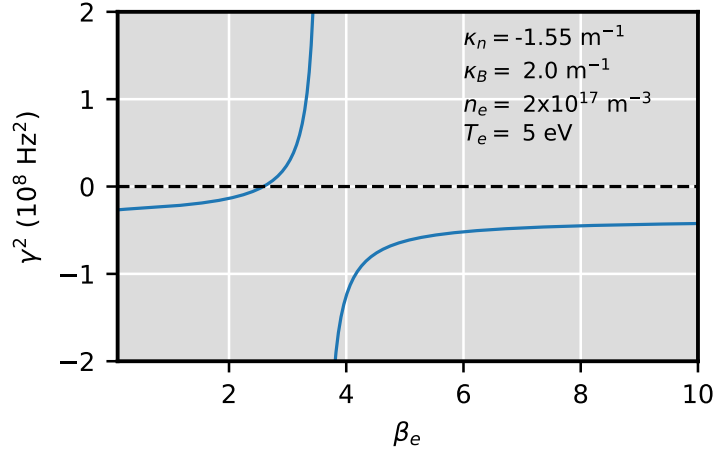


Figure 5.16: Growth rate squared,  $\gamma^2$ , vs  $\beta$ . Unstable if  $\text{Re}(\gamma) > 0$

## 5.6 Summary

We have observed a unique instability in high- $\beta$ , collisionless Hall plasmas transfer energy and momentum from the electrons to the ions. The instability may have some connections to instabilities observed in Hall thrusters [17, 14, 71, 72, 73], Penning traps [16, 74, 75] and the ionosphere [76, 77, 78, 79, 80]. The theorized gradient drift instability in these plasmas has strong electron drifts in crossed electric and magnetic fields but is electrostatic and low- $\beta$  with no magnetic field fluctuations. Previous experiments [13, 81] have shown large electromagnetic fluctuations at higher frequencies attributed to a lower-hybrid drift instability, but were unable to detect any ion heating with a directional ion velocity analyzer.

In conclusion, recent experiments on PCX have shown the excitation of the electromagnetic gradient drift instability with large amplitude magnetic and density fluctuations. Additionally, the ions are shown to be flowing in the toroidal direction and heated by the saturated instability via Landau damping. Finally, a simple two-fluid theory has been developed to explain the local dispersion relation for the electromagnetic gradient drift instability.

For flow-driven plasma instabilities, the electromagnetic gradient drift instability is problematic. The ion heating leads to a large increase in the unmagnetized ion viscosity due to the  $T_i^{5/2}$  dependence. The density is roughly  $2 \times 10^{17} \text{ m}^{-3}$  for most of the unstable plasmas discussed. With

that density and an ion temperature of 0.4 eV, the viscosity is estimated to be  $\sim 15 \text{ m}^2/\text{s}$ . If the ions have a temperature of  $\sim 1.4 \text{ eV}$  as seen in the unstable plasmas, the viscosity drastically increases to  $\sim 350 \text{ m}^2/\text{s}$ . The flow shear necessary for these instabilities is unable to develop due to the high viscosity. As a result, the fluid Reynolds number is kept quite low.

The electromagnetic gradient drift instability presents an interesting regime for future studies. The instability was not observed on the BRB with the opposite current direction to PCX. On PCX, the conditions are  $\kappa_B > 0$  and  $\kappa_n < 0$  which is only unstable with finite- $\beta$  effects. With BRB, the gradient length scales are flipped, but  $\beta$  is still relatively large indicating that the BRB should be stable. Plans for a future experiment with the matching current direction on the BRB could allow the opportunity to study the instability at higher drive currents and magnetic fields leading to the excitation of multiple modes as a path to plasma turbulence.

## Chapter 6

### Conclusion

At the start of my graduate work, the lab that houses the BRB was a converted classroom where the floor had been removed to create a two story lab space. The vacuum vessel arrived soon after with a ton of work that goes into starting a new lab. The first thing I did in the lab was attach myself to the vessel with a fall harness so hose barbs could be braised with a torch onto the aluminum pipes that would provide water cooling to the vessel wall. Since then, the lab has grown from having first plasmas in September, 2011 to becoming a national user facility.

#### 6.1 Summary of Results

This thesis was originally motivated by the pursuit of understanding flow driven instabilities such as the dynamo and the magnetorotational instability in laboratory plasmas, but the realization of the importance of Hall physics shifted the focus. However, studying flowing plasmas even in the Hall regime still required a better understanding of the ion dynamics with an upgrade to the Fabry-Pérot spectrometer for high resolution ion temperature and velocity measurements. Hall physics is known to affect the underlying process of the dynamo and MRI, but the plasma equilibrium in the lab was never really considered when the first volumetric flow drive experiments were proposed. In this thesis, it is shown that the Hall effect in these low collisionality, high- $\beta$  plasmas is crucial to understand if the dynamo and MRI are going to be observed in a laboratory plasma.

Following the motivation outlined in Chapter 1, the Big Red Ball and the Plasma Couette experiment along with the hardware, diagnostics, and data acquisition are presented in Chapter 2. Chapter 3 goes into great detail on the design, upgrades, and Bayesian analysis for the Fabry-Pérot

spectrometer for high-resolution, high-throughput ion and velocity measurements. Chapters 4 and 5 describe the rich physics of high- $\beta$  Hall plasmas.

In Chapter 3, the journey of upgrading the Fabry-Pérot spectrometer to measure both ion temperatures and flow with high precision with integration times on the order of  $\sim 100$  ms is detailed. The optics were changed to a rail mount system to increase the portability of the diagnostic and to simplify the optical alignment. A Bayesian analysis was developed to address the multi-modal issues in fixed wavelength calibration inherent to Fabry-Pérot spectrometers. The absolute wavelength calibration used for velocity measurements was solved by temperature stabilization and automatic calibration immediately after plasma discharges. With the improvements, the spectrometer is capable of measuring ion temperatures and velocities with resolutions better than 0.1 eV and 50 m/s respectively.

In Chapter 4, the effects of Hall physics on the plasma equilibrium for volumetric flow drive are described. Volumetric flow drive on the BRB successfully drives a centrally peaked ion flow. Surprisingly, a large amplification of the small applied uniform magnetic field is observed. The large increase of the magnetic field is a direct manifestation of the Hall effect. The radially outward current is mostly comprised of electrons traveling radially inward that are deflected into the toroidal direction causing an azimuthal current reinforcing the applied magnetic field. Switching the current direction results in an extreme form of diamagnetism where the electrons are deflected into the azimuthal direction to counteract the applied magnetic field. The equilibrium with an axial magnetic field and azimuthal current requires a density gradient that is hollow with radially outward current and a centrally peaked density profile for current directed radially inward. With radially directed inward current on PCX, solid body rotation with a peak of  $\sim 190$  m/s is observed with the Fabry-Pérot spectrometer. In both cases, the flow is largest when the magnetic field is capable of partially magnetizing the ions resulting in the ions to feel a portion of the  $E \times B$  torque. As a result of the magnetic field being pushed around, the ions only feel a local torque and the momentum diffuses to the rest of the plasma via viscosity. With radial cross field currents, the generated Hall currents modify the equilibrium by either reinforcing or negating the applied field

based on the injected current direction resulting in a centrally peaked or solid body flowing plasma with large density gradients.

In Chapter 5, a unique instability is observed on PCX when the applied magnetic field is too large and the diamagnetism is unable to expel most of the flux in the plasma core. The observed instability is the electromagnetic gradient drift instability, a high- $\beta$  cousin to the gradient drift instability. The mode is a non-axisymmetric flute mode and assumed to have a  $m = 1$  toroidal mode number based on high-speed video and probe data. The mode saturates during the plasma start up and rotates until the power supply turns off. Correlations between all the probes last throughout the duration of the plasma. The instability would not occur on PCX without finite- $\beta$ , but is stabilized by large  $\beta$ . Measurements from the Fabry-Pérot show that the ions are much hotter compared to stable VFD plasmas. The heating is from the saturated instability via Landau damping observed with an elongated tail in the ion distribution function near the phase velocity of the wave. The Hall effect combined with the most of the pressure coming from the electron fluid leads to an efficient mechanism where the saturated instability is able to remove energy and momentum from the electrons and deposit it into the ion fluid resulting in heating and faster flows.

The ramifications of the Hall effect in volumetric flow drive plasmas are less than ideal. For the case on BRB with radially outward current, the flow profile is centrally peaked, perfect for studying the excitation of the MRI. However, the hollowed out density profile coupled with the large increase of the magnetic field on axis suppresses the instability. The plasma beta is now below one and the magnetic tension is much stronger leading to stabilization against the MRI. On PCX, the electromagnetic gradient drift instability is exciting new physics to study with the possibility of exciting multiple modes that could be a path to plasma turbulence, but the increased ion temperature increases the viscosity dramatically limiting the amount of flow shear that can develop.

Perhaps changing gas species on the BRB could be beneficial for excitation of the MRI with volumetric flow drive. If the performance of the plasmas can be increased with more cathode power and better coupling of ECH power into the plasma, an increase in the density and the reduced mass

of the helium compared to argon could lower the ion inertial length down to the 20 – 40 cm range where Hall effects might play a smaller role in the equilibrium.

## 6.2 Future Work

The equilibrium work for the volumetric flow drive experiments is incomplete at the moment. The reversed wwwwower, we hope to carry out the experiments in both argon and helium achieving higher flow speeds.

As noted in Chapter 5, the original current configuration for VFD on BRB should be stable to the gradient drift instability and was not observed experimentally, but with the current direction flipped, the plasma should be unstable. With the next experiment with the cathodes at the poles, the equilibrium and stability observed on PCX can be probed more on the BRB with the additional power and plasma performance. If the edge peaked profile observed is not unique to PCX, the new configuration might be useful for spinning up co-rotating hemispheres to model differential flow similar to the solar convective zone. Additionally, the larger current drive and magnetic fields could lead to the excitation of multiple modes serving as a path to plasma turbulence.

The upgraded Fabry-Pérot spectrometer up to this point has only operated on PCX with argon plasmas. The diagnostic is capable of measuring helium ion emission, but helium plasmas on PCX are low-performance with too little ion emission. Moving the spectrometer to the BRB for the next set of VFD experiments will allow for the first measurement of ion temperature and flow in helium plasmas. Additionally, one of the original motivations for the Fabry-Pérot was the verification of Braginskii's unmagnetized viscosity. With faster flows on the BRB from VFD or edge-stirring, the Fabry-Pérot can be used to measure the flow shear and momentum penetration treating the plasma as a viscometer.

High- $\beta$ , Hall plasmas offer a rich new avenue of plasma physics and flow-driven instabilities to be explored. These proposed ideas are just a few directions to continue this research. I look forward to seeing the new research into high- $\beta$  Hall plasmas and especially the continued operation of the Fabry-Pérot spectrometer.

## References

- [1] Pablo D. Mininni, Daniel O. Gomez, and Swadesh M. Mahajan. Role of the Hall Current in Magnetohydrodynamic Dynamos. *The Astrophysical Journal*, 584(2):1120–1126, 2 2003. ISSN 0004-637X. doi: 10.1086/345777. URL <https://iopscience.iop.org/article/10.1086/345777>.
- [2] PABLO D. MININNI, ALEXANDROS ALEXAKIS, and ANNICK POUQUET. Energy transfer in Hall-MHD turbulence: cascades, backscatter, and dynamo action. *Journal of Plasma Physics*, 73(3):377–401, 6 2007. ISSN 0022-3778. doi: 10.1017/S0022377806004624. URL [https://www.cambridge.org/core/product/identifier/S0022377806004624/type/journal\\_article](https://www.cambridge.org/core/product/identifier/S0022377806004624/type/journal_article).
- [3] Mark Wardle. The Balbus-Hawley instability in weakly ionized discs. *Monthly Notices of the Royal Astronomical Society*, 307(4):849–856, 8 1999. ISSN 0035-8711. doi: 10.1046/j.1365-8711.1999.02670.x. URL <https://academic.oup.com/mnras/article-lookup/doi/10.1046/j.1365-8711.1999.02211.x><https://academic.oup.com/mnras/article-lookup/doi/10.1046/j.1365-8711.1999.02670.x>.
- [4] Steven A. Balbus and Caroline Terquem. Linear Analysis of the Hall Effect in Protostellar Disks. *The Astrophysical Journal*, 552(1):235–247, 5 2001. ISSN 0004-637X. doi: 10.1086/320452. URL <http://stacks.iop.org/0004-637X/552/i=1/a=235>.
- [5] N. I. Shakura and R. A. Sunyaev. Black holes in binary systems: Observational appearance. *Astronomy and Astrophysics*, 24:337–355, 1973.

- [6] E P Velikhov. Stability of an Ideally Conducting Liquid Flowing Between Cylinders Rotating in a Magnetic Field. *Soviet Physics Jetp*, 36(5):1398–1404, 1959.
- [7] S Chandrasekhar. The Stability of Non-dissipative Couette Flow in Hydromagnetics. *Proceedings of the National Academy of Sciences*, 46(2):253–257, 1960. ISSN 0027-8424. doi: 10.1073/pnas.46.2.253.
- [8] Steven A Balbus and John F Hawley. A powerful local shear instability in weakly magnetized disks. I - Linear analysis. I. Linear Analysis. *The Astrophysical Journal*, 376:214, 7 1991. ISSN 0004-637X. doi: 10.1086/170270. URL [http://articles.adsabs.harvard.edu/cgi-bin/nph-iarticle\\_query?1991ApJ...376..214B&data\\_type=PDF\\_HIGH&whole\\_paper=YES&type=PRINTER&filetype=.pdf](http://articles.adsabs.harvard.edu/cgi-bin/nph-iarticle_query?1991ApJ...376..214B&data_type=PDF_HIGH&whole_paper=YES&type=PRINTER&filetype=.pdf)<http://adsabs.harvard.edu/doi/10.1086/170270>.
- [9] SI Braginskii. Transport Processes in a Plasma. *Reviews of Plasma Physics*, 1:205, 1965.
- [10] C. S. Corr and R. W. Boswell. High-beta plasma effects in a low-pressure helicon plasma. *Physics of Plasmas*, 14(12):122503, 12 2007. ISSN 1070-664X. doi: 10.1063/1.2802080. URL <http://aip.scitation.org/doi/10.1063/1.2802080>.
- [11] Shunjiro Shinohara, Daisuke Kuwahara, Kazuki Yano, and Amnon Fruchtman. Suppression of diamagnetism by neutrals pressure in partially ionized, high-beta plasma. *Physics of Plasmas*, 23(12):122108, 12 2016. ISSN 1070-664X. doi: 10.1063/1.4968849. URL <http://dx.doi.org/10.1063/1.4968849><http://aip.scitation.org/doi/10.1063/1.4968849>.
- [12] P.-A. Gourdain, C. E. Seyler, L. Atoyán, J. B. Greenly, D. A. Hammer, B. R. Kusse, S. A. Pikuz, W. M. Potter, P. C. Schrafel, and T. A. Shelkovenko. The impact of Hall physics on magnetized high energy density plasma jets. *Physics of Plasmas*, 21(5):056307, 5 2014. ISSN 1070-664X. doi: 10.1063/1.4872022. URL <http://dx.doi.org/10.1063/1.4872022><http://aip.scitation.org/doi/10.1063/1.4872022>.

- [13] R. L. Stenzel. Lowerhybrid turbulence in a nonuniform magnetoplasma. *Physics of Fluids B: Plasma Physics*, 3(9):2568–2581, 9 1991. ISSN 0899-8221. doi: 10.1063/1.859969. URL <http://aip.scitation.org/doi/10.1063/1.859969>.
- [14] Winston Frias, Andrei I. Smolyakov, Igor D. Kaganovich, and Yevgeny Raitses. Long wavelength gradient drift instability in Hall plasma devices. II. Applications. *Physics of Plasmas*, 20(5):052108, 5 2013. ISSN 1070-664X. doi: 10.1063/1.4804281. URL <http://aip.scitation.org/doi/10.1063/1.4804281>.
- [15] Albert Simon. Instability of a Partially Ionized Plasma in Crossed Electric and Magnetic Fields. *Physics of Fluids*, 6(3):382, 1963. ISSN 00319171. doi: 10.1063/1.1706743. URL <https://aip.scitation.org/doi/10.1063/1.1706743>.
- [16] F C Hoh. Instability of Penning-Type Discharges. *Physics of Fluids*, 6(8):1184, 1963. ISSN 00319171. doi: 10.1063/1.1706878. URL <https://aip.scitation.org/doi/10.1063/1.1706878>.
- [17] Winston Frias, Andrei I. Smolyakov, Igor D. Kaganovich, and Yevgeny Raitses. Long wavelength gradient drift instability in Hall plasma devices. II. Applications. *Physics of Plasmas*, 20(5):052108, 5 2013. ISSN 1070-664X. doi: 10.1063/1.4804281. URL <http://aip.scitation.org/doi/10.1063/1.4804281>.
- [18] Cami Collins. *Spinning an unmagnetized plasma for magnetorotational instability studies in the Plasma Couette Experiment*. PhD thesis, University of Wisconsin-Madison, 2013.
- [19] C. Collins, N. Katz, J. Wallace, J. Jara-Almonte, I. Reese, E. Zweibel, and C. B. Forest. Stirring Unmagnetized Plasma. *Physical Review Letters*, 108(11):115001, 3 2012. ISSN 0031-9007. doi: 10.1103/PhysRevLett.108.115001. URL <http://arxiv.org/abs/1205.6704><http://dx.doi.org/10.1103/PhysRevLett.108.115001><https://link.aps.org/doi/10.1103/PhysRevLett.108.115001>.

- [20] David Weisberg. *Pursuing the plasma dynamo and MRI in the laboratory: Hydrodynamic studies of unmagnetized plasmas at large magnetic Reynolds number*. PhD thesis, University of Wisconsin-Madison, 2016.
- [21] D. B. Weisberg, E. Peterson, J. Milhone, D. Endrizzi, C. Cooper, V. Désangles, I. Khalzov, R. Siller, and C. B. Forest. Driving large magnetic Reynolds number flow in highly ionized, unmagnetized plasmas. *Physics of Plasmas*, 24(5):056502, 5 2017. ISSN 1070-664X. doi: 10.1063/1.4978889. URL <http://aip.scitation.org/doi/10.1063/1.4978889>.
- [22] G. Fiksel, A. F. Almagri, D. Craig, M. Iida, S. C. Prager, and J. S. Sarff. High current plasma electron emitter. *Plasma Sources Science and Technology*, 5(1):78–83, 2 1996. ISSN 0963-0252. doi: 10.1088/0963-0252/5/1/010. URL <http://stacks.iop.org/0963-0252/5/i=1/a=010?key=crossref.9d687986dcea64ad38a09a8338ab49de>.
- [23] T. Matsumoto, J. Sekiguchi, T. Asai, H. Gota, E. Garate, I. Allfrey, T. Valentine, M. Morehouse, T. Roche, J. Kinley, S. Aefsky, M. Cordero, W. Waggoner, M. Binderbauer, and T. Tajima. Development of a magnetized coaxial plasma gun for compact toroid injection into the C-2 field-reversed configuration device. *Review of Scientific Instruments*, 87(5):053512, 5 2016. ISSN 0034-6748. doi: 10.1063/1.4952581. URL <http://dx.doi.org/10.1063/1.4952581><http://aip.scitation.org/doi/10.1063/1.4952581>.
- [24] Takahiro EDO, Tomohiko ASAI, Fumiyuki TANAKA, Shodai YAMADA, Akiyoshi HOSOZAWA, Yasuhiro KAMINOU, Hiroshi GOTA, Thomas ROCHE, Ian ALLFREY, Dmitry OSIN, Roger SMITH, Michl BINDERBAUER, Tadafumi MATSUMOTO, and Toshiki TAJIMA. Performance Improvement of a Magnetized Coaxial Plasma Gun by Adopting Iron-Core Bias Coil and Pre-Ionization Systems. *Plasma and Fusion Research*, 13: 3405062–3405062, 5 2018. ISSN 1880-6821. doi: 10.1585/pfr.13.3405062. URL [https://www.jstage.jst.go.jp/article/pfr/13/0/13\\_3405062/\\_article](https://www.jstage.jst.go.jp/article/pfr/13/0/13_3405062/_article).

- [25] I. H. Hutchinson. *Principles of Plasma Diagnostics*. Cambridge University Press, 7 2002. ISBN 9780521803892. doi: 10.1017/CBO9780511613630. URL <https://www.cambridge.org/core/product/identifier/9780511613630/type/book>.
- [26] Noah Hershkowitz. How Langmuir Probes Work. In *Plasma Diagnostics*, pages 113–183. Elsevier, 1989. doi: 10.1016/B978-0-12-067635-4.50008-9. URL <https://linkinghub.elsevier.com/retrieve/pii/B9780120676354500089>.
- [27] I. H. Hutchinson. Ion collection by a sphere in a flowing plasma: 2. non-zero Debye length. *Plasma Physics and Controlled Fusion*, 45(8):1477–1500, 8 2003. ISSN 0741-3335. doi: 10.1088/0741-3335/45/8/307. URL <http://stacks.iop.org/0741-3335/45/i=8/a=307?key=crossref.3f02ffa206df98c02b0a1de95b8686e5>.
- [28] E. Ko and N. Hershkowitz. Asymmetry reversal of ion collection by mach probes in flowing unmagnetized plasmas. *Plasma Physics and Controlled Fusion*, 48(5):621–634, 5 2006. ISSN 0741-3335. doi: 10.1088/0741-3335/48/5/009. URL <http://stacks.iop.org/0741-3335/48/i=5/a=009?key=crossref.165d694907e22e268659e69e7cf2215b>.
- [29] Ethan E Peterson. *A Laboratory Model for Magnetized Stellar Winds* by. PhD thesis, University of Wisconsin-Madison, 2019.
- [30] John B Boffard, Chun C Lin, and Charles a DeJosephJr. Application of excitation cross sections to optical plasma diagnostics. *Journal of Physics D: Applied Physics*, 37(12):R143–R161, 2004. ISSN 0022-3727. doi: 10.1088/0022-3727/37/12/R01.
- [31] John B Boffard, R O Jung, Chun C Lin, and a E Wendt. Optical emission measurements of electron energy distributions in low-pressure argon inductively coupled plasmas. *Plasma Sources Science and Technology*, 19(6):065001, 2010. ISSN 0963-0252. doi: 10.1088/0963-0252/19/6/065001. URL <http://stacks.iop.org/0963-0252/19/i=6/a=065001?key=crossref.df990510e3ae0ff4856c9043d0826052>.

- [32] John B Boffard, R O Jung, Chun C Lin, L E Aneskavich, and Amy E Wendt. Optical diagnostics for characterization of electron energy distributions: argon inductively coupled plasmas. *Plasma Sources Science and Technology*, 20(5):055006, 2011. ISSN 0963-0252. doi: 10.1088/0963-0252/20/5/055006. URL <http://stacks.iop.org/0963-0252/20/i=5/a=055006>.
- [33] R W P McWhirter. *Plasma Diagnostic Techniques*. New York : Academic Press, 1965.
- [34] V. Désangles, J. Milhone, C. Cooper, D. B. Weisberg, M. D. Nornberg, and C. B. Forest. High ionisation fraction plasmas in a low temperature, multidipole cusp plasma. *Journal of Plasma Physics*, 84(3):905840312, 6 2018. ISSN 0022-3778. doi: 10.1017/S0022377818000533. URL [https://www.cambridge.org/core/product/identifier/S0022377818000533/type/journal\\_article](https://www.cambridge.org/core/product/identifier/S0022377818000533/type/journal_article).
- [35] J. A. Stillerman, T. W. Fredian, K.A. Klare, and G. Manduchi. MDSplus data acquisition system. *Review of Scientific Instruments*, 68(1):939–942, 1 1997. ISSN 0034-6748. doi: 10.1063/1.1147719. URL <http://aip.scitation.org/doi/10.1063/1.1147719>.
- [36] G. Manduchi, C. Taliercio, and A. Luchetta. The Java interface of MDSplus: towards a unified approach for local and remote data access. *Fusion Engineering and Design*, 48(1-2): 163–170, 8 2000. ISSN 09203796. doi: 10.1016/S0920-3796(00)00114-9. URL <https://linkinghub.elsevier.com/retrieve/pii/S0920379600001149>.
- [37] John D. Hunter. Matplotlib: A 2D Graphics Environment. *Computing in Science & Engineering*, 9(3):90–95, 2007. ISSN 1521-9615. doi: 10.1109/MCSE.2007.55. URL <http://ieeexplore.ieee.org/document/4160265/>.
- [38] Scott D. Baalrud, Brett Scheiner, Benjamin Yee, Matthew Hopkins, and Edward Barnat. Extensions and applications of the Bohm criterion. *Plasma Physics and Controlled Fusion*, 57(4):044003, 4 2015. ISSN 0741-3335. doi: 10.1088/0741-3335/57/4/

044003. URL <http://stacks.iop.org/0741-3335/57/i=4/a=044003?key=crossref.7885f0d198bd220eefdc70639c9e78e>.
- [39] Scott Robertson. Sheath and presheath in plasma with warm ions. *Physics of Plasmas*, 16(10):103503, 10 2009. ISSN 1070-664X. doi: 10.1063/1.3247874. URL <http://aip.scitation.org/doi/10.1063/1.3247874>.
- [40] Michael Keidar, Alex Shashurin, Olga Volotskova, Mary Ann Stepp, Priya Srinivasan, Anthony Sandler, and Barry Trink. Cold atmospheric plasma in cancer therapy. *Physics of Plasmas*, 20(5):057101, 5 2013. ISSN 1070-664X. doi: 10.1063/1.4801516. URL <http://aip.scitation.org/doi/10.1063/1.4801516>.
- [41] P. C. Stangeby. Measuring plasma drift velocities in tokamak edge plasmas using probes. *Physics of Fluids*, 27(11):2699, 1984. ISSN 00319171. doi: 10.1063/1.864573. URL <https://aip.scitation.org/doi/10.1063/1.864573>.
- [42] B. J. Peterson, J. N. Talmadge, D. T. Anderson, F. S B Anderson, and J. L. Shoet. Measurement of ion flows using an unmagnetized Mach probe in the interchangeable module stellarator. *Review of Scientific Instruments*, 65(8):2599–2606, 8 1994. ISSN 0034-6748. doi: 10.1063/1.1144658. URL <http://aip.scitation.org/doi/10.1063/1.1144658>.
- [43] E. Ko and N. Hershkowitz. Asymmetry reversal of ion collection by mach probes in flowing unmagnetized plasmas. *Plasma Physics and Controlled Fusion*, 48(5):621–634, 5 2006. ISSN 0741-3335. doi: 10.1088/0741-3335/48/5/009. URL <http://stacks.iop.org/0741-3335/48/i=5/a=009?key=crossref.165d694907e22e268659e69e7cf2215b>.
- [44] D. L. Rudakov, M. G. Shats, R. W. Boswell, C. Charles, and J. Howard. Overview of probe diagnostics on the H-1 heliac. *Review of Scientific Instruments*, 70(1):476–479, 1 1999. ISSN 0034-6748. doi: 10.1063/1.1149483. URL <http://aip.scitation.org/doi/10.1063/1.1149483>.

- [45] C. Charles, A. W. Degeling, T. E. Sheridan, J. H. Harris, M. A. Lieberman, and R. W. Boswell. Absolute measurements and modeling of radio frequency electric fields using a retarding field energy analyzer. *Physics of Plasmas*, 7(12):5232–5241, 12 2000. ISSN 1070-664X. doi: 10.1063/1.1322557. URL <http://aip.scitation.org/doi/10.1063/1.1322557>.
- [46] Z. Harvey, S. Chakraborty Thakur, A. Hansen, R. Hardin, W. S. Przybysz, and E. E. Scime. Comparison of gridded energy analyzer and laser induced fluorescence measurements of a two-component ion distribution. *Review of Scientific Instruments*, 79(10):10F314, 10 2008. ISSN 0034-6748. doi: 10.1063/1.2953411. URL <http://aip.scitation.org/doi/10.1063/1.2953411>.
- [47] R. A. Stern and J. A. Johnson. Plasma Ion Diagnostics Using Resonant Fluorescence. *Physical Review Letters*, 34(25):1548–1551, 6 1975. ISSN 0031-9007. doi: 10.1103/PhysRevLett.34.1548. URL <https://link.aps.org/doi/10.1103/PhysRevLett.34.1548>.
- [48] M. J. Goekner, J. Goree, and T. E. Sheridan. Laserinduced fluorescence characterization of a multidipole filament plasma. *Physics of Fluids B: Plasma Physics*, 3(10):2913–2921, 10 1991. ISSN 0899-8221. doi: 10.1063/1.859924. URL <http://aip.scitation.org/doi/10.1063/1.859924>.
- [49] G. D. Severn, D. A. Edrich, and R. McWilliams. Argon ion laser-induced fluorescence with diode lasers. *Review of Scientific Instruments*, 69(1):10–15, 1998. ISSN 00346748. doi: 10.1063/1.1148472.
- [50] C. B. Forest, K. Flanagan, M. Brookhart, M. Clark, C. M. Cooper, V. Desangles, J. Egedal, D. Endrizzi, I. V. Khalzov, H. Li, M. Miesch, J. Milhone, M. Nornberg, J. Olson, E. Peterson, F. Roesler, A. Schekochihin, O. Schmitz, R. Siller, A. Spitkovsky, A. Stemo, J. Wallace, D. Weisberg, and E. Zweibel. The Wisconsin Plasma Astrophysics Laboratory. *Journal of Plasma Physics*, 81(5), 2015. ISSN 14697807. doi: 10.1017/S0022377815000975.

- [51] C. M. Cooper, D. B. Weisberg, I. Khalzov, J. Milhone, K. Flanagan, E. Peterson, C. Wahl, and C. B. Forest. Direct measurement of the plasma loss width in an optimized, high ionization fraction, magnetic multi-dipole ring cusp. *Physics of Plasmas*, 23(10), 2016. ISSN 10897674. doi: 10.1063/1.4963850.
- [52] A. Kramida, Ralchenko, Yu, J Reader, and NIST ASD Team. NIST Atomic Spectra Database (version 5.6.1), 2018. URL <https://physics.nist.gov/asd>.
- [53] Monica M. Coakley and Fred L. Roesler. Application of conventional CCD cameras with Fabry-Perot spectrometers for airglow observations. In Jinxue Wang and Paul B. Hays, editors, *Optical Spectroscopic Techniques and Instrumentation for Atmospheric and Space Research*, number 2266, page 122. SPIE, 9 1994. doi: 10.1117/12.187548. URL <http://proceedings.spiedigitallibrary.org/proceeding.aspx?doi=10.1117/12.187548>.
- [54] M M Coakley, F L Roesler, R J Reynolds, and S Nossal. FabryPerot CCD annular-summing spectroscopy: study and implementation for aeronomy applications. *Applied Optics*, 35(33): 6479, 11 1996. ISSN 0003-6935. doi: 10.1364/AO.35.006479. URL <https://www.osapublishing.org/abstract.cfm?URI=ao-35-33-6479>.
- [55] F.L. Roesler. 12. Fabry-Perot Instruments for Astronomy. In *Methods in Experimental Physics*, volume 12, pages 531–569. Academic Press, 1974. doi: 10.1016/S0076-695X(08)60504-9. URL <https://linkinghub.elsevier.com/retrieve/pii/S0076695X08605049>.
- [56] F. Feroz, M. P. Hobson, and M. Bridges. MultiNest: an efficient and robust Bayesian inference tool for cosmology and particle physics. *Monthly Notices of the Royal Astronomical Society*, 398(4):1601–1614, 10 2009. ISSN 00358711. doi: 10.1111/j.1365-2966.2009.14548.x. URL <https://academic.oup.com/mnras/article-lookup/doi/10.1111/j.1365-2966.2009.14548.x>  
<http://arxiv.org/abs/0809.3437>  
<http://dx.doi.org/10.1111/j.1365-2966.2009.14548.x>.

- [57] F. Feroz and M. P. Hobson. Multimodal nested sampling: an efficient and robust alternative to Markov Chain Monte Carlo methods for astronomical data analyses. *Monthly Notices of the Royal Astronomical Society*, 384(2):449–463, 1 2008. ISSN 00358711. doi: 10.1111/j.1365-2966.2007.12353.x. URL <https://academic.oup.com/mnras/article-lookup/doi/10.1111/j.1365-2966.2007.12353.x>.
- [58] F. Feroz, M. P. Hobson, E. Cameron, and A. N. Pettitt. Importance Nested Sampling and the MultiNest Algorithm, 6 2013. URL <http://arxiv.org/abs/1306.2144>.
- [59] J. Buchner, A. Georgakakis, K. Nandra, L. Hsu, C. Rangel, M. Brightman, A. Merloni, M. Salvato, J. Donley, and D. Kocevski. X-ray spectral modelling of the AGN obscuring region in the CDFS: Bayesian model selection and catalogue, 2014. ISSN 0004-6361. URL <http://arxiv.org/abs/1402.0004><http://dx.doi.org/10.1051/0004-6361/201322971>.
- [60] John Skilling. Nested sampling for general Bayesian computation. *Bayesian Analysis*, 1(4): 833–859, 12 2006. ISSN 1936-0975. doi: 10.1214/06-BA127. URL <https://doi.org/10.1214/06-BA127><http://projecteuclid.org/euclid.ba/1340370944>.
- [61] Udo von Toussaint. Bayesian inference in physics. *Reviews of Modern Physics*, 83(3):943–999, 9 2011. ISSN 0034-6861. doi: 10.1103/RevModPhys.83.943. URL <https://link.aps.org/doi/10.1103/RevModPhys.83.943>.
- [62] D Sivia and J Skilling. *Data Analysis: A Bayesian Tutorial*. Oxford University Press, Oxford, United Kingdom, 2006. ISBN 978-0198568322.
- [63] J T Trauger. Broadband dielectric mirror coatings for Fabry-Perot spectroscopy. *Applied Optics*, 15(12):2998, 12 1976. ISSN 0003-6935. doi: 10.1364/AO.15.002998. URL <http://www.ncbi.nlm.nih.gov/pubmed/20168381><https://www.osapublishing.org/abstract.cfm?URI=ao-15-12-2998>.

- [64] C. Collins, M. Clark, C. M. Cooper, K. Flanagan, I. V. Khalzov, M. D. Nornberg, B. Seidlitz, J. Wallace, and C. B. Forest. Taylor-Couette flow of unmagnetized plasma. *Physics of Plasmas*, 21(4):1–9, 2014. ISSN 10897674. doi: 10.1063/1.4872333.
- [65] Noam Katz, Cami Collins, John Wallace, Mike Clark, David Weisberg, Jon Jara-Almonte, Ingrid Reese, Carl Wahl, and Cary Forest. Magnetic bucket for rotating unmagnetized plasma. *Review of Scientific Instruments*, 83(6), 2012. ISSN 00346748. doi: 10.1063/1.4723820.
- [66] C. M. Cooper, J. Wallace, M. Brookhart, M. Clark, C. Collins, W. X. Ding, K. Flanagan, I. Khalzov, Y. Li, J. Milhone, M. Nornberg, P. Nonn, D. Weisberg, D. G. Whyte, E. Zweibel, and C. B. Forest. The Madison plasma dynamo experiment: A facility for studying laboratory plasma astrophysics. *Physics of Plasmas*, 21(1), 2014. ISSN 10897674. doi: 10.1063/1.4861609.
- [67] J. G. Ziegler and N. B. Nichols. Optimum Settings for Automatic Controllers. *Journal of Dynamic Systems, Measurement, and Control*, 115(2B): 220–222, 6 1993. ISSN 0022-0434. doi: 10.1115/1.2899060. URL <https://asmedigitalcollection.asme.org/dynamicsystems/article/115/2B/220/417448/Optimum-Settings-for-Automatic-Controllers>.
- [68] C R Sovinec, A H Glasser, T A Gianakon, D C Barnes, R A Nebel, S E Kruger, D D Schnack, S J Plimpton, A Tarditi, M S Chu, and NIMROD Team. Nonlinear magnetohydrodynamics simulation using high-order finite elements. 195(1):355–386, 2004. doi: <https://doi.org/10.1016/j.jcp.2003.10.004>.
- [69] I. V. Khalzov, V. I. Ilgisonis, A. I. Smolyakov, and E. P. Velikhov. Magnetorotational instability in electrically driven flow of liquid metal: Spectral analysis of global modes. *Physics of Fluids*, 18(12):124107, 12 2006. ISSN 1070-6631. doi: 10.1063/1.2408513. URL <http://aip.scitation.org/doi/10.1063/1.2408513>.
- [70] Paul M Bellan. *Fundamentals of Plasma Physics*. Cambridge University Press, 2006. doi: 10.1017/CBO9780511807183.

- [71] Winston Frias, Andrei I. Smolyakov, Igor D. Kaganovich, and Yevgeny Raitses. Wall current closure effects on plasma and sheath fluctuations in Hall thrusters. *Physics of Plasmas*, 21(6):062113, 6 2014. ISSN 1070-664X. doi: 10.1063/1.4885093. URL <http://dx.doi.org/10.1063/1.4885093><http://aip.scitation.org/doi/10.1063/1.4885093>.
- [72] V. Nikitin, D. Tomilin, A. Lovtsov, and A. Tarasov. Gradient-drift and resistive mechanisms of the anomalous electron transport in Hall effect thrusters. *EPL (Europhysics Letters)*, 117(4):45001, 2 2017. ISSN 0295-5075. doi: 10.1209/0295-5075/117/45001. URL <https://iopscience.iop.org/article/10.1209/0295-5075/117/45001>.
- [73] N. A. Marusov, E. A. Sorokina, V. P. Lakhin, V. I. Ilgisonis, and A. I. Smolyakov. Gradient-drift instability applied to Hall thrusters. *Plasma Sources Science and Technology*, 28(1):015002, 1 2019. ISSN 1361-6595. doi: 10.1088/1361-6595/aae23d. URL <http://stacks.iop.org/0963-0252/28/i=1/a=015002?key=crossref.bc44dd1423ada8bcf06f660e6835ab83>.
- [74] Ivan Romadanov, Andrei Smolyakov, Yevgeny Raitses, Igor Kaganovich, Tang Tian, and Sergei Ryzhkov. Structure of nonlocal gradient-drift instabilities in Hall E B discharges. *Physics of Plasmas*, 23(12):122111, 12 2016. ISSN 1070-664X. doi: 10.1063/1.4971816. URL <http://dx.doi.org/10.1063/1.4971816><http://aip.scitation.org/doi/10.1063/1.4971816>.
- [75] Andrew T. Powis, Johan A. Carlsson, Igor D. Kaganovich, Yevgeny Raitses, and Andrei Smolyakov. Scaling of spoke rotation frequency within a Penning discharge. *Physics of Plasmas*, 25(7):072110, 7 2018. ISSN 1070-664X. doi: 10.1063/1.5038733. URL <http://dx.doi.org/10.1063/1.5038733><http://aip.scitation.org/doi/10.1063/1.5038733>.
- [76] N. A. Gondarenko and P. N. Guzdar. Density and electric field fluctuations associated with the gradient drift instability in the high-latitude ionosphere. *Geophysical Research Letters*,

- 31(11):n/a–n/a, 6 2004. ISSN 00948276. doi: 10.1029/2004GL019703. URL <http://doi.wiley.com/10.1029/2004GL019703>.
- [77] P K Chaturvedi and S L Ossakow. Nonlinear stabilization of the E x B gradient drift instability in ionospheric plasma clouds. *Journal of Geophysical Research*, 84(A2):419, 1979. ISSN 0148-0227. doi: 10.1029/JA084iA02p00419. URL <http://doi.wiley.com/10.1029/JA084iA02p00419>.
- [78] Charles E. Seyler, Jos M. Rosado-Román, and Donald T. Farley. A nonlocal theory of the gradient-drift instability in the ionospheric E-region plasma at mid-latitudes. *Journal of Atmospheric and Solar-Terrestrial Physics*, 66(17):1627–1637, 11 2004. ISSN 13646826. doi: 10.1016/j.jastp.2004.07.011. URL <https://linkinghub.elsevier.com/retrieve/pii/S1364682604001683>.
- [79] J. J. Sojka, M. V. Subramaniam, L. Zhu, and R. W. Schunk. Gradient drift instability growth rates from global-scale modeling of the polar ionosphere. *Radio Science*, 33(6):1915–1928, 11 1998. ISSN 00486604. doi: 10.1029/98RS02490. URL <http://doi.wiley.com/10.1029/98RS02490>.
- [80] J. C. Cerisier, J. J. Berthelier, and C. Beghin. Unstable density gradients in the high-latitude ionosphere. *Radio Science*, 20(4):755–761, 7 1985. ISSN 00486604. doi: 10.1029/RS020i004p00755. URL <http://doi.wiley.com/10.1029/RS020i004p00755>.
- [81] R. L. Stenzel and J. M. Urrutia. Electron magnetohydrodynamic turbulence in a high-beta plasma. I. Plasma parameters and instability conditions. *Physics of Plasmas*, 7(11):4450–4456, 2000. ISSN 1070664X. doi: 10.1063/1.1314343.

## Appendix A: Bayesian Probability for Fabry-Pérot Spectroscopy

The Fabry-Pérot analysis utilizes Bayesian statistics to calculate a probability function for the parameters of interest given the data. At the heart of the analysis is Bayes' theorem:

$$P(A|D) = \frac{P(D|A)P(A)}{P(D)} \quad (\text{A.1})$$

where  $A$  is the parameter of interest,  $D$  represents the data, and parameters to the right of  $|$  in a probability are held constant.  $P(A|D)$  is the probability of the parameter  $A$  given the data,  $D$ , which is different from  $P(A, D)$ , the probability of  $A$  and  $D$ . The probability of two events, such as  $A$  and  $D$ , is given by

$$P(A, D) = P(D|A)P(A) \quad . \quad (\text{A.2})$$

Marginalization allows us to eliminate the dependency of an event and account for its effect. Marginalization for a continuous probability distribution function is given by

$$P(A) = \int P(A, D)dD \quad (\text{A.3})$$

where the entire space of  $D$  has been integrated over. These equations cover most of the Bayesian probability needed to understand the Fabry-Pérot analysis outlined below and presented in great detail in Chapter 3.

The goal is to calculate the marginalized posterior probability for plasma measurements such as  $T_i$  and  $V$  given the data from a plasma. Ignoring effects such as the data is line integrated, the marginalized posterior is given by

$$P(T_i, V|\{P\}, \{C\}) = \int P(T_i, V, \{\text{Cal}\}|\{P\}, \{C\})d\{\text{Cal}\} \quad (\text{A.4})$$

where  $\{P\}$  is the set of data points in a plasma image,  $\{C\}$  is the set of data point in a calibration image, and  $\{\text{Cal}\}$  is the set of calibration parameters, and nuisance parameters such as the amplitude have been left off for brevity. The integrand in Eq. A.4 can be expanded as

$$P(T_i, V, \{\text{Cal}\}|\{P\}, \{C\}) = P(T_i, V|\{P\}, \{\text{Cal}\})P(\{\text{Cal}\}|\{C\}) \quad (\text{A.5})$$

where the conditionals have been simplified if the variables are independent. The second term in Eq. A.5 is the posterior probability for the calibration. Eq. A.5 can be interpreted as calculating the posterior for  $T_i$  and  $V$  while sampling from the calibration's posterior probability. As a result, the calibration analysis can be done separately and then sampled from for the plasma analysis.

The first step in calculating the marginalized posterior for plasma parameters is to calculate the marginalized posterior for the set of calibration parameters such as the étalon spacing,  $d$ , and the camera focal length,  $f_2$ . Applying Bayes' rule, we can express the marginalized posterior as

$$P(\{\text{Cal}\}|\{C\}) = \frac{P(\{C\}|\{\text{Cal}\})P(\{\text{Cal}\})}{P(\{C\})} \quad (\text{A.6})$$

where  $P(\{C\}|\{\text{Cal}\})$  is the likelihood probability,  $P(\{\text{Cal}\})$  is the prior probability, and  $P(\{C\})$  is the evidence. The prior can be as informative as we choose. We choose to have a mostly non-informative prior.

Each measurement is assumed to be independent from each other (i.e. pixels don't have information about adjacent pixels). The likelihood probability distribution is given by

$$P(\{C\}|\{\text{Cal}\}) = \prod_i P(C_i|\{\text{Cal}\}) \quad (\text{A.7})$$

where  $P(C_i|\{\text{Cal}\})$  is the likelihood for an individual measurement  $C_i$ . The individual likelihood is described by a Normal distribution,  $\mathcal{N}(\mu_i, \sigma_i^2)$ , where  $\mu_i$  is our model for the intensity for measurement  $i$  and  $\sigma_i^2$  is the variance estimated from the data in an annular sum.

The first term in Eq. A.5 can be rewritten with Bayes' rule as

$$P(T_i, V|\{P\}, \{\text{Cal}\}) = \frac{P(\{P\}|T_i, V, \{\text{Cal}\})P(T_i, V)}{P(\{P\}|\{\text{Cal}\})} \quad (\text{A.8})$$

where  $P(\{P\}|T_i, V, \{\text{Cal}\})$  is the likelihood for a plasma chord measurement,  $P(T_i, V)$  is the prior, and  $p(\{P\}|\{\text{Cal}\})$  is the evidence. The likelihood is the same form as the likelihood used

for the calibration posterior. With these equations, it is now possible to calculate the marginal posterior distribution for  $T_i$  and  $V$ .

## Appendix B: High Beta Gradient Drift Instability Derivation

Fluctuations from the electromagnetic gradient drift instability have been observed on the Plasma Couette Experiment. Measurements from the experiment indicate the stability is related to the plasma  $\beta$ . We believe this instability is related to the gradient drift instability [17], an electrostatic instability with  $\nabla B_z$  and  $\nabla n$  with wavevector perpendicular to  $\hat{z}$ . In addition to density and electrostatic fluctuations, large  $B_z$  fluctuations are observed and require additional physics to the gradient drift instability to explain the behavior.

The analysis outline in section II of Frias et al. is extended for magnetic fluctuations in  $B_z$  only with  $k$  perpendicular to the applied magnetic field ( $z$ ). The ions are unmagnetized and only follow a ballistic response. The ion continuity equation and momentum equation are

$$\frac{\partial n}{\partial t} + \nabla \cdot (n \mathbf{V}_i) = 0 \quad (\text{B.1})$$

$$nm_i \left( \frac{\partial \mathbf{V}_i}{\partial t} + (\mathbf{V}_i \cdot \nabla) \mathbf{V}_i \right) = ne\mathbf{E} - T_i \nabla n \quad (\text{B.2})$$

where the Lorentz force has been neglected because the ions are unmagnetized and the ion temperature is treated as a constant. We assume a Fourier solution  $\sim e^{i(-\omega t + \mathbf{k} \cdot \mathbf{r})}$  for the linear perturbations and assume a Boussinesque approximation ( $k_x L_x \gg 1$ ). With the assumed form, ion continuity and momentum balance become

$$-i\omega \tilde{n} + i\mathbf{k} \cdot \mathbf{V}_{i0} \tilde{n} + in_0 \mathbf{k} \cdot \tilde{\mathbf{V}}_i = 0 \quad (\text{B.3})$$

$$-i\omega \tilde{\mathbf{V}}_i + i(\mathbf{k} \cdot \mathbf{V}_{i0}) \tilde{\mathbf{V}}_i = -i\mathbf{k} \frac{e\tilde{\Phi}}{m_i} - V_{thi}^2 \mathbf{k} \frac{\tilde{n}}{n_0} \quad (\text{B.4})$$

Combining everything yields a relationship between the density and electrostatic fluctuations given by

$$\frac{\tilde{n}}{n_0} = \frac{k_{\perp}^2}{(\omega - \mathbf{k} \cdot \mathbf{V}_{i0})^2 - k_{\perp}^2 V_{thi}^2} \frac{e\tilde{\Phi}}{m_i} \quad (\text{B.5})$$

For fluid theory to be valid,  $\omega - \mathbf{k} \cdot \mathbf{V}_{i0} \gg k_{\perp} V_{thi}$  and can be neglected in the analysis. This assumption is discussed in more detail in Chapter 5.

The electrons are magnetized and have equilibrium  $\mathbf{E} \times \mathbf{B}$  drifts and diamagnetic drift velocities that are compressible and is accounted for in the continuity equation giving

$$\frac{\partial n}{\partial t} + \mathbf{v}_{\mathbf{E}} \cdot \nabla n - 2n(\mathbf{v}_{\mathbf{E}} + \mathbf{v}_{pe}) \cdot \nabla \ln B = 0 \quad (\text{B.6})$$

where  $v_E$  is the  $\mathbf{E} \times \mathbf{B}$  drift and  $v_{pe}$  is the electron diamagnetic drift. Assuming a Fourier form again, careful linearization of the the drift velocities with the inclusion of magnetic fluctuations gives

$$\tilde{\mathbf{v}}_{\mathbf{e}} = -ik_{\phi} \frac{\tilde{\Phi}}{B_0} \hat{r} + \left( ik_r \frac{\tilde{\Phi}}{B_0} - u_0 \frac{\tilde{B}}{B_0} \right) \hat{\phi} \quad (\text{B.7})$$

$$\tilde{\mathbf{v}}_{pe} = ik_{\phi} \frac{T_e}{eB_0} \frac{\tilde{n}}{n_0} \hat{r} - \left[ \left( ik_r \frac{T_e}{eB_0} + v_* \right) \frac{\tilde{n}}{n_0} + v_* \frac{\tilde{B}}{B_0} \right] \hat{\phi} \quad (\text{B.8})$$

where  $\mathbf{u}_0 = -E_{r0}/B_0 \hat{\phi}$  is the equilibrium  $\mathbf{E} \times \mathbf{B}$  drift velocity and  $\mathbf{v}_* = -T_e \kappa_n / (eB_0) \hat{\phi}$  is the equilibrium diamagnetic drift.

The magnetic fluctuations can be related to the density and electric field perturbations through Ampère's Law. Assuming the toroidal current is only from the electron drift velocities and neglecting the displacement current, the toroidal component of Ampère's law is

$$(\nabla \times \mathbf{B})_r = \mu_0 J_r = -\mu_0 n e \mathbf{V}_{\mathbf{e}} \cdot \hat{\mathbf{r}} \quad (\text{B.9})$$

$$ik_{\phi} \tilde{B} = -\mu_0 n e \tilde{V}_{e,r} \quad (\text{B.10})$$

where  $\mathbf{V}_{\mathbf{e}}$  is the total electron drift velocity. Linearizing Eq. B.9 and inserting Eqn B.7 gives

$$\frac{\tilde{B}}{B_0} = \frac{\beta}{2} \left( \frac{e\tilde{\Phi}}{T_e} - \frac{\tilde{n}}{n_0} \right) \quad (\text{B.11})$$

where  $\beta = 2\mu_0 n_0 T_e / B_0^2$  is the electron plasma pressure to magnetic pressure ratio.

Linearizing Eq. B.6 and assuming a Fourier solution gives

$$-i\omega\tilde{n} + u_0 \frac{\partial n_0}{\partial r} + iu_0 k_\phi \tilde{n} - 2n_0 \kappa_B (\tilde{\mathbf{V}}_E + \tilde{\mathbf{V}}_{pe}) \cdot \hat{\mathbf{r}} - 2n_0(u_0 + v_*) i k_\phi \frac{\tilde{B}}{B_0} = 0 \quad (\text{B.12})$$

and combining Eqns. B.7-B.11 results in

$$\frac{\tilde{n}}{n_0} = \frac{(1 - \beta)v_* - v_D - \beta v_E}{(\omega/k_\phi) - (1 + \beta)v_E - v_D - \beta v_*} \frac{e\tilde{\Phi}}{T_e} \quad (\text{B.13})$$

where  $v_D = -2T_e \kappa_B / (eB_0)$  is the electron magnetic drift velocity and  $\kappa_B = \partial \ln B / \partial r$  is the inverse gradient length scale for the magnetic field. Setting  $\beta = 0$  recovers the result from Frias et al. Eq. 16 [17].

Invoking quasi-neutrality to combine Eqns. B.5 and B.13 gives the dispersion relation

$$\omega = \mathbf{k}_\perp \cdot \mathbf{V}_{i0} + \frac{1}{2} \frac{k_\perp^2 C_s^2}{k_\phi \mathcal{A}} \left( 1 \pm \sqrt{1 - 4 \frac{k_\phi^2 \mathcal{A}}{k^2 C_s^2} (\mathcal{B} - V_0)} \right) \quad (\text{B.14})$$

where  $\mathcal{A}$  and  $\mathcal{B}$  are given by

$$\mathcal{A} = (1 - \beta)v_* - v_D - \beta v_E \quad (\text{B.15})$$

$$\mathcal{B} = (1 + \beta)v_E + v_D + \beta v_* \quad (\text{B.16})$$

For  $\beta = 0$ , the unstable criterion from Frias et al. is recovered. The condition for instability is

$$\mathcal{A}(\mathcal{B} - V_0) > \frac{1}{4} \frac{k^2}{k_\phi^2} C_s^2 \quad (\text{B.17})$$

Assuming  $V_0$  is small and inserting Eqns B.15 and B.16 gives

$$\left[ (1 - \beta)\kappa_n - 2\kappa_B - \beta \frac{eE_0}{T_e} \right] \left[ (1 + \beta) \frac{eE_0}{T_e} + 2\kappa_B - \beta\kappa_n \right] > \frac{1}{4} \frac{k^2}{k_\phi^2} \frac{1}{\rho_s^2} \quad (\text{B.18})$$

where  $\rho_s = C_s / \Omega_{ci}$  is the ion Larmor sound radius.

## Appendix C: Electron Cyclotron Heating System

The electron cyclotron heating (ECH) system was built to produce and heat plasmas on the BRB. For the purposes of studying flow driven instabilities, it is important to decouple the plasma production from the stirring drive. ECH also directly heats the electrons, important for increasing the magnetic Reynold's number,  $R_m = LV/\eta \propto T_e^{3/2}$ . With  $R_m \gg 1$ , the plasma is able to advect field lines with the plasma flow, an important criterion for instabilities such as the dynamo.

### C.1 Building a Magnetron Power Supply

The original goal for the ECH system was to build a power supply for 5 20 kW steady-state 2.45 GHz magnetrons. A steady-state magnetron requires a few key components for operation: a high voltage power supply, an DC magnetic field, and a heater circuit for the cathode filament.

#### C.1.1 High Voltage Power Supply

The high voltage power supply had a few design goals: a regulated output voltage than can vary from 5 kV to 15 kV with less than 5% ripple, a 1 ms turn on/off time, and 10 A of output current to power all five magnetrons. We decided to build our power supply based on a simple linear regulator with a 4CX35000C power tetrode to regulate the output voltage. The tetrode is capable of dropping all of the input voltage at zero current. As a result, it can be used as a modulator and a regulator and will be referred to as the Mod/Reg.

The high voltage power supply system consists of a few stages: a 3 phase step up transformer, a 3-phase rectifier, a filter capacitor, a 360 Hz notch filter, and the modulator/regulator (Mod/Reg) brought over from MIT by Jan Egedal. These components can be seen in Fig. C.1. The transformer

steps up from 240 VAC to 14.5 kVAC. The output of the transformer is then passed through a 3-phase rectifier. The output of the rectifier is filtered by a  $16 \mu\text{F}$  capacitor and a 360 Hz notch filter consisting of an inductor and capacitor in series. The voltage after the filters is much higher than 14.5 kV because of the leakage inductance of the step up transformer. Under no load, the output voltage is around 20.5 kV which corresponds to the peak voltage of 14.5 kVAC. Under loads of about 10 A, the voltage never droops below 19 kV. The magnetrons operate in the range of 13.5 to 14.5 kV and require a voltage regulator.

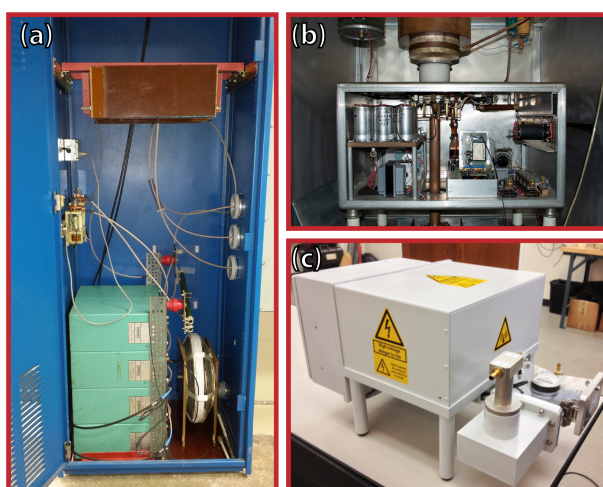


Figure C.1: a) Picture of the high voltage rectifier, filter caps, and 60 Hz notch filter. b) Picture of the inside of the mod/reg power supply. The grid driver circuit raises/lowers the tetrode grid voltage based on the light level in the fiber optic cable. c) Picture of a Muegge 20 kW 2.45 GHz magnetron with WR-430 circulator with water dummy load.

The main component of the Mod/Reg is a power tetrode (4CX35000). A tetrode is a vacuum tube with four electrodes: a thermionic cathode, an anode, a control grid, and a screen grid. The purpose of the screen grid is to electrostatically shield the anode from the control grid. The grid voltage ultimately controls the load current through the tube setting the voltage drop from the cathode to the anode. The feedback control consists of a voltage divider and a comparator to a set point. The difference or set point error is transmitted over a fiber using an infrared diode. The grid

driver adjusts the grid voltage up and down based on the increased or decreased error signal. A simplified schematic of the high voltage power supply is shown in Fig. C.2.

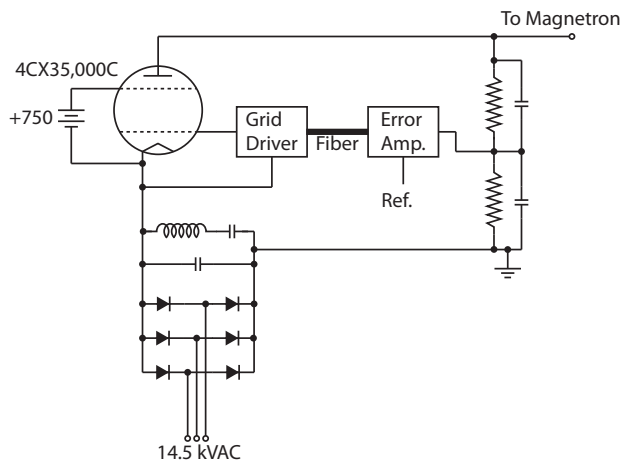


Figure C.2: Schematic of the high voltage Modulator/Regulator (mod/reg) power supply. 14.5 kV is rectified and filtered with 16 (or is it 4, I should check the vault)  $\mu\text{F}$  capacitor and a 60 Hz LC notch filter. The heart of the mod/reg is a 35 kW power tetrode with 750 applied to the screen grid relative to the cathode. The output voltage is measured with a voltage divider and compared against a reference voltage. The error is transmitted over a fiber to the grid driver which adjusts the grid voltage to change the output voltage.

Initial testing of the Mod/Reg was carried out in feed-forward mode where the negative feedback is turned off. A current was applied to the infrared diode to set the grid voltage to a steady state value. The load was a 2 K $\Omega$  water load resistor with copper sulphate dissolved in the water. The results from the test are summarized in Fig. C.3. Four different grid voltages were used in the test with the most negative resulting in zero output voltage. As the grid voltage is raised, the output voltage increases in magnitude. As expected, the ripple on the output voltage increases as the load current increases because the 16  $\mu\text{F}$  capacitor begins to discharge during the cycle. As seen in the FFT in Fig. C.3, the dominant frequency of 360 Hz has been reduced significantly.

The Mod/Reg was tested with feedback on the same water load resistor to demonstrate voltage regulation and the ability to modulate on and off. The control voltage was varied to change the

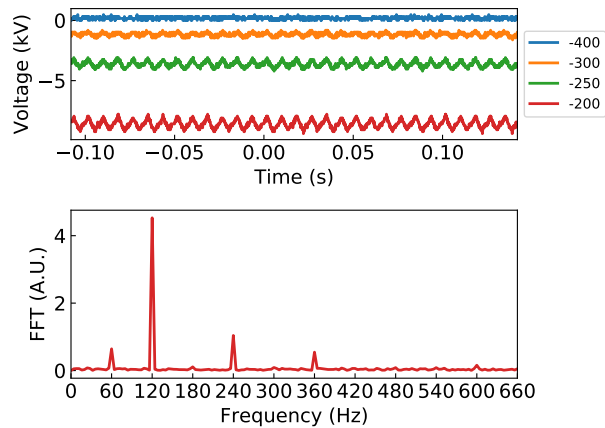


Figure C.3: The top graph shows the voltage trace of the mod/reg with a 2k resistor load in feed-forward control as a function of the grid voltage. Under small load currents ( $V_{grid} < -250$ ), the voltage ripple is small as expected. As a grid voltage is raised and the current through the load increases, the ripple grows. The bottom graph shows an fast Fourier transform (FFT) of the  $V_{grid} = -200$  V case where the dominant frequency is 120 Hz. For a 3 phase rectifier, 360 Hz is the dominant mode expected and has been mostly eliminated by the LC notch filter.

output voltage from a few kV up to  $\sim 16$  kV. The results from the water load testing can be see in Fig. C.4. With the resistive load, the Mod/Reg is showing good voltage regulation as well as very fast turn on.

### C.1.2 Electromagnet

The magnetic field is a crucial component to magnetron operation. The electrons move radially outward from the cathode to the anode. The magnetic field deflects their trajectory into the toroidal direction. If the right conditions are met, the electrons resonate with the magnetron anode structure at the RF output frequency.

For a typical microwave oven magnetron, the magnetic field is from permanent magnet. In contrast, a high-power microwave with variable output power will use an electromagnet to control the RF output power. When the magnetic field is much larger than the optimal field, the magnetron

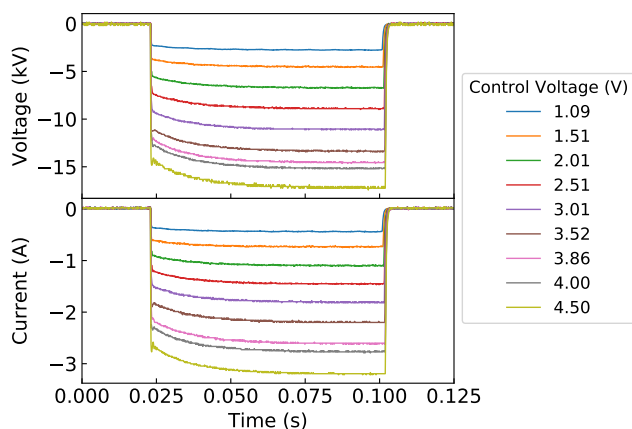


Figure C.4: Testing the mod/reg power supply with a high voltage water load by varying the control voltage input. It seems that the mod/reg is regulating well and removing the 60 Hz harmonics.

is cutoff and the electrons are unable to travel from the cathode to the anode. When the magnetic field is too weak, the electrons don't resonate with the anode cavities and no RF is produced. The output power can be varied by using a less than optimal magnetic field where the electrons don't perfectly resonate with the cavity.

### C.1.3 Filament Control

When a magnetron is in operation, a portion of the electrons resonating with the anode cavities will strike the cathode and generate more heat. At high output powers, this additional heating can be substantial and must be avoided. To mitigate the issue of electron back bombardment, the AC voltage applied to the filament is reduced based on the output RF power. Our goal was to create a system that would automatically reduce the filament heating power as the magnetron Rf power increased. We decided to use a relatively simple technology not used very often anymore, a saturable reactor. In simple terms, a saturable reactor is a current controlled variable inductor. If the control winding has a large DC current, the inductance of the AC winding decreases and more of the voltage is dropped across the inductor instead of the filament load. In practice, our saturable reactor was built out of two toroidal cores wired in series, but magnetically anti-parallel. Two

extra windings were wrapped around both cores and will be called the two control windings. The primary windings are for the AC circuit and will function as a variable inductor. DC current is applied to the control windings to saturate the cores and lower their inductance. The primary windings are hooked up anti-parallel such that no net electromotive-force (EMF) is produced in the control windings. The first control winding is used to heat the filament up by slowly ramping the current up to some value. The second control winding has current running in the opposite direction to oppose the saturation from the first control winding. This second control winding will be run in series with the magnetron to automatically decrease the filament heating power. A simplified schematic of the saturable reactor can be seen in Fig. C.5. Primary voltage and current waveforms for the magnetron filament can be seen in Fig. C.6 for various DC control currents. The waveforms are similar to phase angle control with a triac, but are more rounded and contain less harmonic content.

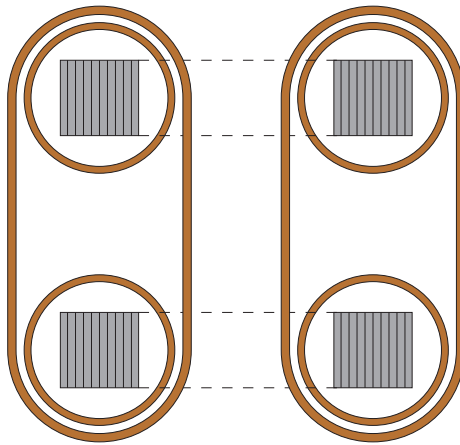


Figure C.5: Diagram of a 2 toroidal core saturable reactor. The AC windings are connected in series, but anti-parallel in magnetic polarity. The DC control windings wrap around both cores. The AC windings do not induce a net voltage on the DC control windings because each produces a voltage opposite to the other.

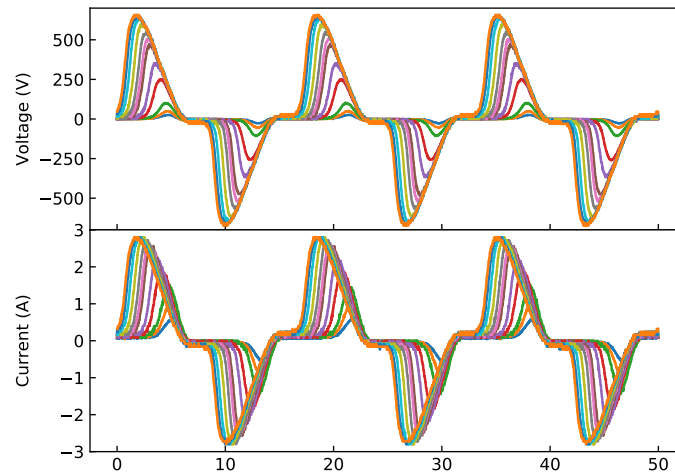


Figure C.6: Primary side waveforms for the magnetron filament with varying control currents through the DC winding of saturable reactor.

### C.1.4 Magnetron Testing with Mod/Reg

At this point, all of the components of the magnetron power supply have been tested separately and were ready to be wired together. The saturable reactor primary circuit was attached to the step down transformer for the magnetron filament. The step down transformer also serves as high voltage isolation for the cathode from earth ground. Control winding #1 of the saturable reactor was hooked up to a variable current power supply to control the filament heating power. Control winding #2 was wired in series with the magnetron to back off the filament heating power as the magnetron outputs more RF power. A schematic of this setup can be seen in Fig. C.7.

Initial testing of the full system was performed with short pulses,  $\sim 5$  ms. Control winding #2 was not used because of the short duration of the pulses to simplify the experimental setup. The testing setup for the magnetron had two controls: the cathode voltage and the magnet current. The first test was to pulse the high voltage at roughly -13.5 kV with a large magnet current to block the generation of RF. This worked as expected where there was almost no anode current and no RF power was generated. The second test was to find the optimal voltage and magnet current

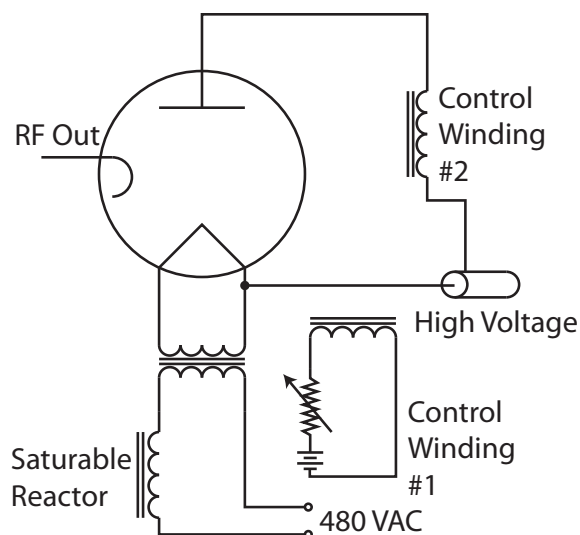


Figure C.7: Schematic of the high voltage circuit for a magnetron. The filament of the magnetron is controlled by a saturable reactor. The user increases the current in control winding #1 to increase the heating power to the filament. The high voltage is supplied to the magnetron cathode from the mod/reg power supply. The return current flows through control winding #2. The output RF power is proportional to the magnetron current. The filament power needs to be lowered as the RF power is increased to account heating from electron back-bombardment on the cathode.

for producing RF power at the full 20 kW. The datasheet from the manufacturer gives an ideal operating point of -13.5 kV for the cathode and 1.8 A for the electromagnet yielding 2.1 A of anode current and 20 kW of RF power. Unfortunately, we were unable to find this operating point.

The next steps was to perform a systematic search in our 2D parameter space looking for anode current and RF output power. We would choose a voltage set point and systematically lower the electromagnet current from RF blocking looking for the generation of RF power. Unfortunately, we were unable to find the optimal setpoint for the magnetrons. As is discussed later, the issue was most likely related to magnetron conditioning. High power continuous wave magnetrons need to be run steady-state to condition the vacuum inside the magnetron to reduce arcing.

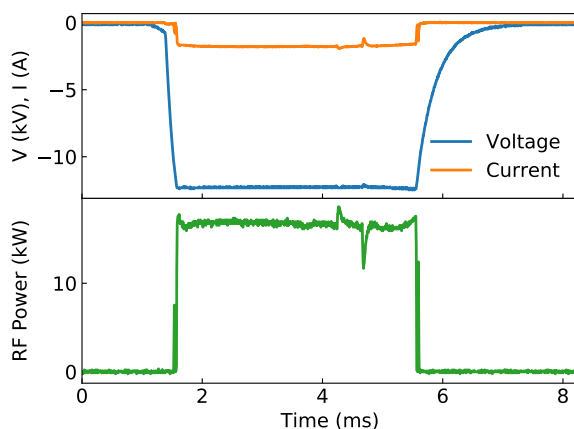


Figure C.8: Time trace of voltage, current, and output RF power for 2.8 A electromagnet current. This is a clean time trace that was not very repeatable. A proper conditioning of the magnetron would have most likely fixed this.

## C.2 Final System

### C.2.1 Muegge Power Supply

Eventually, we decided to buy the magnetron power supplies from Muegge and abandon the 1 ms rise time in-house high-voltage power supply. The power supply includes an unregulated high voltage power supply, a filament heater with circuitry to compensate for electron bombardment, a regulated electromagnet power supply, and interlocks. The high-voltage power supply is a 12 pulse rectifier with a standard capacitive filter. The electromagnet is used to regulate the output RF power by starting with a RF blocking magnetic field before applying the high voltage. The electromagnet current is decreased until the required RF power is reached. The power supply is a reliable all-in-one system that allows for easy operation of a 20 kW magnetron.

Figure C.9 shows the forward and reflected power from two magnetrons installed on the BRB. There is an approximately delay of 2-3 seconds from giving the command to the power supply to turn on and when the RF is first detected. A series of interlocks must be passed and then the electromagnet can be decreased to the require level for RF power generation. Once the electromagnet starts to decrease, the RF power has a  $\sim 200$  ms rise time, much longer than the originally desired

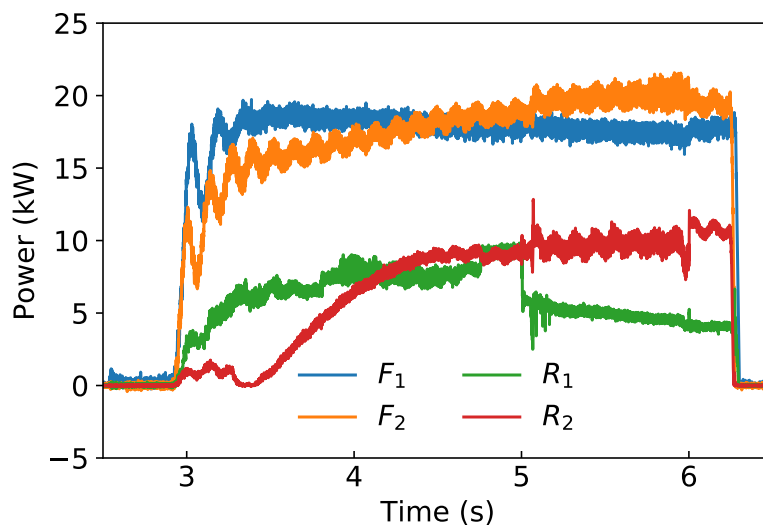


Figure C.9: Time trace of forward and reflected power for two magnetrons creating a helium plasma on the BRB. The plasma was under-dense and probably should not be reflecting as much power. It could have something to do with the horn.

1 ms rise time. The slow time scale makes it difficult to use ECH for short pulsed experiments with delicate probes that can't withstand the heat loading from long-duration plasmas.

One lesson learned after the purchase of the Muegge power supplies was the importance of conditioning. The magnetron is prone to arcing when it is not properly conditioned. To condition the magnetrons, the magnetron is run for many hours with a water-cooled waveguide dummy load. The power can be slowly ramped during that time to full power. This conditioning should be done every time the magnetron is not used for a few weeks. Because of the experimental and exploratory nature of building our power supply, we were never comfortable doing this procedure and were always going to be prone to arcing in the magnetron.

## C.2.2 Waveguide and Launcher

The original waveguide launcher was unterminated waveguide that ended at a radius near the magnet faces with mostly O-mode orientation. As a result, the first experiments had arcing between adjacent magnets that left black marks. Fortunately, the magnetization of the magnets was

unchanged when measured with a Hall probe. To mitigate arcing, the magnets within an approximate 50 cm radius were covered with copper to cover the gaps between the magnets.

The unterminated waveguide was replaced with a copper horn made by Mike Clark. The horn is flared in both the E and H plane and stops flush with the magnet faces. The horn has flexible metallic fingers in the jacket and is press fit onto the waveguide inserted into the BRB. With the copper magnet covers and the waveguide horn, most of the arcing issues were resolved.

### **C.2.3 Electron Cyclotron Heating on the Big Red Ball**

To date, 40 kW of ECH power is installed on the BRB with an additional 20 kW ready to be installed. A typical time trace of the RF power is shown in Fig. C.9 for an argon plasma. The plasma is over-dense and is most likely reflecting most of the power back down the horn. Launching the waves at an angle would most likely mitigate the reflection issues.

An RF power scan was performed for argon plasmas at a fixed neutral fill pressure. The density and temperature were measured with a Langmuir probe located in the plasma core away from the edge. The results are shown in Fig. C.10. The density and temperature show two distinct modes in the plasma that is most likely from the neutral pressure drifting over the course of the scan. The temperature does not vary much with power which is typical for argon plasmas where most of the power is radiated away.

A radial scan at a fixed neutral pressure and power was performed in argon with results presented in Fig. C.11. The plasma is just over-dense for most of the profile. The plasma resembles a typical cathode plasma with gradients only in the edge of the plasma. No excess heating is detected in the edge where the plasma is under-dense.

A triple probe radial scan was performed in helium plasmas with a single cathode biased during a portion of the plasma duration. For all RF powers, we were unable to create an over-dense helium plasma without the assistance of a cathode. The plasma is initially created with ECH only. From 135 cm and inward, the density profile resembles a typical cathode plasma. Outside of 135 cm, the RF power is creating more plasma. The electrons show an increase in temperature to approximately 125 cm. When the cathode is biased, the plasma is immediately pushed over-dense in the core.

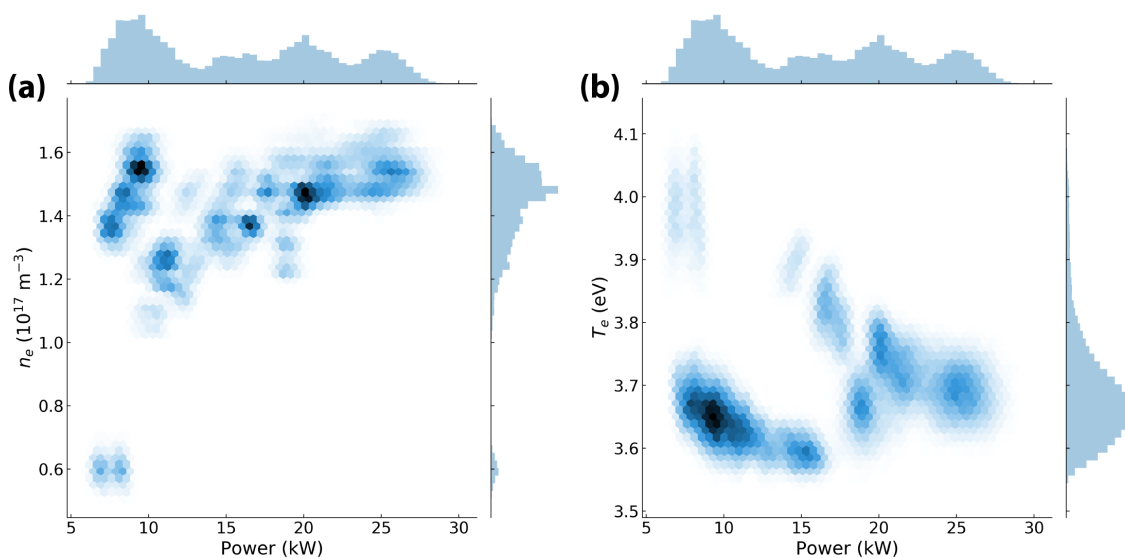


Figure C.10: Results from an RF Power Scan in argon plasmas. (a)  $n_e$  vs RF power (b)  $T_e$  vs RF power

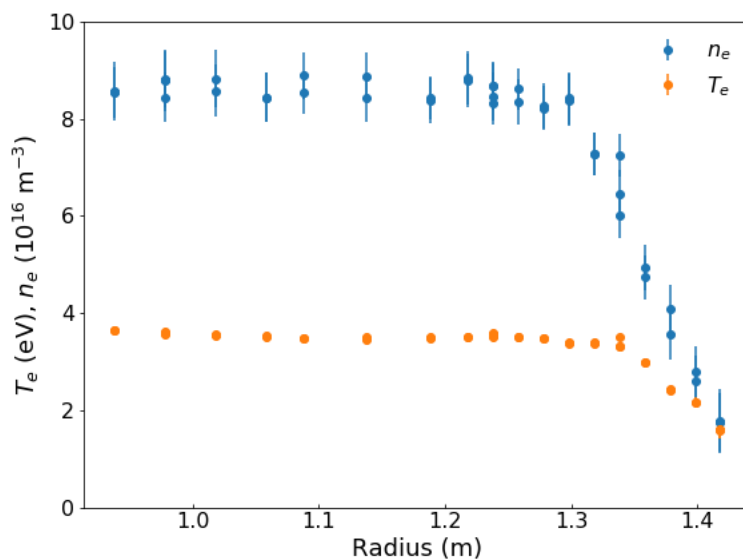


Figure C.11:  $n_e$  and  $T_e$  radial profiles in an ECH argon plasma. Profile looks very similar to a standard LaB<sub>6</sub> cathode plasma except less dense. Plasma is just over-dense with respect to the cut off density of  $7.8 \times 10^{16} \text{ m}^{-3}$  for 2.45 GHz.

The density profile resembles a cathode plasma, but shows plasma production and electron heating outside the typical plasma edge at 135 cm. After the cathode is no longer biased, the density decreases slightly but is still over-dense. The electron temperature is within error identical to the cathode and ECH plasma.

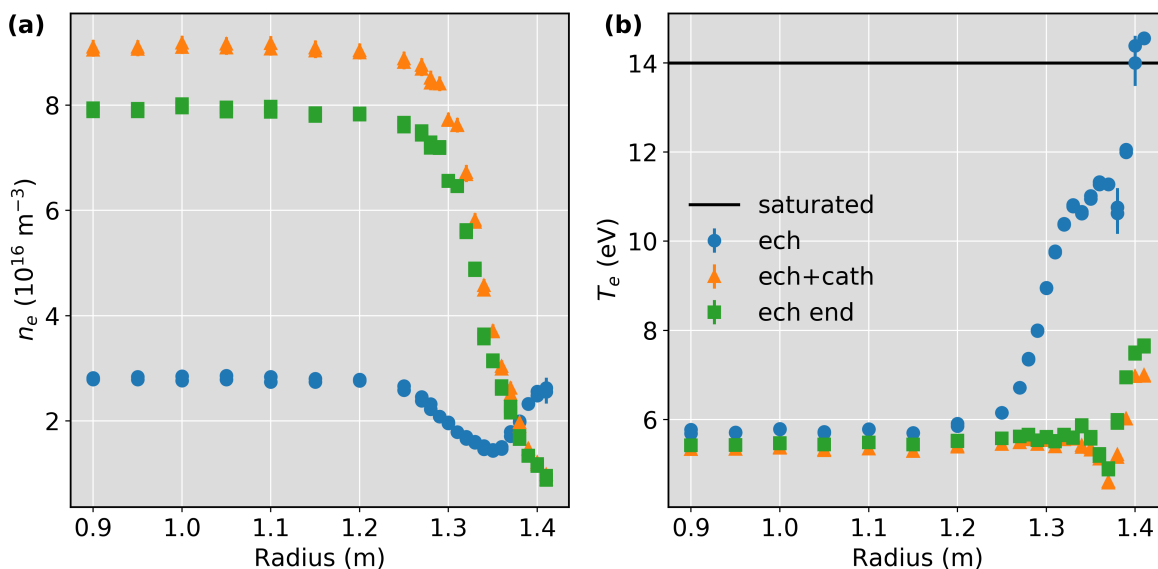


Figure C.12: Helium  $n_e$  and  $T_e$  radial profiles generated by ECH and cathodes. The plasma is created with ECH. A few seconds later, a cathode is biased for one second. ECH is continued for one second before the end of the plasma. (a)  $n_e$  and (b)  $T_e$  profiles are shown for the 3 phases from a triple probe.

### C.3 Summary

The initial goal of the electron cyclotron heating system was to efficiently create over-dense plasmas with hot electrons while decoupling the plasma producing and heating from the plasma stirring, but some issues were encountered that need addressing. Although we eventually purchased all-in-one power supplies for the magnetron, much progress was made toward building our own high-voltage power supply system with fast turn-on capability. Over-dense plasmas in argon were successfully created using ECH only, but helium required the extra input power from a LaB<sub>6</sub>

cathode. With the plasma being over-dense, coupling of the ECH power to the plasma is difficult with large amounts of power being reflected back down the waveguide. The plasma edge behaves like a mirror to the emitted microwaves. Possible improvements to the system could leverage this behavior by launching the power at an angle relative to the plasma edge to have reflections bounce back and forth between the plasma edge and vacuum vessel wall without any traveling back down the waveguide.